Lecture Notes in Electrical Engineering 531

Lei Xu
Lei Zhou *Editors*

Proceedings of the 8th International Multidisciplinary Conference on Optofluidics (IMCO 2018)

Springer

Lecture Notes in Electrical Engineering

Volume 531

The book series *Lecture Notes in Electrical Engineering* (LNEE) publishes the latest developments in Electrical Engineering - quickly, informally and in high quality. While original research reported in proceedings and monographs has traditionally formed the core of LNEE, we also encourage authors to submit books devoted to supporting student education and professional training in the various fields and applications areas of electrical engineering. The series cover classical and emerging topics concerning:

- Communication Engineering, Information Theory and Networks
- Electronics Engineering and Microelectronics
- Signal, Image and Speech Processing
- Wireless and Mobile Communication
- Circuits and Systems
- Energy Systems, Power Electronics and Electrical Machines
- Electro-optical Engineering
- Instrumentation Engineering
- Avionics Engineering
- Control Systems
- Internet-of-Things and Cybersecurity
- Biomedical Devices, MEMS and NEMS

For general information about this book series, comments or suggestions, please contact leontina.dicecco@springer.com.

To submit a proposal or request further information, please contact the Publishing Editor in your country:

China

Jasmine Dou, Editor (jasmine.dou@springer.com)

India, Japan, Rest of Asia

Swati Meherishi, Editorial Director (Swati.Meherishi@springer.com)

Southeast Asia, Australia, New Zealand

Ramesh Nath Premnath, Editor (ramesh.premnath@springernature.com)

USA, Canada:

Michael Luby, Senior Editor (michael.luby@springer.com)

All other Countries:

Leontina Di Cecco, Senior Editor (leontina.dicecco@springer.com)

**** This series is indexed by EI Compendex and Scopus databases. ****

More information about this series at http://www.springer.com/series/7818

Lei Xu · Lei Zhou
Editors

Proceedings of the 8th International Multidisciplinary Conference on Optofluidics (IMCO 2018)

Springer

Editors
Lei Xu
Department of Optical Science and Engineering
Fudan University
Shanghai, China

Lei Zhou
Department of Physics
Fudan University
Shanghai, China

ISSN 1876-1100 ISSN 1876-1119 (electronic)
Lecture Notes in Electrical Engineering
ISBN 978-981-13-3380-4 ISBN 978-981-13-3381-1 (eBook)
https://doi.org/10.1007/978-981-13-3381-1

This Springer imprint is published by the registered company Springer Nature Singapore Pte Ltd.
The registered company address is: 152 Beach Road, #21-01/04 Gateway East, Singapore 189721, Singapore

Contents

Papers from the 8th International Multidisciplinary Conference on Optofluidics (IMCO 2018)

Editors:
Lei Xu, Fudan University, Shanghai, China
Lei Zhou, Fudan University, Shanghai, China

A Method for Controlling Sensitivity of Fabry–Perot Interferometer Sensors Based on Vernier Effect

Le-yi Hou, Ben Xu, and Chun-liu Zhao

Abstract Optical fiber cascaded Fabry–Perot interferometers temperature sensors based on Vernier effect are studied in detail by theoretical simulation. The simulation results show that the free spectrum range (FSR) difference of the two Fabry–Perot interferometers affects the temperature sensitivity. When the value of the FSR difference is positive, the temperature sensitivity is positive too. Otherwise, the temperature sensitivity is negative. Furthermore, the temperature sensitivity of the Fabry–Perot interferometer sensors based on Vernier effect is higher with the FSR difference smaller. Therefore, we propose a method for controlling the sensitivity of the Fabry–Perot interferometer sensors based on Vernier effect by adjusting the difference of the two FSR.

Keywords Cascaded Fabry–Perot interferometers · Vernier effect · Temperature sensitivity · Free spectrum range difference

1 Introduction

Fabry–Perot interferometer (FPI) is universally developed and employed in pressure sensing [1, 2], strain sensing [3], temperature sensing [2], hydrogen sensing [4] and refractive index sensing [5, 6] field own to good performance as well as simple in construct. Recent years, optical Vernier effect has been attracted great interesting because which can improve sensitivity greatly [7, 8]. Especially FPI sensors based on Vernier effect are fabricated and applied to the enlargement of sensing sensitivity universally [4, 9, 10]. However, we notice that the temperature sensitivity of the

L. Hou · B. Xu · C. Zhao (✉)
Institute of Optoelectronic Technology, Jiliang University China, Hangzhou, China
e-mail: clzhao@cjlu.edu.cn; zhchunliu@hotmail.com

L. Hou
e-mail: 190996854@qq.com

B. Xu
e-mail: xuben@cjlu.edu.cn

L. Xu and L. Zhou (eds.), *Proceedings of the 8th International Multidisciplinary Conference on Optofluidics (IMCO 2018)*, Lecture Notes in Electrical Engineering 531,
https://doi.org/10.1007/978-981-13-3381-1_1

FPI sensors based on Vernier effect has different characteristics. Sometimes, the sensitivity of the FPI sensor based on Vernier effect is positive, and sometimes that is negative. Moreover, the values of the sensitivity are various from the length of the FPIs' cavities. Almost no one has found it and made a clear explanation for the phenomenon.

In this paper, optical fiber cascaded Fabry–Perot interferometers (CFPIs) sensors based on Vernier effect are studied by simulation. Results indicate that Vernier effect appears in the CFPIs sensors with the length of the HCF and the caudal SMF proportional. Free spectrum range (FSR) difference between the HCF cavity and the caudal SMF cavity determines whether the sensitivity is positive or negative. Moreover, temperature sensitivity can be enlarged by reducing the FSR difference, which has a significant guiding role on improving the sensor's sensitivity.

2 Sensor Structure and Operate Principle

The CFPIs sensors are fabricated by splicing a segment of HCF between the lead-in SMF and a section of the caudal SMF, as shown in Fig. 1. There are three reflectors in this sensor, namely mirror1 (M_1), mirror2 (M_2) and mirror3 (M_3), respectively. These three mirrors divide the configuration to two mainly FPIs. FPI1 is formed by M_1 and M_2, whose length marked as L_1. And FPI2 is formed by M_2 and M_3 and the length of it marked as L_2. Obviously, these two FPIs are cascaded.

We suppose the reflection coefficient of M_1, M_2 and M_3 is R_1, R_2 and R_3. n_1 and n_2 are the effective refractive index of medium in FPI1 and FPI2, correspondingly. When the light propagates to FPI1 and FPI2, the reflection spectra gathered in the lead-in SMF detected are calculated as follows [6]:

$$I_{rr} = \left(\frac{E_r}{E_{\text{in}}}\right)^2 = M + N + C + 2\sqrt{MC}\cos(2(\varphi_1 + \varphi_2)) + 2\sqrt{MN}\cos(2\varphi_1) + 2\sqrt{NC}\cos(2\varphi_2) \quad (1)$$

where Ein and Er are the input electric field and reflected field, respectively . $M = R_1$, N $= (1 - R_1)^2 R_2$, $\varphi_1 = 2\pi n_1 L_1/$. φ_1 is the phase deviation produced by the FPI1. Wavelength of light is λ. $P = (1 - R_1)R_2$, $Q = (1 - R_1)R^2(1 - 2)3$,

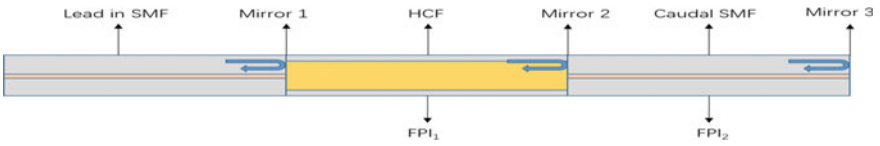

Fig. 1 Schematic configuration of the present CFPIs optical sensor

$\varphi_2 = 2\pi n_2 L_2/\lambda$. φ_2 is the phase deviation produced by the FPI2. Where $C = (1 - R_1)^2(1 - R_2)^2 R_3$. FSR of the FPI1 and the FPI2 are calculated as [11]

$$\mathrm{FSR}_1 = \frac{\lambda^2}{2n_1 L_1} \tag{2}$$

$$\mathrm{FSR}_2 = \frac{\lambda^2}{2n_2 L_2} \tag{3}$$

For convenience, D is defined as the difference between FSR1 and FSR2.

$$D = \mathrm{FSR}_1 - \mathrm{FSR}_2 \tag{4}$$

In simulation, we set the length of the air cavity and the quartz cavity properly to guarantee D very small, which will produce a Vernier effect. The temperature sensitivity of the envelop is calculated as [4]

$$S_{T-\mathrm{envelop}} = \lambda_N \left(\frac{\partial L_2}{\partial T}\frac{1}{L_2} + \frac{\partial n_2}{\partial T}\frac{1}{n_2} \right) \frac{\mathrm{FSR}_1}{\mathrm{FSR}_1 - \mathrm{FSR}_2} \tag{5}$$

where N is the resonant order belonging to integer. $\frac{\partial L_1}{\partial T}\frac{1}{L_1}$ is the thermal expansion coefficient of the HCF, namely the thermal expansion coefficient of the quartz. So $\frac{\partial L_1}{\partial T}\frac{1}{L_1} = \frac{\partial L_2}{\partial T}\frac{1}{L_2}$. $\frac{\partial n_1}{\partial T}\frac{1}{n_1}$, $\frac{\partial n_2}{\partial T}\frac{1}{n_2}$ are the thermo-optical coefficient of the air and the quartz.

3 Simulation and Result

In simulation, we set $n_1 = 1$, $n_2 = 1.44$..$R_1 = R_2 = R_3 = 0.18$. $\frac{\partial L_1}{\partial T}\frac{1}{L_1} = \frac{\partial L_2}{\partial T}\frac{1}{L_2} = 5.5 \times 10^{-7}/°\mathrm{C}$, $\frac{\partial n_1}{\partial T}\frac{1}{n_1} = -5.6 \times 10^{-7}/°\mathrm{C}$, $\frac{\partial n_2}{\partial T}\frac{1}{n_2} = 5.5 \times 10^{-6}/°\mathrm{C}$. Firstly, we simulate the spectral characteristics of CFPIs sensors under the condition that $D < 0$ and temperature at 20 and 100 °C.

Figure 2 shows the interference spectra of the CFPIs temperature sensors with $D < 0$. Red curves represent the interference spectra at 20 °C. Blue curves show the interference spectra at 100 °C. Figure 2a shows the interference spectra when D is 0.0119 nm. The FSR of the interference spectra envelops is ~126 nm. Figure 2b shows the interference spectra when D is 0.0381 nm. The FSR of these envelops is ~39.65 nm. With temperature varying from 20 to 100 °C, because of thermal expansion effect and thermo-optic effect, the interference spectrum in Fig. 2a, b shifts to longer wavelength about 78 nm and 25 nm, respectively.

Figure 3 shows the relationship between the wavelength and temperature within the CFPIs sensors with $D > 0$. Figure 3a, b are matched with Fig. 2a, b, respectively. The sensitivity of which are 0.945 nm/°C and 0.295 nm/°C, respectively. Obviously,

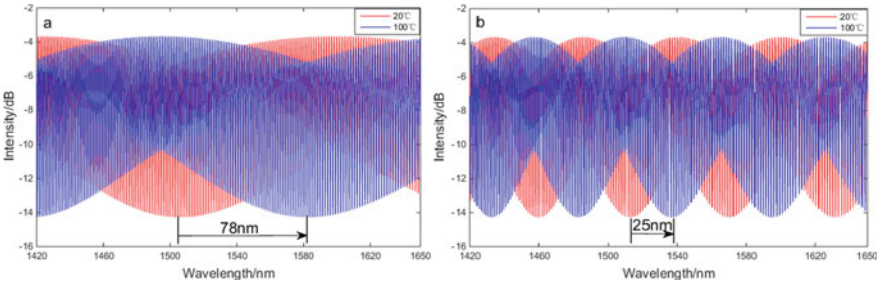

Fig. 2 Interference spectra of the CFPIs temperature sensors with $D > 0$. **a** $L1 = 800$ μm, $L2 = 560$ μm, $D = 0.0119$ nm, **b** $L1 = 800$ μm, $L2 = 570$ μm, $D = 0.0381$ nm

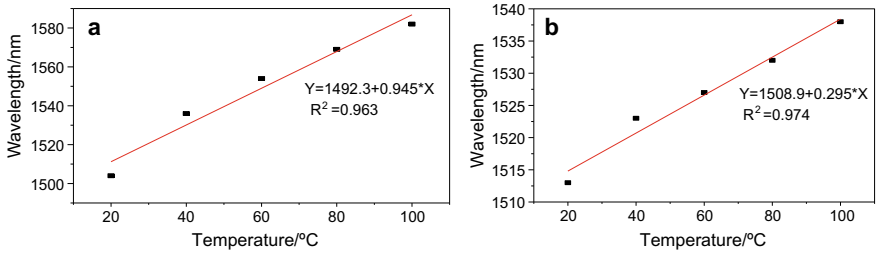

Fig. 3 Relationship between the wavelength and temperature within the CFPIs temperature sensors with $D > 0$. **a** $L1 = 800$ μm, $L2 = 560$ μm, $D = 0.0119$ nm, **b** $L1 = 800$ μm, $L2 = 570$ μm, $D = 0.0381$ nm

the temperature sensitivity of the sensor where D is small is larger than that D is higher. Then, we simulate the spectral characteristics of the CFPIs sensors under the condition that $D > 0$ and temperature at 20 and 100 °C.

Figure 4 shows the interference spectra of the CFPIs temperature sensors with $D < 0$. Red curves represent the interference spectra at 20 °C. Blue curves show the interference spectra at 100 °C. Figure 4a shows the interference spectra

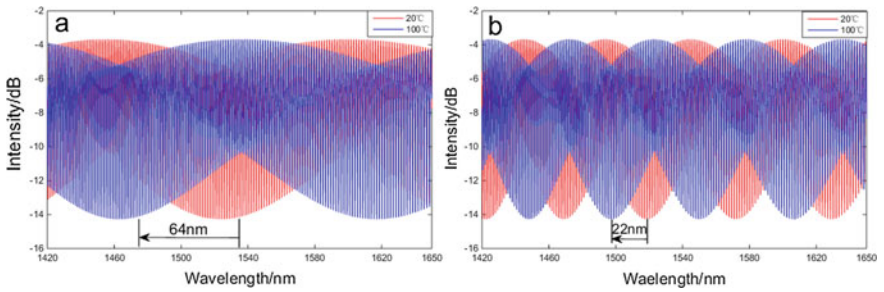

Fig. 4 Interference spectra of the CFPIs temperature sensors with $D < 0$. **a** $L1 = 800$ μm, $L2 = 550$ μm, $D = -0.0151$ nm, **b** $L1 = 800$ μm, L2 = 540 μm, $D = -0.0433$ nm

when D is −0.0151 nm. Figure 2b shows the interference spectra when D is −0.0433 nm. With temperature varying from 20 to 100 °C, the interference spectra in Fig. 4a, b shift to shorter wavelength about 64 nm and 22 nm, respectively.

Figure 5 shows the relationship between the wavelength and temperature within the CFPIs sensors with $D < 0$. Figure 5a, b are matched with Fig. 4a, b, respectively. The temperature sensitivities of them are −986 pm/°C and −0.26 pm/°C. The linear fitting coefficients are up to 0.972 and 0.970, respectively.

As shown in Fig. 6, temperature sensitivity improves with $|D|$ decreasing. Besides, we can get that when $D > 0$, the temperature sensitivity is positive; moreover, the temperature sensitivity will be negative when $D < 0$. So a method for controlling

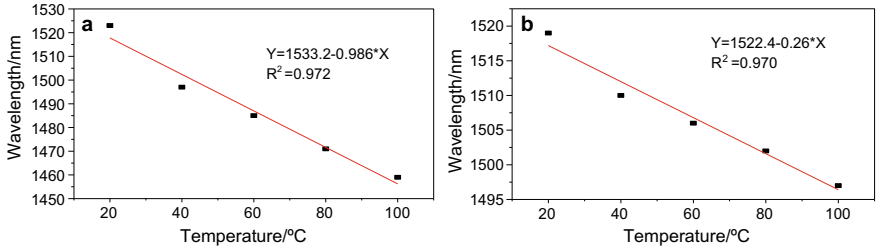

Fig. 5 Relationship between the wavelength and temperature within the CFPIs temperature sensors with $D < 0$. **a** $L1 = 800$ μm, $L2 = 560$ μm, $D = 0.0119$ nm. **b** $L1 = 800$ μm, $L2 = 570$ μm, $D = 0.0381$ nm

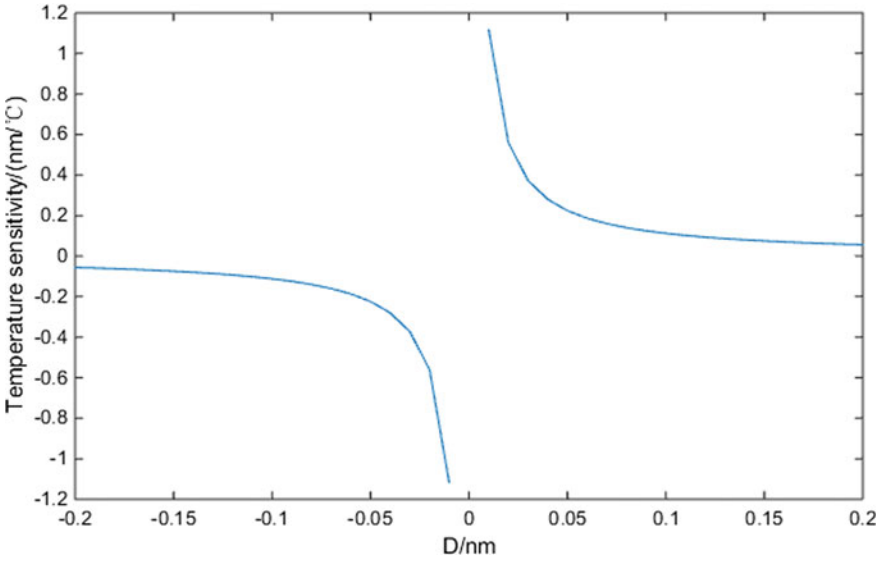

Fig. 6 Relationship between the temperature sensitivity and D value

sensitivity of FPI sensors based on Vernier effect is proposed: adjusting the length of the HCF and the caudal SMF to get higher sensing sensitivity.

4 Conclusion

In this paper, we propose a method for controlling the sensitivity of FPI sensors based on Vernier effect. We specially simulate the CFPIs sensors consist of a segment of hollow core fiber (HCF) sandwiched between the lead-in SMF and a section of caudal SMF. Simulation results show that the sensitivity has direct relationship with D. The interference spectra drift toward longer wavelength and sensitivity are positive when $D > 0$. Conversely, the interference spectra drift in the direction of shorter wavelength and the sensitivity are negative when $D < 0$. Besides, sensitivity increases with the reduction of $|D|$. Therefore, the sensitivity of FPI sensors based on Vernier effect can be controlled by adjusting the length of HCF and SMF, which has a significant guiding role on improving the sensor's sensitivity.

Funding This work is funded by Project of The National Key Research and Development Program of China No. 2017YFC0805905 and No. 2018YFF0215104, Project of Natural Science Foundation of China, NSFC (Number: 61775202), the Natural Science Foundation of Zhejiang Province China under Grant No. LY17F050010, National Natural Science Foundation of China (11874332) and National major scientific research instrument development project of Natural Science Foundation of China (61727816).

References

1. Zhu J et al (2017) An optical fiber Fabry-Perot pressure sensor using corrugated diaphragm and angle polished fiber. Opt Fiber Technol 34:42–46
2. Ran Z et al (2015) Novel high-temperature fiber-optic pressure sensor based on etched PCF F-P interferometer micromachined by a 157-nm laser. IEEE Sens J 15(7):3955–3958
3. Coutant O, De Mengin M, Le Coarer E (2015) Fabry-Perot optical fiber strainmeter with an embeddable, low-power interrogation system. Optica 2(5):400
4. Li Y et al (2018) Optical cascaded Fabry-Perot interferometer hydrogen sensor based on vernier effect. Opt Commun 414:166–171
5. Chen P, Shu X, Cao H (2017) Novel compact and low-cost ultraweak Fabry-Perot interferometer as a highly sensitive refractive index sensor. IEEE Photonics J 9(5):1–10
6. Tian J, Quan M, Yao Y (2015) Ultra-high sensitivity Fabry-Perot interferometer gas refractive index fiber sensor based on photonic crystal fiber and Vernier effect. Opt Lett 40(21):4891
7. Liao H et al (2017) Sensitivity amplification of fiber-optic in-line Mach-Zehnder interferometer sensors with modified Vernier-effect. Opt Express 25(22):26898
8. Shao L et al (2015) Sensitivity-enhanced temperature sensor with cascaded fiber optic Sagnac interferometers based on Vernier-effect. Opt Commun 336:73–76
9. Zhang P et al (2014) Cascaded fiber-optic Fabry-Perot interferometers with Vernier effect for highly sensitive measurement of axial strain and magnetic field. Opt Express 22(16):19581

10. Zhao Y et al (2016) Highly sensitive airflow sensor based on Fabry-Perot interferometer and vernier effect. J Lightw Technol 34(23):5351–5356
11. Jiang J et al (2017) Sensitivity-enhanced temperature sensor by hybrid cascaded configuration of a Sagnac loop and a F-P cavity. Opt Express 25(26):33290

Active Planar Plasmonic Sensor for Measuring Glucose Concentration

Jing Cai and Yong Jin Zhou

Abstract A novel microwave resonator loaded with an active amplifying circuit is present, which consists of a corrugated ring structures and two coupled microstrip. Compared with passive structure, the introduction of active amplifying can compensate for the metal loss of passive structure at resonant frequency and increase quality factor significantly. The Q value of the passive structure is around 50, while the Q value of another structure is 500 times more than before, up to 25,000. Subsequently, we proposed an active liquid microwave sensor combined the proposed active resonator and microfluidic channel. Although fluid injection may lead to greater loss, active amplifying circuit can make up for these losses. The simulated results have verified its high resolution with different concentration of glucose solution. It is easy to sight the frequency offset even though the change of the concentration is only 0.2 mmol/L. These results demonstrate the proposed sensor has advantages of low costs, compactness, and high resolution for liquid detection.

Keywords Active microwave sensor · Corrugated ring · Spoof LSPs

1 Introduction

Surface plasmons (SPs) could be either propagating (surface plasmon polaritons, SPPs) in extended interfaces or localized (localized surface plasmons, LSPs) in finite metal particles [1]. Although SPs can realize many novel applications due to their novel properties of deep subwavelength confinement and field enhancement, metals behave similarly to perfect electric conductors (PEC) which does not support the SPs at lower frequencies, like microwave frequency [2]. In order to achieve the SPs at lower frequencies, the concept of spoof SPPs based on the structured metal surfaces has been proposed [3]. Spoof LSPs have been proposed and experimentally verified at microwave frequencies [4, 5]. Subsequently, various devices based on spoof LSPs

J. Cai · Y. J. Zhou (✉)
Key Laboratory of Specialty Fiber Optics and Optical Access Networks, School of Communication and Information Engineering, Shanghai University, Shanghai 200444, China
e-mail: yjzhou@shu.edu.cn

L. Xu and L. Zhou (eds.), *Proceedings of the 8th International Multidisciplinary Conference on Optofluidics (IMCO 2018)*, Lecture Notes in Electrical Engineering 531,
https://doi.org/10.1007/978-981-13-3381-1_2

have been designed, such as metallic spiral structure [6], closed subwavelength high contrast gratings [7], and closed corrugated ring [8]. However, quality factors (Q value) of the resonance peaks are still hard to get a significant boost due to their inherent loss.

In this paper, we proposed an active liquid microwave sensor combined the active microwave resonator and microfluidic channel. Compared with passive sensor, the introduction of active amplifying can compensate for the loss of passive structure at resonant frequency and increase quality factor significantly. The simulated results have verified its high resolution with different concentration of glucose solution. It is easy to sight the frequency offset even though the change of the concentration is only 0.2 mmol/L. These results demonstrate the proposed sensor has advantages of low costs, compactness, and high resolution for liquid detection.

2 Active Microwave Sensor Based on Spoof LSPs

2.1 Microwave Active Planar Resonator Based on Spoof LSPs

Figure 1a, b shows the proposed ultra-thin corrugated ring based on spoof LSPs with and without the active amplifying circuit. The corrugated ring is similar to Ref. [8], and the difference is metal of outer ring is removed to miniaturize the size and loading coupling branches. The S-parameters are calculated by simulated software HFSS (the negative resistance is used to replace the active amplifying circuit), and the results are displayed in Fig. 1d. The introduction of active amplifying can compensate for the metal loss of passive structure at resonant frequency and increase quality factor significantly. We can see that the curve S11 becomes more sharp with the introduction of active circuits. Meanwhile, the quality factor of two cases has been calculated by the method of group delay. The Q value of the passive structure is around 50, while the Q value of another structure is 500 times more than before, up to 25,000, consistent with expectations.

2.2 Active Planar Microwave Sensor for Glucose Solution

Reference [8] has verified that the closed corrugated ring has high sensitivity with changes in dielectric constant of the surrounding environment and the active circuit improved Q value so as to higher resolution. Based on these, we proposed an active liquid microwave sensor consists of proposed corrugated ring loading microfluidic channel as shown in Fig. 2a. Although fluid injection may lead to greater loss, active amplifying circuit can make up for these losses to obtain very high resolution. The simulated S11 of proposed sensor with different concentration of glucose solution is

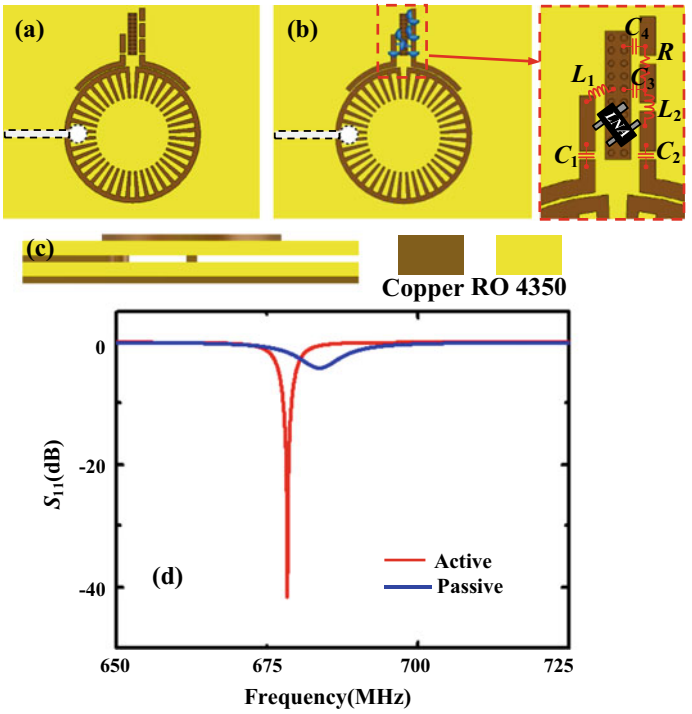

Fig. 1 Layout of the corrugated ring without (**a**) and with (**b**) active circuit; **c** the side view of the resonator; **d** simulated S-parameters of active and passive structure

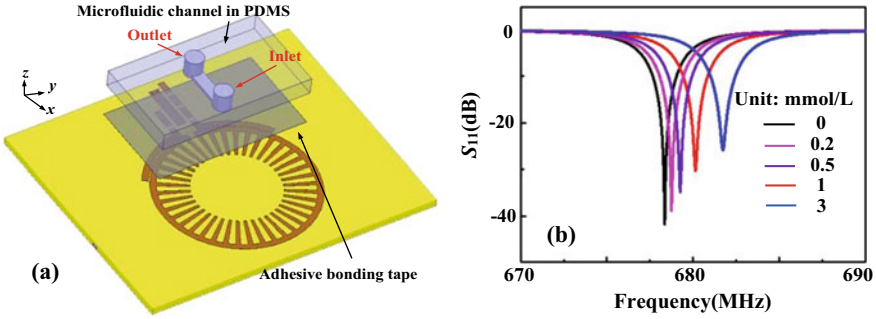

Fig. 2 **a** 3D view of the proposed sensor and **b** simulated S-parameters with different concentration of glucose solution

shown in Fig. 2b. It is observed that the proposed sensor has very high Q value even if different concentration of glucose solution is injected, and it is easy to sight the frequency offset even though the change of the concentration is only 0.2 mmol/L.

These results demonstrate that the proposed sensor has advantages of low costs, compactness, and high resolution for liquid detection.

3 Conclusions

In this paper, we proposed an active liquid microwave sensor combined the active microwave resonator and microfluidic channel. Compared with passive sensor, the introduction of active amplifying can compensate for the loss of passive structure at resonant frequency and increase quality factor significantly. The simulated results have verified its high resolution with different concentration of glucose solution. It is easy to sight the frequency offset even though the change of the concentration is only 0.2 mmol/L. These results demonstrate that the proposed sensor has advantages of low costs, compactness, and high resolution for liquid detection.

References

1. Barnes WL, Dereux A, Ebbesen TW (2010) Surface plasmon subwavelength optics. Nature 424(6950):824–830
2. Garciavidal FJ, Martínmoreno L, Pendry JB (2005) Surfaces with holes in them: new plasmonic metamaterials. J Opt A Pure Appl Opt 7(2):S97
3. Pors A, Moreno E, Martinmoreno L et al (2012) Localized spoof plasmons arise while texturing closed surfaces. Phys Rev Lett 108(22):223905
4. Shen XP, Cui TJ (2014) Ultrathin plasmonic metamaterial for spoof localized surface plasmons. Laser Photonics Rev 8(1):137–145
5. Gao Z, Gao F, Xu H et al (2016) Localized spoof surface plasmons in textured open metal surfaces. Opt Lett 41(10):2181
6. Huidobro PA, Moreno E, Martin-Moreno L et al (2014) Magnetic localized surface plasmons. Phys Rev X 4(2):340–342
7. Li Z, Xu B, Liu L et al (2016) Localized spoof surface plasmons based on closed subwave-length high contrast gratings: concept and microwave-regime realizations. Sci Rep 6:27158
8. Yang BJ, Zhou YJ, Xiao QX (2015) Spoof localized surface plasmons in corrugated ring structures excited by microstrip line. Opt Express 23(16):21434–21442

Bessel-Like Beams Based on Optical Fiber Polymer Microtips

Jingyu Tan, Ruowei Yu, and Limin Xiao

Bessel-like beams possess unique light intensity distribution and self-healing propagation property have been widely used in various fields such as imaging [1], particle guiding [2], and microfabrication [3]. Generation of them with optical fibers allows a compact device without alignment and stability issues compared with bulky optical systems. Microaxicons at the fiber ends were fabricated to produce a Bessel-like beam [4, 5]; however, the fabrication process is generally time-consuming and complicated. Besides, multimode fibers were spliced to single mode fibers (SMFs) with fiber lens or SMFs with long period gratings to demonstrate the generation of Bessel-like beam[6, 7].

Bachelot et al. introduced a method to fabricate a microtip on the top end of optical fibers based on free radical photopolymerization [8]. Our approach relies on the growth of such a polymer microtip fabricated at the facet of a SMF. In this letter, we will show the optimization of length and shape of microtips to generate Bessel-like beams and the investigation of far-field patterns and the self-healing property.

The photopolymerizable reagent is made up of 0.5% in weight of eosin Y, 8% in weight of methyldiethanolamine, and 91.5% in weight of pentaerythritol triacrylate [8]. A drop of photopolymerizable reagent was deposited on the end of SMF-28 from Corning. Generally, the droplet length on the facet is around 30 μm because of

J. Tan · R. Yu · L. Xiao (✉)
Advanced Fiber Devices and Systems Group, Key Laboratory of Micro and Nano Photonic Structures (MoE), Department of Optical Science and Engineering, Fudan University, Shanghai, China
e-mail: liminxiao@fudan.edu.cn

L. Xiao
Key Laboratory for Information Science of Electromagnetic Waves (MoE), Fudan University, Shanghai, China

Shanghai Engineering Research Center of Ultra-Precision Optical Manufacturing, Fudan University, Shanghai, China

L. Xu and L. Zhou (eds.), *Proceedings of the 8th International Multidisciplinary Conference on Optofluidics (IMCO 2018)*, Lecture Notes in Electrical Engineering 531,
https://doi.org/10.1007/978-981-13-3381-1_3

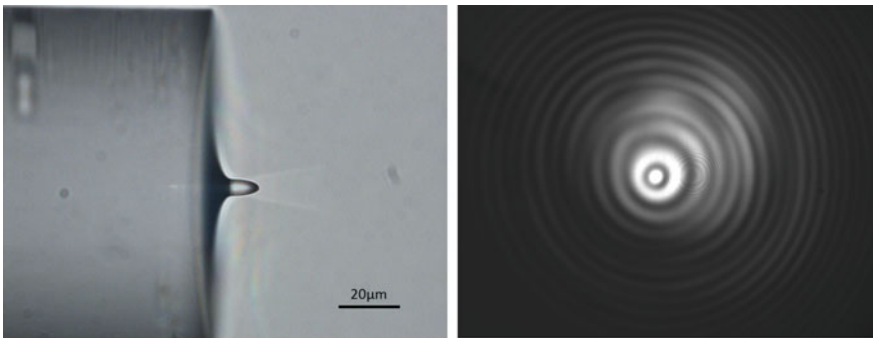

Fig. 1 **a** 100× microscopic image of a photopolymer microtip at the end of a SMF fabricated with green laser. **b** Bessel-like beam pattern from behind the fabricated microtip, measured by a CCD camera

liquid surface tension. However, we find shorter microtips are favorable for Bessel-like beams generation, so we use a dose reduction method to fabricate short microtips. The length of droplet can be reduced to around 10–20 μm after one operation. Then green laser emerging from the SMF selectively solidified external photosensitive material and therefore formed a polymer microtip.

In addition to the length, the achievement of Bessel-like beams highly depends on the shape of the microtip, which is mainly affected by photopolymer parameters, such as laser exposure time, green laser power, and oxygen diffusion concentration. After a suitable height droplet was deposited, a green laser with the wavelength of 532 nm was coupled into the SMF through a mode filter to ensure that only the fundamental mode was excited. The laser illuminated the center part of the liquid, and at this moment the far-field pattern behind the tip showed nearly a single mode. As shown in Fig. 1, after rinsed off the unreacted liquid with a few drops of ethanol, a firm microtip appeared, and the far-field pattern became Bessel-like. A tip with a base diameter of around 6.1 μm and a length of 17.4 μm could grow after the polymer droplet was exposed to the laser with the power of 1 μw for 60 s.

In the experiments, the end facet of our microtip is not round but is quite sharp similar to a polished microlens, acting as a specific microaxicon. Figure 2 shows that the Gaussian beam propagated from the SMF can be reshaped with the interference of wave vectors from different positions at the microtip end and thereby directly forming a Bessel-like beam.

In order to study the working wavelength range and the mode properties of the microtip, we directly placed the screen behind the microtip to observe the far-field patterns at different wavelengths. As shown in Fig. 3, four far-field patterns at different wavelengths were captured. High-quality Bessel-like beams of light in the wavelength range from 406 to 660 nm that covered the full visible light spectral region can be produced by our microtips, with more than 30 concentric rings. In the near-infrared spectral region, it also functions well. However, it is difficult to capture

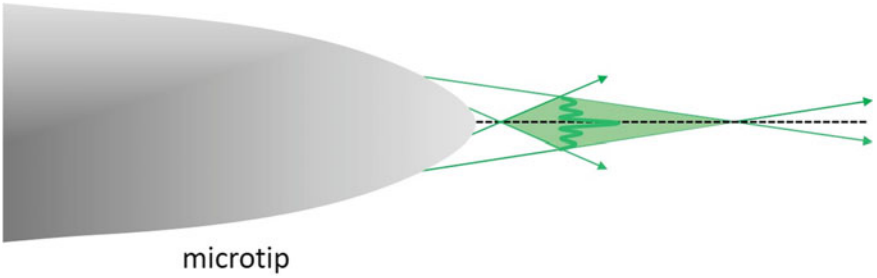

Fig. 2 Formation principle of a Bessel-like beam from the microtip illuminated by a Gaussian beam

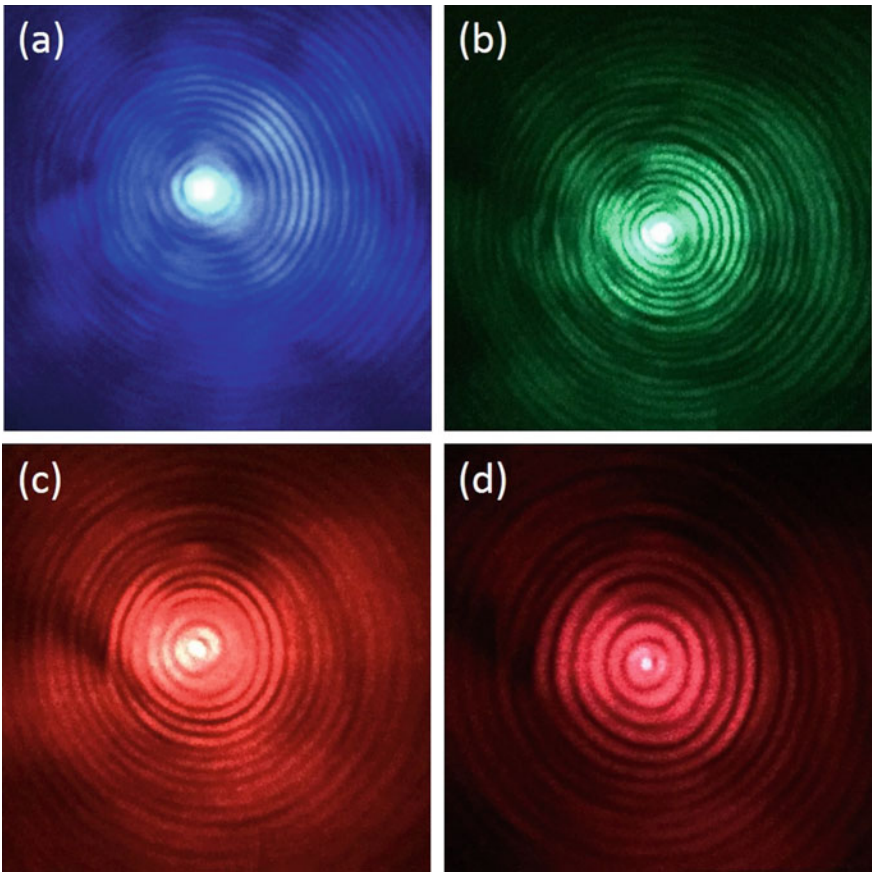

Fig. 3 Far-field patterns at four different wavelengths behind the microtips: **a** 406 nm; **b** 520 nm; **c** 638 nm; **d** 660 nm

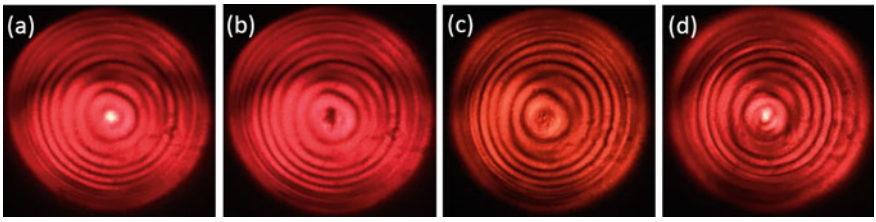

Fig. 4 **a** Light pattern without an obstacle. **b** Light pattern with an obstacle, $z = 0$ mm. **c** Light pattern after moving the unit 5.5 cm to the right, $z = 55$ mm. **d** Light pattern with the recovered central bright spot after moving the unit 10 cm further to the right, $z = 155$ mm

the entire far-field patterns because in the near-infrared CCD, we used possessed a limited photo-surface area compared with the larger screen.

We also verified the self-healing property of the Bessel-like beam. The experimental setup consists of a 40× objective lens, a glass slide with obstacle, a 10× objective lens, a camera, and a screen. The 10× objective lens, screen, and camera were placed as a unit along an axis, i.e., along the z position. As shown in Fig. 4a, we can see that the pattern on the screen was out of obstacles. When the center bright point was completely blocked, the position of the unit on the axis is used as the initial position of our measurement [Fig. 4b]. When the device was moved 5.5 cm to the right, the central point started to recover to some extent [Fig. 4c]. When the device was moved another 10 cm, the bright center has recovered [Fig. 4d].

In conclusion, we introduce an ultra-compact, convenient, low-cost, and effective approach of Bessel-like beams generation through self-growing polymer microtips. The droplet height and polymerization parameters are essential for achieving high-quality Bessel-like beam conversion. Our microtips can function in a wide spectral region with up to more than 30 concentric rings. Besides, the self-healing property of Bessel beams has been verified.

Funding National Natural Science Foundation of China (NSFC) (61475119, 61775041); Shanghai Pujiang Program (17PJ1400600); National Key R&D Program of China (2016YFC0201401).

References

1. Planchon TA, Gao L, Milkie DE, Davidson MW, Galbraith JA, Galbraith CG, Betzig E (2011) Rapid three-dimensional isotropic imaging of living cells using Bessel beam plane ill μmination. Nat Methods 8:417–423
2. Arlt J, Dholakia K, Soneson J, Wright EM (2001) Optical dipole traps and atomic waveguides based on Bessel light beams. Phys Rev A 63(6):063602
3. Kumar S, Sotillo B, Chiappini A, Ramponi R, Di Trapani P, Eaton SM, Jedrkiewicz O (2017) Study of graphitic microstructure formation in diamond bulk by pulsed Bessel beam laser writing. Appl Phys A 123:698
4. Eah S-K, Jhe W (2003) Nearly diffraction-limited focusing of a fiber axicon microlens. Rev Sci Instrum 74(11):4969–4971

5. Cabrini S, Liberale C, Cojoc D, Carpentiero A, Prasciolu M, Mora S, Degiorgio V, De Angelis F, Di Fabrizio E (2006) Axicon lens on optical fiber forming optical tweezers, made by focused ion beam milling. Microelectron Eng 83(4–9):804–807
6. Zhu X, Schülzgen A, Peyghambarian N (2009) Generation of controllable nondiffracting beams using multimode optical fibers. Appl Phys Lett 94(20):201102
7. Steinvurzel SP, Tantiwanichapan K, Goto M, Ramachandran S (2011) Fiber-based Bessel beams with controllable diffraction-resistant distance. Opt Lett 36(23):4671–4673
8. Bachelot R, Ecoffet C, Deloeil D, Royer P, Lougnot DJ (2001) Integration of micrometer-sized polymer elements at the end of optical fibers by free-radical photopolymerization. Appl Opt 40(32):5860–5871

Design of SiN-Based Mode-Size Converter for Single-Photon Communication

Juan Hu, Xiao ling Chen, Qing Fang, and Feng Song

Abstract SiN-based mode-size converter with high coupling efficiency and low polarization loss has been designed, in which length is 98.7 μm. The simulated coupling efficiency for TE mode is 87%, and the simulated coupling efficiency for TM mode is 81%. It is polarization-insensitive when the converter coupled with single-mode fiber at the wavelength of 800 nm. For both TE and TM mode, the 1-dB bandwidths are 34 nm and 32 nm, respectively, and the alignment tolerance for 1-dB excess loss is ±0.8 μm in the horizontal and vertical directions. The core part of converter is supported with SiO_2 beams to prevent light leaking from the substrate, and this converter can compress spot and couple it into the SiN waveguide effectively and smoothly.

Keywords Silicon photonics · Single-photon communication · Mode-size converter

1 Introduction

Quantum communication is one of the most popular research areas in the world, and single-photon detectors are the core components for implementing quantum teleportation systems which are based on single-photon transmission. Si is a good choice for the preparation of detectors, but the absorption coefficient of Si is higher at the wavelength of 800 nm, which is not conducive to the transmission of signals, but the transmission loss of silicon nitride at this wavelength is low [1], so SiN is selected as an optical transmission medium for the on-chip optical path of the quantum optical communication. When the wavelength is 800 nm, the mode field diameter of the silicon nitride linear waveguide is very small, and when it is directly coupled with

J. Hu · X. Chen · Q. Fang (✉)
Kunming University Science and Technology, Yunnan, China
e-mail: semioelab@kmust.edu.cn

F. Song
School of Science, Xi'an Polytechnic University, Xi'an, China

L. Xu and L. Zhou (eds.), *Proceedings of the 8th International Multidisciplinary Conference on Optofluidics (IMCO 2018)*, Lecture Notes in Electrical Engineering 531,
https://doi.org/10.1007/978-981-13-3381-1_4

the single-mode fiber, a large extra loss may occur due to the mismatch of mode field diameters. In order to solve the huge coupling loss in direct coupling, scientists have proposed and produced high-performance converters with high coupling efficiency and low polarization loss. There are surface coupling based on grating couple and edge coupling based on inverse taper. In 2011, Fang [2] produced a Si waveguide-based converter with 1-dB bandwidth of TE and TM modes are more than 120 nm. Jia [3] uses silicon nitride with refractive index is 1.5 as an intermediate material and is combined with reverse tapered and cantilever structures to reduce mismatch losses when coupled with single-mode fiber. In 2015, the IBM [4] made O-band metamaterial coupler and transmission loss achieved −1.3 dB between standard single-mode fiber and silicon nano-waveguide; however, this cantilever-type converter length is about 875 μm, which is quite long for silicon photonic devices. In 2016, our group [5] produced cantilever-type converter with good performance such as low coupling loss, uncorrelated wavelength, and wide bandwidth.

2 Converter Design

As shown in Fig. 1, we have designed a mode-size converter that is tapered in the horizontal direction. The key structure of the entire converter is supported by SiO_2 beams, and this suspended design prevents light signal leaking from the substrate which reduces coupling loss. Etching only in the horizontal direction makes the manufacturing steps and processes simpler.

The mode-size converter can be divided into three parts along the propagation direction. The first part is a SiO_2 rectangular waveguide that connects with the single-mode fiber, the second part is a taper that tapered in the horizontal direction, and the third part is composed of SiN reverse taper that embedded in the middle of SiO_2 waveguide. The compressed spot is further pressed into the SiN waveguide when optical signal propagates to the third part. We set the thickness of the buried oxide layer as 2 μm, since the diameter of the single-mode fiber is between 4 and 6 μm at 800 nm, and we choose the size of SiO_2 waveguide that connected to the single-mode fiber to be 5 μm × 5 μm. We use a Gaussian light with wavelength of 800 nm as the launching field to launch into single-mode fiber and calculate fundamental

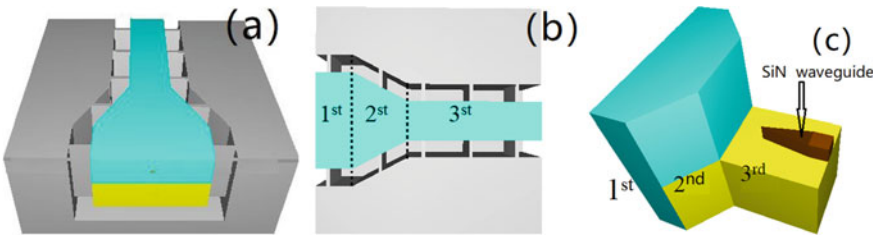

Fig. 1 Structural schematic diagram of converter **a** Main view, **b** top view, **c** core structure

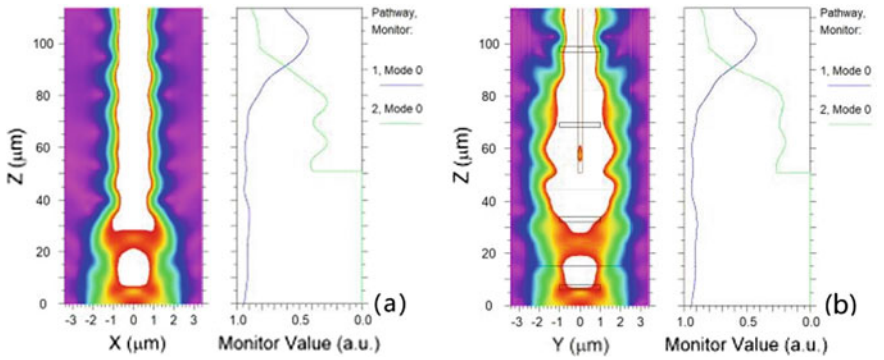

Fig. 2 Simulation of the optical path and data monitoring **a** *XZ* cross section, **b** *YZ* cross section. (Green line shows the energy in SiN. Blue line shows the energy in SiO_2)

mode, and the obtained fundamental mode is used to couple with SiO_2 rectangular waveguide of the converter.

In the third part, since the refractive index of silicon nitride is larger than the refractive index of silicon dioxide, the light energy is gradually pressed into the silicon nitride waveguide. The optical path of light propagating is simulated by Rsoft software in the mode-size converter, as shown in Fig. 2. When the light travels in the *Z*-axis direction, the spot is significantly smaller and its size is compressed horizontally into the SiN waveguide. For both TE and TM mode, coupling efficiency are 86 and 81%.

In order to obtain the optimal size of converter more accurately, we placed two monitors to monitor the optical field energy in SiO_2 and silicon nitride waveguide, respectively. We have obtained the coupling efficiency by changing the height, width, and length of the silicon nitride tapered waveguide as shown in Fig. 3. Figure 3a, b shows the coupling efficiency as the change of height and width of the SiN waveguide, and Figure 3c shows the variation of the coupling efficiency with the width of the SiN waveguide. From these figures, we can see that the coupling efficiency reaches the highest when the height, length, and width of the SiN waveguide taper are 0.2 μm × 48 μm × 0.15 μm. Calculate some parameters by simulation, second cladding

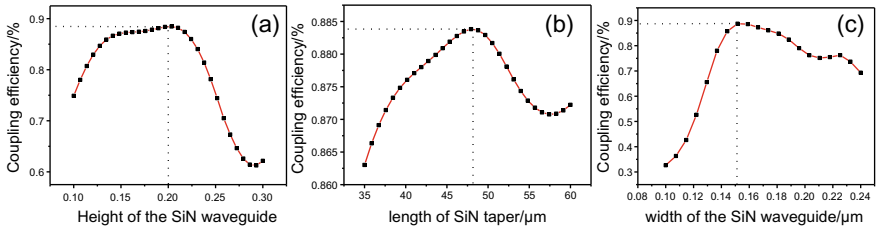

Fig. 3 Coupling efficiency varies with **a** height of the SiN, **b** length of SiN taper, **c** width of the SiN

SiO_2 taper length is 29.5 μm, second width of the end of cladding SiO_2 taper is 2.28 μm, third pitch of SiN waveguide tip and end of second is 6.2 μm, and the highest coupling efficiency can be achieved.

In order to obtain performance parameters of the converter, we simulated and calculated the device's alignment tolerance and the coupling efficiency that varies with wavelength. Figure 4 shows the coupling efficiency with the variation of offset, and the alignment tolerance that produces 1-dB extra loss in the horizontal and vertical directions are ±0.8 μm. Figure 5 shows the change of coupling efficiency as a function of wavelength, Fig. 5 shows the coupling efficiency with the change of wavelength, for both TE and TM mode, the 1 dB bandwidths are 34 and 32 nm.

Finally, we designed a cantilever-type mode-size converter which operates at 800 nm with high coupling efficiency and low polarization loss. The heart of the converter is supported by SiO_2 beams, and it has neither vertical taper nor vertical etching.

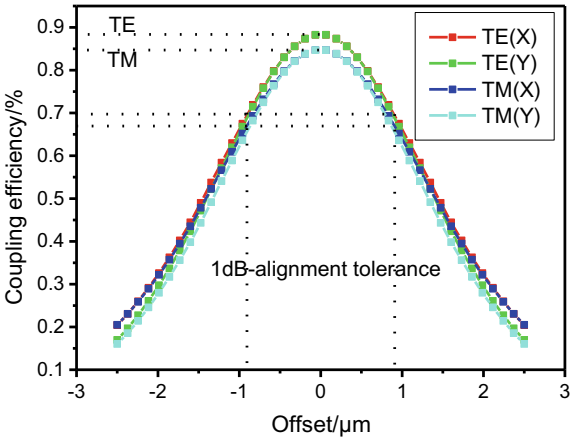

Fig. 4 Change of coupling efficiency with offset

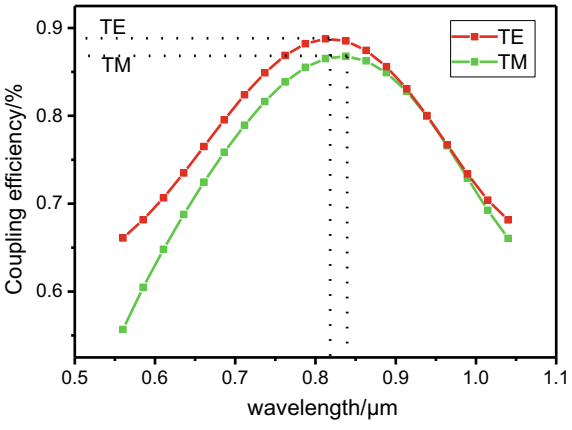

Fig. 5 Change of coupling efficiency with wavelength

Acknowledgements This work was supported by the National Natural Science Foundation of China (No. 61764008 and No. 61674072) and by the Opened Fund of the State Key Laboratory of Integrated Optoelectronics No. IOSKL2017KF11, Natural Science Foundation of Shanxi Province of China (Grant Nos. 2017JM6075), Foundation of Shaanxi Provincial Education Department (Grant Nos. 17JK0335), and Foundation of State Key Laboratory of Functional Materials for Informatics (Grant Nos. SKL201804).

References

1. Ting HU, Dong B, Luo X, Liow TY, Song J, Lee C, Guo-Qiang LO (2017) Silicon photonic platforms for mid-infrared applications [invited]. Photon Res 5(5):417
2. Fang Q, Song J, Luo X, Yu M, Lo G, Liu Y (2011) Mode-size converter with high coupling efficiency and broad bandwidth. Opt Express 19(22):21588–21594
3. Jia L, Song J, Liow TY, Luo X, Tu X, Fang Q, Koh SC, Yu M, Lo G (2014) Mode size converter between high-index-contrast waveguide and cleaved single mode fiber using SiON as intermediate material. Opt Express 22(19):23652
4. Barwicz T, Jantapolczynski A, Khater M, Yan T, Leidy R, Maling J, Martel S, Engelmann S, Orcutt JS, Fortier P (2015) An O-band metamaterial converter interfacing standard optical fibers to silicon nanophotonic waveguides. In: Optical fiber communications conference and exhibition, pp 1–3
5. Fang Q, Song J, Luo X, Tu X, Jia L, Yu M, Lo G (2016) Low loss fiber-to-waveguide converter with a 3-D functional taper for silicon photonics. IEEE Photon Technol Lett 28(22):2533–2536

Graphene-Microfiber and Its Application on Photonic Devices and Lasers

Xiaoying He, Anqi Hu, X. Guo, and C. Li

Abstract Graphene-microfiber with the advantage of graphene material and microfiber has been hailed as a wonderful optical waveguide. In this paper, its fabrication, optical properties and applications have been presented. Here, we present our recent progress in the graphene-microfiber waveguides from photonic devices, e.g., optical polarizers and optical modulators to mode-locking in fiber laser. With the novel nanotechnology emerging, graphene-microfiber could offer new possibilities for the future optic circuits, systems and networks.

Keywords Graphene · Microfiber · Polarizer · Modulator · Mode-locked fiber laser

1 Introduction

Graphene has attracted significant attentions, due to a variety kind of excellent photonic and electronic properties [1]. Graphene, as two-dimensional (2D) hexagonal lattice forms of carbon, has been made as an ideal material for utilizing in the field of nano-electronics, devices and sensors. Because of its unique electronic structure and linear dispersion, the monolayer graphene has a constant absorption per unit mass of the semiconductor material (2.3%) across the visible and infrared range [2]. Compared to other optical materials, graphene has ultrafast carrier dynamics response over ultra-broad-band spectral range. The Pauli blocking effect enables it to exhibit many remarkable nonlinear optical properties such as saturable absorptions, high Kerr nonlinearity (nonlinear refractive index change), two-photon absorption, four-wave mixing (FWM) and so on. Furthermore, it can be controlled through electrical

X. He (✉) · A. Hu · X. Guo
School of Electronic Engineering, and State Key Laboratory of Information Photonics and Optical Communications, Beijing University of Posts and Telecommunications, Beijing 100876, China
e-mail: xiaoyinghe@bupt.edu.cn

C. Li
Schools of Information, Beijing University of Technology, Beijing 100124, China

L. Xu and L. Zhou (eds.), *Proceedings of the 8th International Multidisciplinary Conference on Optofluidics (IMCO 2018)*, Lecture Notes in Electrical Engineering 531,
https://doi.org/10.1007/978-981-13-3381-1_5

gating to shift the Fermi level for controlling the optical absorption. As an atomically thin film, it can also be flexible to integrate with the microfiber or other optical waveguides for wide applications on optical polarizers, modulators, mode-locked fiber lasers and so on.

Microfiber as one-dimensional (1D) micro/nano-scale waveguide with strong evanescent fields and ultra-tight optical confinement can effectively collect and launch the evanescent light to couple with other materials. In the microfiber, its large evanescent light enables strong or rapid near-field interaction with graphene, thus leading to so many potential applications. Here, we report our recent progress about the graphene-microfiber including its optical properties, fabrication and applications on photonic devices and lasers. We will start from the fundamentals of the graphene-microfiber, and then move to its applications. Finally, a brief outlook for opportunities and challenges of the graphene-microfiber in the future has been presented.

2 Fundamental of Graphene-Microfiber

2.1 Structure and Fabrication

To date, the structure of our designed graphene-microfiber is shown in Fig. 1, where the graphene film is tightly covered on the microfiber and the MgF_2 substrate. The microfiber is fabricated by flame-heated taper-drawing technology [3] with the diameter down to micro/nano-scale. This technique could realize the tapering profile optimization and cross-section geometric control, and effectively decrease the propagation loss of the microfiber. Here, the fabrication process of the graphene-microfiber is in the following. The graphene film is grown on the surface of Cu or Ni by chemical vapor deposition (CVD) method, and then the low refractive index PMMA or ultraviolet glue is spin-coated on the graphene film surface. The polymer/graphene/metal sandwich structure is formed. To remove the metal layer, it can be soaked into the $FeCl_3$ solution with a long time. Subsequently, the polymer-supported graphene washes in deionized water several times and covered on the microfiber with the MgF_2 substrate. The PMMA or UV glue could be removed by acetone for our consideration. Then, we put it in a box to dry at room temperature for 12 h. Finally, the graphene-microfiber waveguide, as shown in Fig. 1, has been obtained.

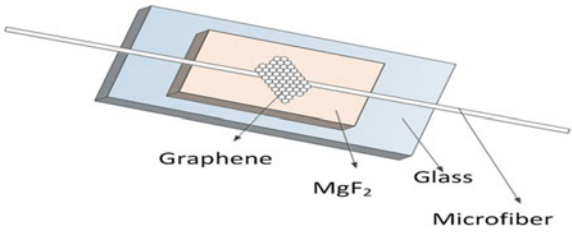

Fig. 1 Graphene-microfiber structure with graphene covered on the microfiber

2.2 Properties of Graphene Covered on the Microfiber

The dynamical conductivity σ_g of graphene should be considered in the Maxwell's equations for analyzing the effective refractive index of graphene and its optical field. The conductivity of graphene is related to radian frequency (ω), chemical potential (μ_c), the relaxation time (τ) and temperature (T), which is calculated from the Kubo formula:

$$\sigma_g(\omega, \mu_c, \Gamma, T) = \frac{je^2(\omega - j\tau^{-1})}{\pi\hbar}\frac{1}{(\omega - j\tau^{-1})^2}\int_0^\infty \varepsilon\left(\frac{\partial f_d(\varepsilon)}{\partial\varepsilon} - \frac{\partial f_d(-\varepsilon)}{\partial\varepsilon}\right)d\varepsilon$$
$$- \frac{je^2(\omega - j\tau^{-1})}{\pi\hbar}\int_0^\infty \frac{f_d(-\varepsilon) - f_d(\varepsilon)}{(\omega - j2\Gamma)^2 - 4(\varepsilon/\hbar)^2}d\varepsilon \quad (1)$$

where e is the charge of an electron, $\hbar = h/2\pi$ is the reduced Planck's constant, $f_d(\varepsilon) = \left(e^{(\varepsilon-\mu_c)/k_BT} + 1\right)^{-1}$ is the Fermi–Dirac distribution and k_B is Boltzmann's constant. The first term in Eq. (1) is evaluated as the intraband conductivity, and the second is due to the interband contribution. The permittivity of the graphene is related to the conductivity as $\varepsilon_g = \varepsilon_0 - \sigma_{g,i}/\omega d + j\sigma_{g,r}/\omega d$ [4], where $\sigma_{g,i}$ and $\sigma_{g,r}$ are the imaginary and real part of the conductivity of graphene σ_g, d is the thickness of the graphene film and ω is the light's angular frequency. Figure 2 shows nonlinear saturable absorption of single-layer graphene measured by using picosecond pulse laser. Due to the graphene asymmetrically covered on the microfiber, when different polarized light pass through the graphene-microfiber, it presents polarization-dependence property on the nonlinear saturable absorption. This asymmetrical graphene-microfiber structure can be used as polarizer and modulator.

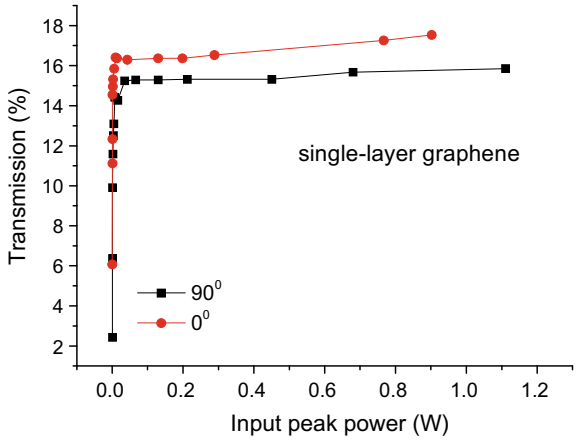

Fig. 2 Nonlinear saturable absorption of single-layer graphene

3 Applications of the Graphene-Microfiber

3.1 Photonic Devices Applications

Graphene-microfiber has broadband all-optical modulating, which can realize the modulation rate from 1 MHz [5] to 200 GHz [6]. Here, we use polarization-dependent graphene-microfiber structure to realize modulation [7] and polarization [8]. By changing the place of the core, a flexible graphene-microfiber polarizer can be obtained with high polarization extinction ratio of ~30 dB [8]. Because of the cross-absorption modulation effects of graphene [7], a 1480 nm pump light with a series of 100 Gbit/s RZ signals and 8-wavelength polarized continuous wave probe lights simultaneously come into the graphene-microfiber for generating 8 channel polarization-dependent modulated lights with 100Gbit/s RZ signals. *X*-polarized and *Y*-polarized modulated lights have different modulation depth of ~14.8 and ~14.88 dB. The modulation depth of the *y*-polarized light is larger than that of *x*-polarized. This means that such a modulator is remarkably suitable for the prominent application on digital community antenna television signal broadcast (Fig. 3).

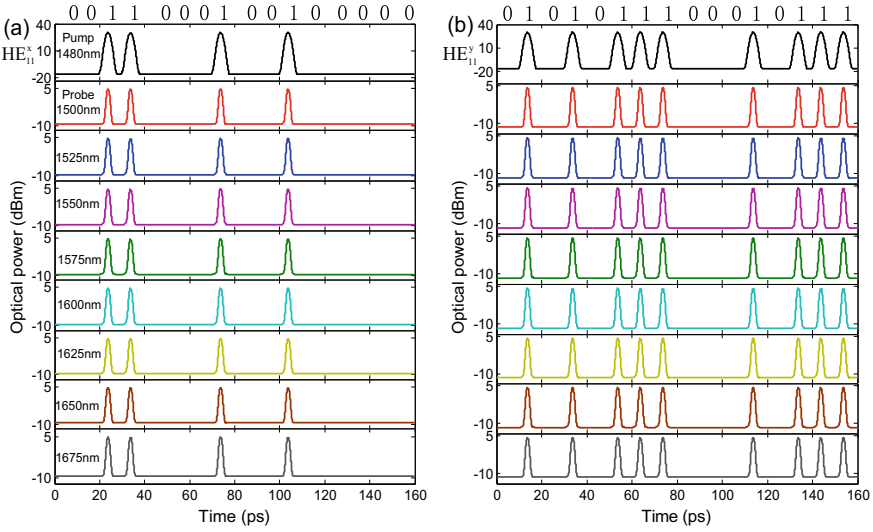

Fig. 3 Nonlinear saturable absorption of single-layer graphene [7]

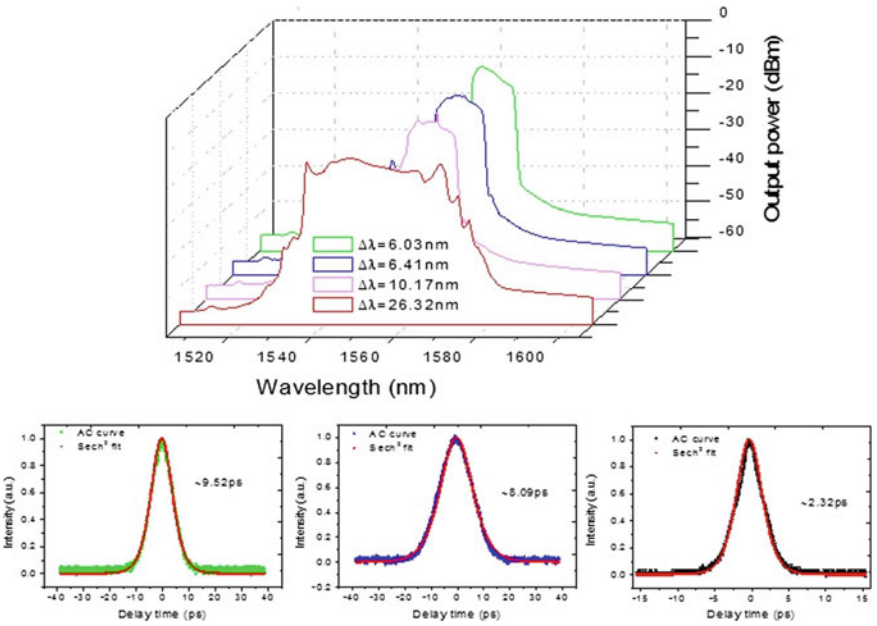

Fig. 4 Output pulses and their 3 dB spectra [11]

3.2 Mode-Locked Fiber Laser Applications

In 2012, we used the reduced graphene oxides on the microfiber for passive mode-locking in Erbium-doped fiber laser to generate wide-band doublet pulses [9]. Subsequently, the chirped fiber grating can be introduced into the mode-locking fiber laser with graphene-microfiber. Wavelength-tunable pulses can be realized from 1550 to 1550 nm with pulse-width about 20 ps [10]. By tuning the polarization of the light propagated in the graphene-microfiber, pulse-width tunable pulses can be obtained in the fiber laser from ~9.24 to ~2.32 ps with 3 dB spectral bandwidth from ~6.03 to 26.32 nm [11], as shown in Fig. 4.

4 Conclusion

Graphene-microfiber, as a novel fiber-based device not only can be used as saturable absorber in the fiber laser for mode-locking, but also can be opened up to new opportunities in photonic devices such as modulator, polarizer and so on. All these applications are due to the interaction between the strong evanescent optical field in the microfiber and the nonlinear saturable absorption with tunable chemical potential in the graphene. Except the above, graphene has another superior feature, e.g., large nonlinear Kerr effect, FWM, two-photonic absorption, electrically tuning the Fermi

level and surface plasmon effect. When the graphene with these features is integrated with the microfiber, some new potential applications such as super-resolution imaging, optical sensor and so on can be realized.

Acknowledgements The project is supported by National Natural Science Foundation of China (Number 61675046) and the Fundamental of Research Funds for the Center Universities (No. 2019PTB-006).

References

1. Bonaccorso F, Sun Z, Hasan T, Ferrari AC (2010) Graphene photonics and optoelectronics. Nat Photon 4(9):611–622
2. Acouris P (2010) Graphene electronic and photonic properties and devices. Nano Lett 10(11):4285–4294
3. Tong L, Lou J, Mazur E (2004) Single-mode guiding properties of subwavelength-diameter silica and silicon wire waveguides. Opt Express 12(6):1025–1035
4. Wu Y, Yao B, Zhang A, Rao Y, Wang Z, Cheng Y, Gong Y, Zhang WL, Chen YF, Chiang KS (2014) Graphene-coated microfiber Bragg grating for high-sensitivity gas sensing. Opt Lett 39(5):1235–1237
5. Liu Z, Feng M, Jiang W, Xin W, Wang P, Sheng Q, Liu Y, Zhou W, Tian J (2013) Broadband all-optical modulation using a graphene microfiber. Laser Phys Lett 10(6):065901
6. Li W, Chen B, Meng C, Fang W, Xiao Y, Li X, Hu Z, Xu Y, Tong L, Wang H, Liu W, Bao J, Shen YR (2014) Ultrafast all-optical graphene modulator. Nano Lett 14(2):955–959
7. He X, Xu M, Zhang X (2016) Theoretical investigation of a broadband all-optical graphene-microfiber modulator. J Opt Soc Am B 33(12):2588–2595
8. He X, Liu J (2017) Flexible and broadband graphene polarizer based on surface silicon-core microfiber. Opt Mater Express 7(4):1398–1405
9. He X, Liu Z, Wang D, Yang M, Liao CR, Zhao X (2012) Passively mode-locked fiber lasers based on reduced graphene oxide microfiber for ultra-wide-band doublet pulse generation. J Lightwave Technol 30(7):984–989
10. He X, Liu Z, Wang D (2012) Wavelength-tunable, passively mode-locked fiber laser based on graphene and chirped fiber Bragg grating. Opt Lett 37(12):2394–2396
11. He X, Wang D, Liu Z (2014) Pulse-width tuning in a passively mode-locked fiber laser with graphene satruable absorber. IEEE Photon Technol Lett 26(4):360–363

Groove in Sapphire Machined by CO_2 Laser Under Water

Leilin Huang, Lei Xiao, Fufei Pang, Huanhuan Liu, Xianglong Zeng, and Tingyun Wang

Abstract We have demonstrated a method for crack-free machining of groove in sapphire by using a CO_2 continuous-wave (CW) laser under water. A sapphire wafer with a thickness of 1 mm is immersed into the water with 1 mm beneath the water surface. The effect of laser processing parameters on the jagged edge size and groove depth has been analyzed by tuning line-to-line spacing ranging from 0.006 to 0.1 mm as well as scanning speeds from 5 to 80 mm/s. As the decreasing of line-to-line spacing and the increasing of scanning speed, the jagged edge size reduces. The groove depth is deeper as the increasing of line-to-line spacing and scanning speed. Since underwater laser machining reduces substrate defects originated from heat accumulation from the laser, a groove without recast layer and cracking could be formed in sapphire wafer. The achieved groove in sapphire shows potential application for optical fiber sensing in harsh environments and microfluidic channels in corrosive solutions.

Keywords Groove · Sapphire · CO_2 laser

1 Introduction

The machining of groove in sapphire has broad application prospects in many fields [1]. Particularly, in optical fiber sensing, the formation of groove can be used as a Fabry–Perot cavity that has been shown to be highly sensitive to temperature and pressure [2], especially in high temperature environments. Since sapphire is an extremely hard and corrosion-resistant crystal with a melting point of over 2000 °C, the machining of groove in sapphire shows great potential in harsh environments and provides the possibility for the application of microfluidic channels in corrosive solutions. The processing of such material by picosecond and femtosecond

L. Huang · L. Xiao · F. Pang (✉) · H. Liu · X. Zeng · T. Wang
Key Laboratory of Specialty Fiber Optics and Optical Access Networks, Joint International Research Laboratory of Specialty Fiber Optics and Advanced Communication, Shanghai Institute for Advanced Communication and Data Science, Shanghai University, Shanghai 200444, China
e-mail: ffpang@shu.edu.cn

L. Xu and L. Zhou (eds.), *Proceedings of the 8th International Multidisciplinary Conference on Optofluidics (IMCO 2018)*, Lecture Notes in Electrical Engineering 531,
https://doi.org/10.1007/978-981-13-3381-1_6

ultrashort pulse lasers shows high photon loss and low material removal [3]. In contrast, sapphire has a high absorption coefficient of 95% for a CO_2 laser emitted at 10.6 μm [4]. Meanwhile, CO_2 laser underwater machining has been found to result in reducing substrate defects such as recast layer and cracking that are typically found in machining in air [5].

In this paper, the effect of laser processing parameters on the jagged edge size and groove depth is analyzed by laser machining in sapphire wafer with different line-to-line spacing and scanning speeds. The achieved groove in sapphire shows potential application for optical fiber sensing in harsh environments and microfluidic channels in corrosive solutions.

2 Experimental Investigation

The experiment setup for CO_2 laser underwater machining system is shown in Figure 1a. It consists of a computer-controlled CO_2 CW laser associated with an *x-y* galvanometer beam scanner and a sample container with water. A 53 × 25 × 1 mm sapphire wafer is immersed into the water with 1 mm beneath the water surface. A groove with a diameter of 3 mm is machined into the sapphire. Figure 1b illustrates the interaction between CO_2 laser, water and sapphire wafer.

Figure 2 shows the micrographs of the jagged edge morphology with line-to-line spacing ranging from 0.006 to 0.1 mm. As the distance between the lines decreases,

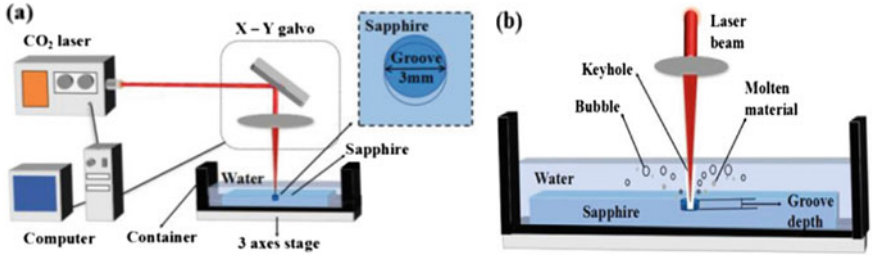

Fig. 1 **a** Schematic diagram of experimental setup for underwater machining of sapphire, **b** interaction between CO_2 laser, water and sapphire

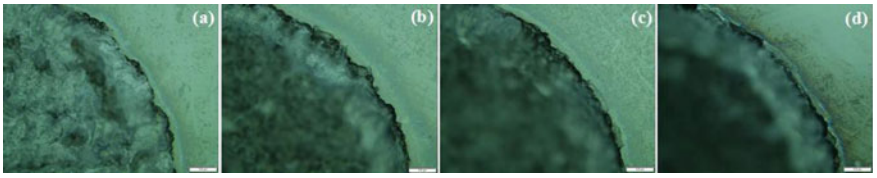

Fig. 2 Micrographs of jagged edge morphology at a line-to-line spacing of **a** 0.1 mm, **b** 0.04 mm, **c** 0.01 mm, **d** 0.006 mm. Scale bars are 100 μm

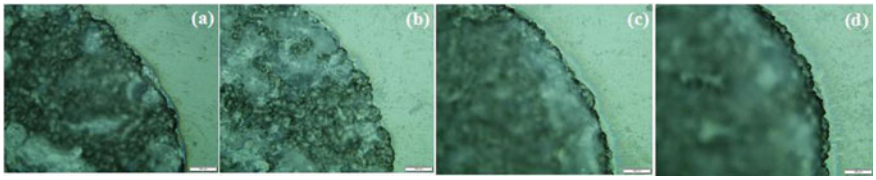

Fig. 3 Micrographs of jagged edge morphology at a scanning speed of **a** 80 mm/s, **b** 50 mm/s, **c** 10 mm/s, **d** 5 mm/s. Scale bars are 100 μm

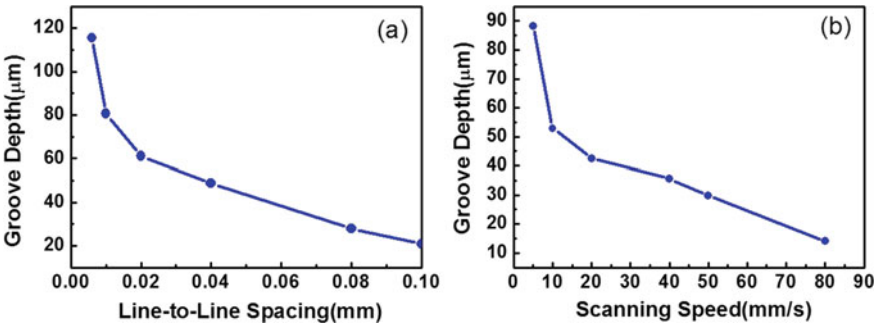

Fig. 4 Groove depth under different **a** line-to-line spacing, **b** scanning speed

the overlap rate of the spots on the edge increases and the jagged edge reduce. The jagged edge morphology with scanning speed ranging from 5 to 80 mm/s is shown in Fig. 3, which indicates that the jagged edge size reduces along with the decreasing heat accumulation induced by speed increasing.

Figure 4a plots the groove depth measured by 3D Optical Profiler (S neox) under different spacing. As the spacing becomes smaller, the thermal accumulation in unit is higher so that and the depth of groove is deeper. The groove depth under different scanning speeds is shown in Fig. 4b. The increase of the material's removal rate caused by the extension of the machining time which is resulted from the speed decreasing, deepen the groove depth eventually.

3 Conclusion

In summary, we realize the CO_2 laser underwater machining of grooves in sapphire and investigate the influence of line-to-line spacing and scanning speed on jagged edge size and groove depth. The achieved groove in sapphire shows potential application for optical fiber sensing in harsh environments and microfluidic channels in corrosive solutions.

Acknowledgements This project was funded by National Key Research and Development Program of China (2016YFF0100600); National Natural Science Foundation of China (Grants 61735009 and 61422507).

References

1. Griffin BA, Mills DA, Schmitz T, Sheplak M (2011) A sapphire based fiber optic dynamic pressure sensor for harsh environments: fabrication and characterization. In: 49th AIAA aerospace sciences meeting including the new horizons forum and aerospace exposition. AIAA, Orlando, FL, USA, pp 4–7
2. Yi J, Lally E, Wang A, Xu Y (2011) Demonstration of an all-sapphire Fabry–Pérot cavity for pressure sensing. IEEE Photon Technol Lett 23(1):9–11
3. Juodkazis S, Nishimura K, Misawa W (2007) In-bulk and surface structuring of sapphire by femtosecond pulses. Appl Surf Sci 253(15):6539–6544
4. Zhang W, Guo Y, Yan F, Gao T (2016) Study on thermodynamics damage characteristics of sapphire from CW Laser. Aero Weaponry 41(2):52–55
5. Yan Y, Li L, Sezer K, Wang W, Whitehead D, Ji L, Baob Y, Jiang Y (2011) CO_2 laser underwater machining of deep grooves in alumina. J Euro Ceram Society 31(15):2793–2807

High-Efficient Generation of Nonlinear Optical Effects in Semiconductor Nanowaveguides

Jiaxin Yu, Yuanguang Cao, Fang Liu, and Fuxing Gu

Abstract Nonlinear optical effects, including second- and third-harmonic generation, and multi-photon luminescence, are found to be excited much more efficiently via evanescent wave coupling. Taking this advantage, we establish a microfiber-based compact device to extract the magnitude and phase information of ultrafast pulse laser. The sensitivity of this configuration can be down to femto-joule level.

1 Introduction

Semiconductor nanowaveguides (NWs), such as ZnO nanowires [1], CdSe nanobelts [2], and GaSe [3] nanoribbons, have drawn a widespread attention as nonlinear optical (NLO) media. The large refractive index and scale effect offer them the ability to strongly confine the light within a sub-micron scale. Recently, the evanescent wave coupling (EWC) technique is emerging as an efficient method for NLO optical excitation [4, 5]. We here demonstrate enhanced efficiencies for second-harmonic and third-harmonic generation (SHG/THG) and multi-photon luminescence (MPL) via this waveguide excitation. Particularly, second-order stronger MPL in intensity can be obtained from a single CdSe nanowaveguide, in contrast to that generated by free-space excitation, which can be hardly seen under the same excitation power.

2 Materials and Experimental Setup

The NWs used here were all synthesized via vapor-liquid-solid processes. The optical image and scanning electron microscopy show the nanostructures with smooth surface and good uniformity along the longitudinal direction. EWC technique is

J. Yu (✉) · Y. Cao · F. Liu · F. Gu
Key Laboratory of Modern Optical System, Engineering Research Center of Optical Instrument and System (Ministry of Education), University of Shanghai for Science and Technology, Shanghai 200093, China
e-mail: yujiaxin@usst.edu.cn

L. Xu and L. Zhou (eds.), *Proceedings of the 8th International Multidisciplinary Conference on Optofluidics (IMCO 2018)*, Lecture Notes in Electrical Engineering 531,
https://doi.org/10.1007/978-981-13-3381-1_7

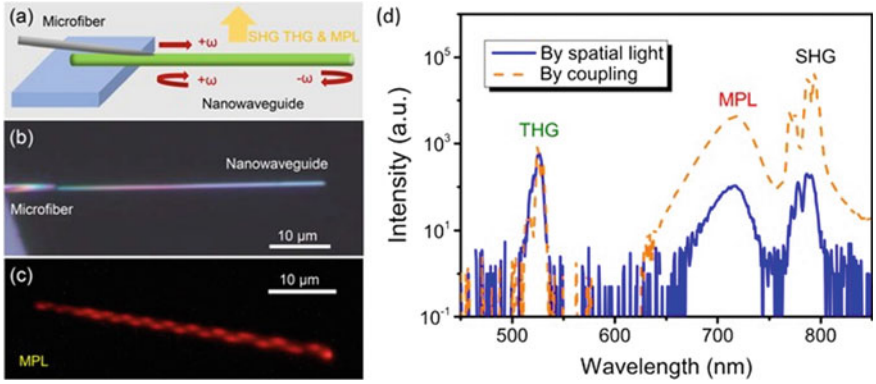

Fig. 1 High-efficient generation of SHG, THG, and MPL via evanescent wave coupling

sketched in Fig. 1a. Briefly, individual NW was picked up and placed on the edge of a MgF_2 substrate, protruding out for tens of micrometers. A microfiber tapered from a standard optical fiber (SMF-28, Corning) was attached to the NW firmly via Van der Waals and electrostatic attractions, as shown in Fig. 1b. In this way, the excitation laser can be coupled from optical fiber into the NW with up to 90% efficiency. For comparison, a spatial light excitation regime is also implemented by focusing the laser on to the suspended NW through a 50× objective lens, which also worked for epi-detection in both excitation regimes.

3 Results and Discussion

We compared the NLO response of the two excitation regime, and the spectra results under the same input power are presented in Fig. 1d. It is obvious that the intensities of all three NLO effects are stronger under the EWC excitation. Specifically, the MPL from an individual NW was hardly observed under spatially focused excitation regime, while under EWC excitation, the MPL emission showed a bright and distinct pattern, as shown in Fig. 1c.

The enhancements of NLO effects can be attributed to two reasons. On one aspect, after coupled into a NW, the light is confined in a scale beyond the diffraction limit, leading to a much higher energy density within the nanostructure. On the other, the light–material interaction distance is largely augmented as the light guiding along the NW. Both aspects will benefit the generation of NLO effects. Provided the high signal-to-noise ratio by waveguide excitation, we thus observe a fourth-order excitation power dependence of three-photon luminescence, and we attribute it to surface defect mechanism based on the recombination of free carriers [2].

Taking the advantage of the high efficiency in NLO generation, we further developed a configuration by coupling pulsed laser from both ends of a NW simultaneously, so that a SHG-based frequency-resolved optical gating method for ultrafast

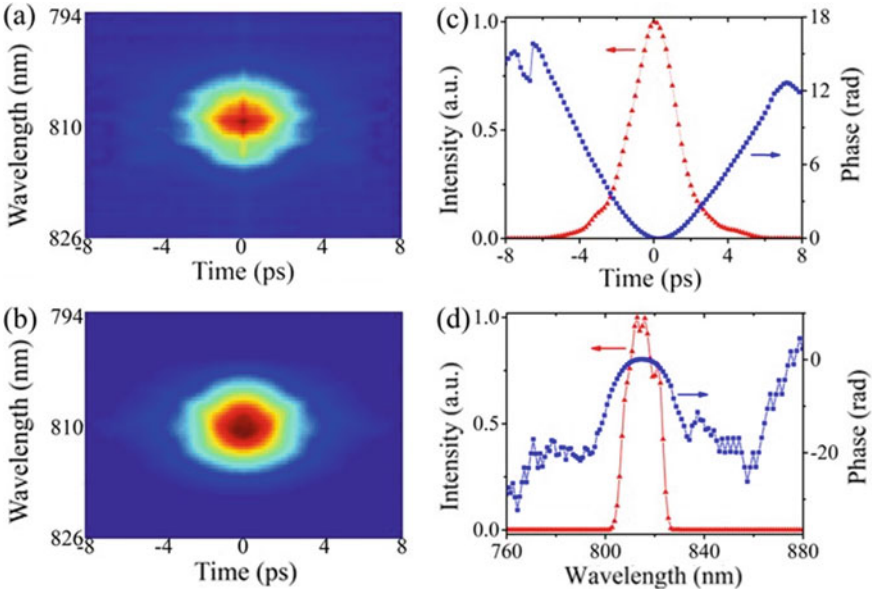

Fig. 2 Pulse measurement and retrieval results of 810 nm pulses by microfiber-nanowaveguide configuration

pulse measurement can be practiced in this compact device. The phase and amplitude of a pulse series are extracted as shown in Fig. 2, and the sensitivity can reach down to femto-joule [1, 3]. This microfiber-NW geometry is compatible with standard fiber system and may promote the functionalization of nonlinear optical circuits in the future.

References

1. Yu J, Liao F, Gu F, Zeng H (2016) Frequency-resolved optical gating measurement of ultrashort pulses by using single nanowire. Sci Rep 6:33181
2. Yu J, Liu F, Gu Z, Gu F, Zhuang S (2018) Efficient higher-order nonlinear optical effects in CdSe nanowaveguides. Opt Exp 26:6880–6889
3. Liao F, Wang Y, Peng T, Peng J, Gu Z, Yu H, Chen T, Yu J, Gu F (2018) Highly efficient nonlinear optical conversion in waveguiding GaSe nanoribbons with pump pulses down to a femto-joule level. Adv Opt Mater 6:1701012
4. Gu F, Zhang L, Wu G, Zhu Y, Zeng H (2014) Sub-bandgap transverse frequency conversion in semiconductor nano-waveguides. Nanoscale 6:12371–12375
5. Gu F, Cui H, Liao F, Lin X, Wang H, Zeng H (2016) Mode tailoring in subwavelength-dimensional semiconductor micro/nanowaveguides by coupling optical microfibers. Opt Exp 24:23361–23367

Influence of Electromagnetic Characteristics of Sodium Chloride on Temperature Change During Microwave Drying

Junjiang Chen, Weijun Wang, Huan Lin, and Hua Chen

Abstract Since the effect of microwave heating is closely related to the electromagnetic parameters of the material, the heated material often exhibits selective heating. This article uses a multi-mode microwave resonant cavity to heat sodium chloride. The finite difference time domain (FDTD) method was used to simulate the electromagnetic field and thermal field equation in the microwave heating process. The heating rate of microwave heating sodium chloride was changed in real time with the change of the electromagnetic characteristic parameters. The analysis results show that with the increase of the relative permittivity of sodium chloride, the electric field intensity of sodium chloride in the cavity increases, the heating rate increases, and the distribution of the electromagnetic field becomes more uniform.

Keywords Finite difference time domain · Relative dielectric constant · Heating rate · Electric field distribution

1 Introduction

Compared with traditional heating, microwave heating as a clean and efficient green energy has been widely used in many fields [1–4]. The effective heating object of microwave drying is mainly the small amount of water to be dried. Because the effect of microwave heating is closely related to the electromagnetic characteristic parameters of the material, it is very important to study the electromagnetic properties of the material during microwave heating with the change of temperature. Li Pengfei and Xie Gaijun used the FDTD method to establish the electromagnetic-thermal coupling model of ceramic microwave heating [5]. Zhu J et al. analyzed the effect of dielectric properties on the temperature distribution by studying continuous fluid

J. Chen · W. Wang · H. Lin · H. Chen (✉)
Faculty of Science, Kunming University of Science and Technology, Kunming 650500, China
e-mail: 93056460@qq.com

H. Chen
Key Laboratory of Unconventional Metallurgy, Ministry of Education, Kunming University of Science and Technology, Kunming 650500, China

L. Xu and L. Zhou (eds.), *Proceedings of the 8th International Multidisciplinary Conference on Optofluidics (IMCO 2018)*, Lecture Notes in Electrical Engineering 531,
https://doi.org/10.1007/978-981-13-3381-1_8

microwave heating [6]. Torres F and Jecko B et al. studied the relationship between the dielectric parameters and the temperature rise of heated objects. The effects of dielectric parameters on microwave heating have been obtained [7].

In order to study the relationship between electromagnetic properties and dielectric parameters of sodium chloride in microwave drying process. In this paper, the time domain finite difference method is used to simulate the heating rate of sodium chloride in the resonant cavity with the electromagnetic characteristic parameters. The relationship between the dielectric parameters of sodium chloride and the heating rate and electric field distribution at different temperatures was obtained.

2 Electromagnetic-Thermal Coupling

In the electromagnetic coupling process, it is divided into two parts: electromagnetic calculation and heat transfer. The FDTD algorithm takes the Yee grid as the discrete element of the electromagnetic field and converts the Maxwell curl equations into differential equations so that the electromagnetic fields are alternately distributed in time and space.

$$\nabla \times \overrightarrow{H} = \frac{\partial \overrightarrow{D}}{\partial t} + \overrightarrow{J} \tag{1}$$

$$\nabla \times \overrightarrow{E} = \frac{\partial \overrightarrow{B}}{\partial t} - \overrightarrow{M} \tag{2}$$

where $\overrightarrow{H}$ is the electric field strength; $\overrightarrow{D}$ is the electric displacement; $\overrightarrow{E}$ is the magnetic field strength; $\overrightarrow{B}$ is the magnetic flux density; $\overrightarrow{J}$ is the current density; $\overrightarrow{M}$ is the magnetic current density.

The medium in the cavity absorbs the electromagnetic wave in the heating process and converts the absorbed electromagnetic wave into a heat source, that is

$$P = \sigma |E|^2 = 2\pi f \varepsilon_0 \varepsilon_r' \tan\delta |E|^2 \tag{3}$$

where σ is the effective conductivity of the entire material system ($\sigma = \omega\varepsilon'' \tan\delta$) and the imaginary part of the complex permittivity of the material. E is the electric field strength in the cavity. ε_0 is the dielectric constant of the material without external electric field. ε' is the relative permittivity. f is the microwave frequency. tan δ is the dielectric loss tangent. Reflects the ability of the medium to absorb microwave energy [8].

At time t, the temperature change at the interior point (x, y, z) of the medium satisfies the heat conduction equation;

$$\rho C_m \frac{\partial T(x, y, z, t)}{\partial t} = k_t \nabla^2 T(x, y, z, t) + P(x, y, z, t) \tag{4}$$

where ρ is the dielectric density. C_m is the specific heat capacity. k_t is the thermal conductivity. P is the heat flux, which is equivalent to the heat source at that point. Using FDTD grid form of discrete, for $\Delta x = \Delta y = \Delta z = \Delta$, Material absorption of microwave energy into heat energy after the heating rate;

$$\frac{dT}{dt} = \frac{2\pi f \varepsilon_0 \varepsilon_r' \tan\delta |E|^2}{\rho c_p}$$

Among them T, ρ, c_p and t are the material temperature, density, constant pressure mass specific heat capacity and heating time.

The main research of microwave electromagnetic-thermal model is that the electromagnetic calculation and the thermal process should be organically combined by an appropriate method so that the actual object can be accurately simulated. The microwaves act on the object being heated and generate microwave losses, therein the energy of the microwave losses being converted into heat. The heat of conversion in the thermal model in the form of heat transfer in the object, the temperature distribution of the object changes, the temperature changes will lead to the object of the dielectric constant and other relevant parameters change, so that the entire electromagnetic field distribution also followed by recalculation, changes in electromagnetic field values make the microwave loss also make the corresponding changes, so repeatedly until the end of the simulation.

3 Numerical Results and Discussion

During the heating process, the medium absorbs electromagnetic waves and converts the absorbed electromagnetic waves into heat sources. The ability of medium to absorb microwave depends mainly on dielectric parameters. Therefore, in this paper, the electromagnetic sensitivity of dielectric parameters is studied. The model of the study is shown in the following figure. The model consists of a resonant cavity and a transmission waveguide (Fig. 1).

The length, width and height of the resonator in the model are 200 mm, 100 mm and 100 mm, respectively. Transmission waveguide length, width and height dimensions were 43, 140 and 22 mm. In this paper, the source of excitation is the differential Gaussian pulse source, and the uniaxial perfectly matched layer (UPML) is its boundary condition with the center frequency of 2.45 GHz. In the calculation of modeling and calculation of convenience, the use of equal-interval discrete. Microwave heating process, the material warmed, will change the internal structure of the heated material, resulting in the dielectric properties of the material being heated changes. This will in turn affect the absorption efficiency of microwaves by the material being

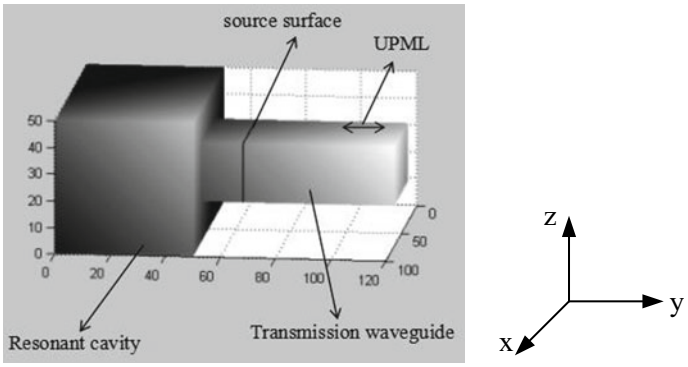

Fig. 1 Structure model of waveguide loaded resonator

heated. Therefore, the influence of the dielectric properties of the material to be heated on the microwave heating effect needs to be considered.

3.1 The Influence of Temperature on the Electric Field Distribution of Sodium Chloride

Considering the influence of different dielectric parameters on the electromagnetic field distribution of sodium chloride during microwave drying. According to Table 1, the dielectric parameter, dielectric loss and loss tangent values at 4% sodium chloride are listed, and the variation of the electromagnetic field of the sodium chloride at the working frequency of 2.45 GHz in the cavity.

Figure 2 shows when the excitation source is fed from the *x-o-z* plane, at a time step of 3000. The MATLAB software is used to calculate the distribution of the electric field in the cavity of the cavity at the temperature of 20 °C, 60 °C and 80 °C, respectively, under the condition of the boundary condition and the excitation source of the cavity are not changed. With the temperature of sodium chloride increases, the dielectric parameter also increases. From Fig. 2 can be seen, when the sodium chloride in the cavity is 20 °C, its electric field distribution shows a clear standing wave state. When 60 °C sodium chloride is added into the cavity, the electric field

Table 1 Dielectric parameters of aqueous 4% sodium chloride at different temperatures at 2.45 GHz [9]

T/°C	20	30	40	50	60	70	80	90	100
ε'	4.55	4.62	4.75	4.81	5.00	5.29	5.48	5.83	6.15
ε''	1.70	1.80	1.97	2.33	2.67	3.14	4.13	5.42	7.65
tan δ	0.37	0.39	0.42	0.48	0.55	0.59	0.75	0.92	1.24

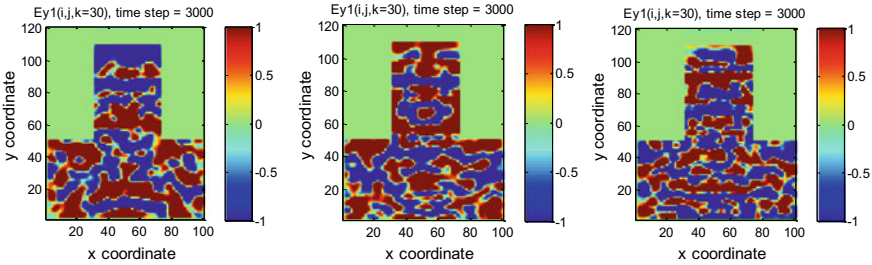

Fig. 2 Distribution of electric field of sodium chloride in cavity at different temperatures

distribution change significantly and is more uniform. When the cavity is filled with sodium chloride with a higher relative permittivity, the temperature is 80 °C, and the distribution of the electric field is more uniform than that of the sodium chloride at 60 °C. Therefore, it can be seen that when the cavity is filled with sodium chloride at different temperatures, and the electric field distribution in the cavity is more uniform with the increase of the dielectric parameter of sodium chloride.

3.2 Electromagnetic Susceptibility Analysis of Dielectric Parameter for Sodium Chloride Heating Rate

At the same time, the relationship between heating rate and heating time of sodium chloride with different dielectric parameters in the cavity was calculated. The dielectric parameter was 4.55, 5.0 and 5.48, respectively. As shown in Fig. 3, as the heating time increases, the heating rate of sodium chloride continues to increase. When the running time is 400 times steps, the heating rate of sodium chloride changes rapidly, and the heating rate tends to be gentle with the heating time. This is mainly due to the weakening of the electromagnetic field inside the cavity and the change of the thermophysical parameters. The weakening of the electromagnetic field may be due to the change in the permeability of the material in the cavity, so that most of the microwaves emitted by the microwave source are reflected back into the microwave source, thus, reducing the electromagnetic field strength inside the cavity. However, the final temperature increase of sodium chloride will tend to balance and remain unchanged. It shows that with the change of the dielectric parameter of the medium in the cavity, the heating rate in the cavity will also change.

4 Conclusion

Based on the FDTD method to establish thermal coupling model electromagnetic Maxwell equations and the heat conduction equation. This article simulates

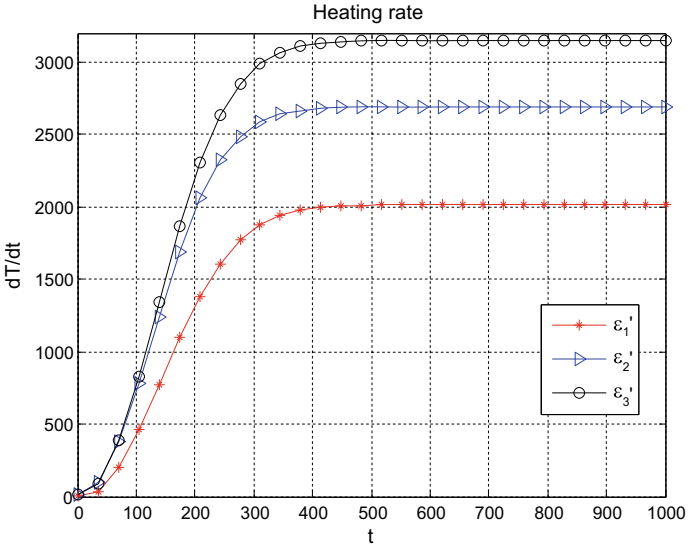

Fig. 3 Temperature rising rate in the cavity of different dielectric parameter

a different dielectric parameter heating rate in sodium chloride. The heating rate curve of sodium chloride was obtained. Raising the temperature of sodium chloride can significantly improve the absorption characteristics of sodium chloride, and then converting electromagnetic energy into heat energy to promote faster temperature rise of sodium chloride and rapid heating and drying.

Acknowledgements This research is funded by the National Natural Science Foundation (Project No. 51304097), Yunnan Provincial Fund Project (Project No. 2013FZ016), Key Project of Yunnan Provincial Department of Education (Project No. 2015Z026), Yunnan Provincial Key Program of Applied Basic Research Projects (Project No. 2015FA017).

References

1. Wenxiang W (2009) Microwave engineering technology. National Defence Industry Press, Beijing, pp 1–5
2. Jie L, Bangwen Z, Baowei L (2010) Experimental study on process of microwave magnetizing roast plus magnetic separation for medium-low grade oxidized ores containing hematite of Bayan obo. Metal Mine 407(5):89–91
3. Ying T (2007) Numerical modeling study of microwave heating CaO-SiO_2 system materials. Wuhan University of Technology, Wuhan
4. Xiaoqing Y, Kama H (2006) Investigation of key problems of interaction betweenmicrowave and chemical reaction. J Radio Sci 21(5):802–809
5. Pengfei LI (2010) Study of microwave heating model based on ADI-FDTD. University of Electronic Science and technology of China, Chengdu

6. Zhu J, Kuznetsov AV, Sandeep KP (2007) Mathematical modeling of continuous flow microwave heating of liquids (effects of dielectric properties and design parameters). Int J Therm Sci 46(4):328–341
7. Torres F, Jecko B (1997) Complete FDTD analysis of microwave heating processes in frequency-dependent and temperature-dependent media. IEEE Trans Microwave Theor Tech 45(1):108
8. Kama H et al (1996) New characteristics of oxido-reduction reaction of KI and $KMn0_4$ irradiated by amplitude-modulated electromagnetic waves. Chin Sci Bull 41(15):1259–1262
9. Chenhui L (2014) Study on new technology of microwave heating based on dielectric properties of metallurgical materials. Kunming University of Science and Technology, Kunming

Metasurfaces for Band-Pass Filter in Ka-Band

Yue Li, Bowen Yang, Huijie Guo, Qiushi Li, and Shiyi Xiao

Abstract This paper establishes a coupled-mode theory (CMT) to help understand the inherent physics governing the transmission properties of a band-pass filter, based on which a two-layer metasurface exhibiting a wide band pass in Ka-band is designed. This method can be easily extended to other frequency regimes.

Keywords Coupled-mode theory · Metasurface · Band pass · Ka-band

1 Introduction

Recently, plasmonic systems have attracted a lot of attention due to their application in practice and scientific. Direct and indirect coupling of optical resonators enable open plasmonic open systems to achieve light manipulation through restructuring of eigenstates with contrasting Q factors, while exhibiting many fascinating optical phenomena, such as Fano resonance, Rabi oscillation, and plasmon-induced transparency (PIT). This method was employed in the design of a band-pass filter working at X-band [1].

In this paper, we employ a coupled-mode model to design a band-pass filter based on two-layer metasurfaces in Ka-band. By analyzing the two-layer metasurfaces using coupled-mode theory [2, 3], we discover that the crucial properties (i.e., position and bandwidth) of each transmission peak within the band pass are solely determined by a particular set of model parameters describing both the inter-layer near-field couplings and the far-field radiations. Our theory is fully justified by both full-wave simulations and microwave experiments.

Y. Li · B. Yang · Q. Li · S. Xiao (✉)
Key Laboratory of Specialty Fiber Optics and Optical Access Networks, Shanghai University, Shanghai 200072, China
e-mail: phxiao@shu.edu.cn

H. Guo
Physics Department and State Key Laboratory of Surface Physics, Fudan University, Shanghai 200433, China

L. Xu and L. Zhou (eds.), *Proceedings of the 8th International Multidisciplinary Conference on Optofluidics (IMCO 2018)*, Lecture Notes in Electrical Engineering 531,
https://doi.org/10.1007/978-981-13-3381-1_9

2 Coupled-Mode Theotry

We start our discussion with a typical electromagnetic metasurface structure. As shown in Fig. 1, the metasurface structure is comprised of two identical layers printed with periodic arrays of subwavelength metallic structures, and the substrate is F4B ($\varepsilon = 2.2$ and $h = 0.2$ mm). Each layer is composed of a metallic Jerusalem cruciform resonator surrounded by a metallic mesh and the distance between the two layers is. The metallic mesh is optically opaque, and the two resonators induce optical transparency at two resonating frequencies [4].

Figure 2 illustrates the CMT model of such a system, which consists of 2 scattering channels and 2 modes embedded inside an opaque background. These two modes are contributed by the localized Jerusalem cruciform resonators.

By "turning off" the optical mode's radiation toward the scattering channel, the resonator amplitude $\alpha_j (j = 1, 2)$ can be expressed as

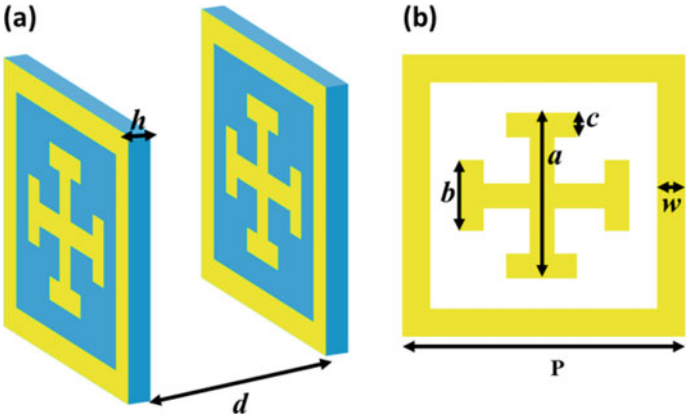

Fig. 1 **a** Schematic diagram of metal structures stacked in space, where blue represents a dielectric substrate with $\varepsilon = 2.2$, $h = 0.2$ mm, and d is the distance between two metal structures. **b** A unit of metal structure, $P = 3.5$, $\omega = 0.25$, $\alpha = 2$, $b = 1$, $c = 0.3$, all in units of mm

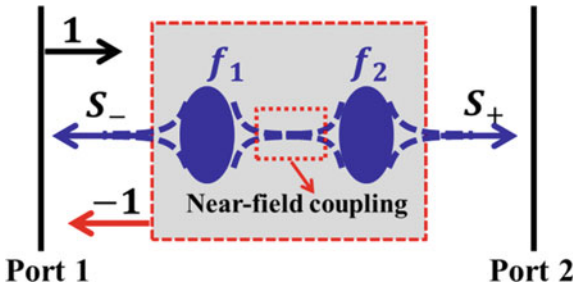

Fig. 2 A schematic diagram of the CMT model showing the two ports and two resonators

$$\frac{1}{2\pi}\frac{d}{dt}\begin{pmatrix}\alpha_1\\ \alpha_2\end{pmatrix} = i\widehat{H}\begin{pmatrix}\alpha_1\\ \alpha_2\end{pmatrix} = i\begin{pmatrix}f_0+\kappa' & \kappa\\ \kappa & f_0+\kappa'\end{pmatrix}\begin{pmatrix}\alpha_1\\ \alpha_2\end{pmatrix} \tag{1}$$

where f_0 denotes the resonating frequency of resonator, κ and κ' denote the near-field coupling [5, 6].

Through unitary transformation, $\widehat{H}$ can be diagonalized as

$$\widetilde{H} = M.\widehat{H}.M^T = \begin{pmatrix}\widetilde{f}_s & 0\\ 0 & \widetilde{f}_a\end{pmatrix} = \begin{pmatrix}f_0+\kappa+\kappa' & \kappa\\ \kappa & f_0-\kappa+\kappa'\end{pmatrix} \tag{2}$$

where $M = \frac{1}{\sqrt{2}}\begin{pmatrix}-1 & 1\\ 1 & 1\end{pmatrix}$. We have proved that if $MM^T = I$, the constraint of CMT parameters would not change.

Therefore, we can apply the CMT model to obtain the formula as

$$\frac{1}{2\pi}\frac{d}{dt}\begin{pmatrix}\widetilde{\alpha}_s\\ \widetilde{\alpha}_a\end{pmatrix} = i\begin{pmatrix}\widetilde{f}_s & 0\\ 0 & \widetilde{f}_a\end{pmatrix}\begin{pmatrix}\widetilde{\alpha}_s\\ \widetilde{\alpha}_a\end{pmatrix} + \begin{pmatrix}-\widetilde{\Gamma}_s & \widetilde{X}\\ \widetilde{X} & -\widetilde{\Gamma}_a\end{pmatrix}\begin{pmatrix}\widetilde{\alpha}_s\\ \widetilde{\alpha}_a\end{pmatrix} + \begin{pmatrix}\tilde{d}_{1s}\\ \tilde{d}_{1a}\end{pmatrix}S_1 \tag{3}$$

where $\tilde{d}_{1i}$ denotes the coupling between the collective mode and the port.

$(r_0 = -1, t_0 = 0)$, we can use the standard two-mode two-port CMT to analyze the transmission coefficient of the two-layer system [1, 7]. By referring to the standard CMT, the transmission coefficient can be approximately expressed as

$$t \approx \frac{\widetilde{W}_a\tilde{d}_{1,s}\tilde{d}_{2,s} + \widetilde{W}_s\tilde{d}_{1,a}\tilde{d}_{2,a} + \widetilde{X}\left(\tilde{d}_{1,s}\tilde{d}_{2,a} + \tilde{d}_{2,s}\tilde{d}_{1,a}\right)}{\widetilde{W}_s\widetilde{W}_a - \widetilde{X}^2} \tag{4}$$

where $\widetilde{W}_j = i\left(f - \tilde{f}_j\right) + \widetilde{\Gamma}_j$ and $\tilde{f}_j$ and $\widetilde{\Gamma}_j$, respectively, denote the resonance frequency and the damping caused by radiations of the two ports. Here $j = s, a$ definer the symmetrical (s) or antisymmetrical (a) mode. $\tilde{d}_{1,j}$ and $\tilde{d}_{2,j}$ $(j = s, a)$ denote the couplings between the jth mode and the two ports, and $\widetilde{X}$ describes the interactions between the two resonant modes. $\widetilde{X}$ and $\widetilde{\Gamma}_j$ are not independent parameters, since $\widetilde{X} = -\left(\tilde{d}^*_{1,s}\tilde{d}_{1,a} + \tilde{d}^*_{2,s}\tilde{d}_{2,a}\right)/2$ and $\widetilde{\Gamma}_j = \left(\left|\tilde{d}_{1,j}\right|^2 + \left|\tilde{d}_{2,j}\right|^2\right)/2$ according to the CMT [2].

The curve shown in Fig. 3a is the best-fitted CMT spectra.

With parameters given by $\widetilde{\Gamma}_a = 2.3$, $\widetilde{\Gamma}_s = 5.1$, $\tilde{f}_a = 36.9$ and $\tilde{f}_s = 28.6$, all in units of GHz. We note that in the limit of $X = 0$, Eq. (4) can be further simplified as $t = \frac{\tilde{d}_{1,s}\tilde{d}_{2,s}}{\widetilde{W}_s} + \frac{\tilde{d}_{1,a}\tilde{d}_{2,a}}{\widetilde{W}_a}$, which describes the responses of the two independent oscillators. We then calculate the transmission spectra contributed by the symmetrical $(j = s)$ and antisymmetrical $(j = a)$ modes separately, and plot them in Fig. 3b. We find that

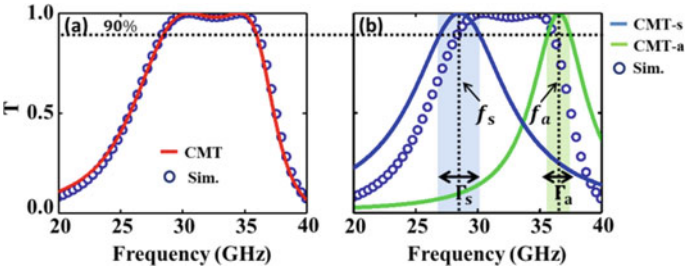

Fig. 3 **a** Results of the two-layer structure transmittance FDTD and CMT fitting, where, **b** bandwidth of collective symmetric and antisymmetrical mode fit the simulated spectra

the position and the bandwidth of the *j*th transmission peak can be described by $\tilde{f}_j$ and $\widetilde{\Gamma}_j$.

In order to understand this two-layer system, we repeated the CMT analyses on a series if two-layer systems with different inter-layer distance d, and retrieved the corresponding CMT parameters in different cases. Figure 4a–c illustrates the relationship between CMT parameters and inter-layer distance d. It can be clearly seen in Fig. 4a that κ and κ' decrease as d increases, so tuning d can change the near-field coupling. In return, the near-field coupling can control the peak width of the two peaks, as shown in Fig. 4b. Figure 4d depicts the FDTD simulated transmission spectra for different distance d.

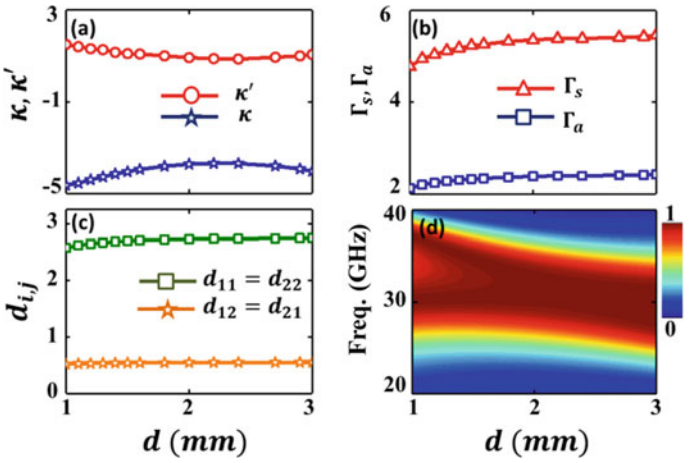

Fig. 4 Retrieved CMT fitting parameters of the two-layer metasurface: **a** coupling coefficients (κ, κ'); **b** bandwidths of two peaks $\widetilde{\Gamma}_a$, $\widetilde{\Gamma}_s$ (blue and red symbols); **c** damping parameters ($d_{i,j}$) as function of inter-layer distance; **d** distance dependence of transmittance spectra computed by FDTD simulations

3 Conclusions

We have established a highly efficient approach to designing an optical band-pass filter based on the coupled-mode theory. We have established that the peak positions and the peak width in the transmission spectrum of a coupled two-layer metasurface are closely related to the collective modes and can be described by near-field coupling. Based on the coupled-mode theory, we have designed a structure that can serve as a band-pass filter in Ka-band with 28.6–36.9 GHz.

Our design approach is robust, intuitive, fast and can have many applications in practice.

References

1. Guo H, Lin J, Qiu M et al (2018) Flat optical transparent window: mechanism and realization based on metasurfaces. J Phys D Appl Phys 51(7):074001
2. Fan S, Suh W, Joannopoulos JD (2003) Temporal coupled-mode theory for the Fano resonance in optical resonators. JOSA A 20(3):569–572
3. Haus HA (1984) Waves and fields in optoelectronics. Prentice-Hall
4. Zhou L, Wen W, Chan CT et al (2005) Electromagnetic-wave tunneling through negative-permittivity media with high magnetic fields. Phys Rev Lett 94(24):243905
5. Xu H, He Q, Xiao S et al (2011) Tight-binding analysis of coupling effects in metamaterials. J Appl Phys 109(2):023103
6. Xi B, Xu H, Xiao S et al (2011) Theory of coupling in dispersive photonic systems. Phys Rev B 83(16):165115
7. Qiu M, Xiao S, He Q et al (2015) Experimental verifications on an effective model for photonic coupling. Opt Lett 40(2):272–275

Miniaturized Refractometer Based on Wedge Interferometry for Handheld Testing Devices

Noha Gaber

Abstract Interferometric methods are known for their high sensitivity for biochemical optical sensing, but at the expense of their large size. However by using wedge interferometry, the size can be drastically reduced while maintaining adequate detection capabilities. In this work, a miniaturized refractometer based on this interferometer type is experimentally tested to be able to achieve sensitivity of 1.66×10^{-5} *RIE*/μm and detection limit of 8.7×10^{-5} *RIE* for bulk refractometry of glucose aqueous solutions. The device consists of two semitransparent mirrors made of glass slides coated by sputtered aluminum thin films, enclosing a tapered frame that maintains one mirror slightly tilted with respect to the other, and simultaneously encloses the liquid under test. Analytical modeling estimation of the sensitivity shows that it can exceed the state of the art for volume refractometry and can be achieved upon using microfabrication techniques. The proposed novel device opens a new avenue for optofluidic detection and is very suitable for point-of-care-testing and handheld devices due to its compact size, simple and cheap fabrication.

Keywords Miniaturized refractometer · Optofluidic sensor · Wedge interferometer

1 Introduction

Optical refractometry is well known for being label-free and real-time method for identifying dielectric materials by measuring their refractive index (RI); thereby, it has various industrial, environmental and biomedical applications. With the wide interest in microfluidics and laboratory-on-a-chip systems, several attempts have been done, trying to integrate various optical detection techniques on-chip [1]. A lot of refractometry methods have the possibility to be easily included into the micro-size system, but most of them still need external bulky expensive equipment such as optical spectrum analyzers or surface-enhanced Raman spectrometers [2]. Using spatial interferometry techniques evades using such bulky equipment, and only a

N. Gaber (✉)
Zewail City of Science and Technology, 6th of October City, Giza, Egypt
e-mail: ngaber@zewailcity.edu.eg

L. Xu and L. Zhou (eds.), *Proceedings of the 8th International Multidisciplinary Conference on Optofluidics (IMCO 2018)*, Lecture Notes in Electrical Engineering 531,
https://doi.org/10.1007/978-981-13-3381-1_10

camera is required for imaging; therefore, they are exhibiting a growing interest. Interferometry techniques generally are trusted for their high detection capabilities. The reason behind their high sensitivity is the accumulation of the phase difference along the beam traveling distance of the interferometer arms [3]. But inherently, increasing the arms' length implies large size apparatus to provide the high sensitivity, which is not suitable for portable devices. This is not necessarily the case with the wedge interferometry configuration introduced in this work. In wedge interferometry, the slope of one mirror with respect to the other also controls this issue, overcoming the large size problem.

In the literature, Young interferometer (YI) configuration holds the record for highest sensitivity for both surface and bulk refractometry. Surface refractometry depends on the evanescent field that passes through the liquid touching the surface of the device. The resolution of these techniques is superior, which are capable of detecting refractive index changes (Δn) as small as 9×10^{-9} *RIU* in case of YI configuration [3]. For volume refractometry, the sensitivity is generally less, but it is more immune to surface contamination as the light passes through the test liquid itself. A Y-branch on-chip configuration could give sensitivity of 2.5×10^{-7} $RIU/\mu m$ and Δn of 1×10^{-7} *RIU* [4]. The size of these devices is usually in the order of decimeters and only available as a benchtop equipment. In this work, a compact size, cheap and simple refractometer based on wedge interferometry is proposed. The modeling of this configuration proves its ability to achieve high sensitivities with much less sizes than accomplished previously. The experimental demonstration of the refractometry performance is also presented.

2 Proposed Structure

The schematic of the proposed structure is shown in Fig. 1a. It consists of a Fabry–Pérot cavity with variable gap thickness, implemented by two mirrors in front of each other with one of them tilted with respect to the other by a designed tilting

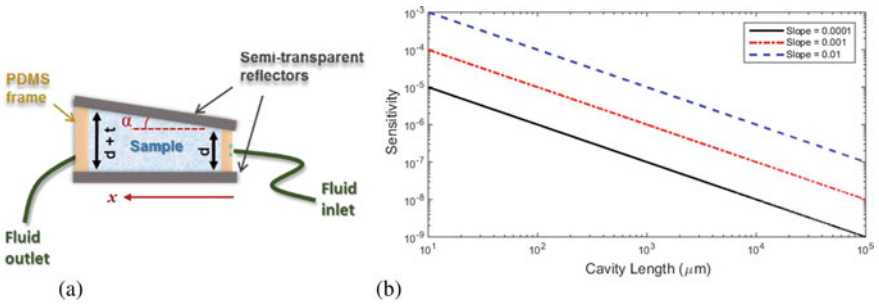

Fig. 1 **a** Schematic diagram of the proposed wedge interferometer for liquid refractometry. **b** Logarithmic plot for the sensitivity against the cavity length for different values of the slope

angle. The tilting is maintained by a fluidic chamber with a variable height made of polydimethylsiloxane (PDMS) polymer. It has a height of (d) from one side and a height of ($d + t$) from the other side. This frame is sandwiched between two semi-reflecting mirrors. Due to the varying height of the frame, one mirror is tilted by an angle (α) with respect to the other mirror. Input/output fluidic tubes are connected to deliver the liquid under test to the device. When a collimated monochromatic light is incident on this varying length resonator, the cavity length (ℓ) at some regions will be equivalent to multiples of $\lambda/2$ forming constructive interference and hence a bright fringe at the output due to perfect phase matching between the multiple reflected rays between the two mirrors. The phase difference will change gradually with moving along the mirror tilt until a completely destructive interference occurs producing a dark fringe at the output. The lines of bright-dark will be repeated successively, whose periodicity and width depend on the title angle α. Upon introducing a fluid sample with certain RI (n_s) inside the chamber, the optical path length of the resonator will be changed to ($\ell.n_s$), causing shift in the interference fringes' pattern. The sensitivity can be determined by the formula in Eq. (1).

$$\text{Sensitivity} = \frac{\delta n_s}{\delta x} = -\frac{n_s}{\ell} S = \frac{S.n_s}{S.x + d} \tag{1}$$

where S is the slope of the tilted mirror and is related to the tilt angle by the relation $S = \tan(\alpha)$. This equation can be used to predict the performance of the sensor with certain design parameters as indicated in Fig. 1b, which plots the sensitivity versus the cavity length for different values of the slope. It is explicit that increasing the cavity length and decreasing the slope achieve higher performance. For example, a slope of 0.001 and a resonator length of 1 *cm* can theoretically achieve sensitivity of 10^{-7} *RIE/*μm, which is better than the state of the art of volume refractometry presented in the introduction, even with much less size. With tolerating longer lengths of few centimeters and smaller slope of 0.0001, beating the state-of-the-art surface refractometer is even possible. But that requires precise dimension control.

3 Experimental

Semi-reflecting mirrors are fabricated by sputtering aluminum thin film on cleaned glass slide covers. The tilted chamber is fabricated by mixing the PDMS gel with its curing agent in a dish that is left for curing on an optical table to ensure flat leveling. The dish is elevated from one side only by putting beneath it a glass slide (thickness $\pm$ 0.5 mm) to produce variable thickness PDMS film with certain tilt angle. After curing, the PDMS is cut in square pieces equivalent to the mirror size, and an opening is cut inside to produce a room for the liquid sample. Two fluidic tubes are connected through the frame for sample delivery and disposal. Then finally, the two mirrors are bonded from top and bottom of the PDMS frame. A green laser pointer with a good collimated beam has been used to illuminate the device, and the produced

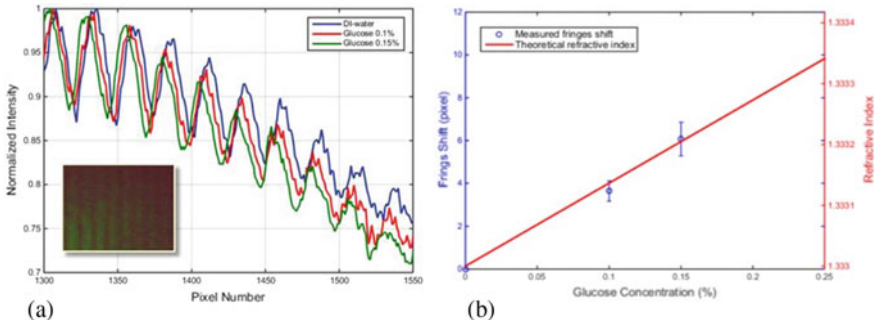

Fig. 2 **a** Interference patterns for DI water and glucose with different concentrations. The inset shows the image of the interference fringes in case of DI water. **b** Interference fringes' shifts with changing glucose concentrations on the left-hand side axis (blue colored), and the theoretical refractive index values on the right-hand side axis (red colored)

interference patterns are recorded by a CCD camera with pixel pitch of 2.2 μm. The obtained images are analyzed by image processing to extract the interference patterns. Figure 2a shows the normalized intensity of the fringe patterns for DI water and glucose aqueous solutions with concentrations of 0.1 and 0.15%. The evident spatial shift between them corresponds to the change in RI of each solution.

From the analysis of the patterns in Fig. 2a, the interference fringes' shifts with changing glucose concentrations have been determined from all the peaks. The mean and standard deviation (σ_e) of the data are plotted on the left-hand side axis of Fig. 2b. The mean values are represented by the blue circles, and the error bars represent $\pm\sigma_e$. Theoretical RI values for the glucose solution of concentration 0.5% are obtained from the literature [5]. The relation between RI and glucose concentration is assumed to be linear within the low concentration range and is plotted on the right-hand side axis in Fig. 2b represented by the red line. The linear plot is used to estimate the sensitivity of the device that is found to be 3.65×10^{-5} *RIE/pixel*. This value depends on the pixel size of the CCD camera in use, and can be enhanced by using smaller pixel size. To avoid this dependence, the shift per length can be employed which will be 1.66×10^{-5} *RIE/*μm. The resolution of a sensor is estimated by three times the root-mean-square (rms) value of the noise variations, that is the standard deviation σ_e. From the error bars in Fig. 2b, the maximum standard deviation is 0.79 *pixel*, and then the resolution $3\sigma_e = 2.37$ *pixel*. The detection limit of a refractometer is the smallest change in RI that can be accurately detected, that is sensitivity multiplied by resolution, which gives 8.7×10^{-5} *RIE*.

References

1. Fan X, White IM (2011) Optofluidic microsystems for chemical and biological analysis. Nat Photonics 5:591–597

2. Liu Q, Huang HJ, Chin LK, Yu YF, Li XC (2008) Label-free detection with micro optical fluidic systems (MOFS): a review. Anal Bioanal Chem 39:2443–2452
3. Schmitt K, Schirmer B, Hoffmann C, Brandenburg A, Meyrueis P (2007) Interferometric biosensor based on planar optical waveguide sensor chips for label-free detection of surface bound bioreactions. Biosens Bioelectron 22:2591–2597
4. Brandenburg A (1997) Differential refractometry by an integrated-optical Young interferometer. Sens Actuators B 38:266–271
5. Lide DR (2004) CRC handbook of physics and chemistry. 84th edn. CRC Press

Nonlinear Radiation Force on Nanoparticles

H. L. Chen, Y. Y. Huang, and L. Gao

Abstract We calculate the radiation force on the nonlinear nanoparticle based on nonlinear Mie theory and Maxwell's stress tensor method. The bistable radiation force can be observed and can be tuned through varying the nanoparticle's size, the incident wavelength and the permittivity of the surrounding medium to obtain larger bistable region. Our results introduce nonlinear material to study the radiation force, which will have potential applications in optical manipulations and optical transportation.

Keywords Mie theory · Optical bistability · Optical manipulation

1 Introduction

Optical micromanipulation based on radiation force has attracted much attention in the past decades due to its wide applications in physics, chemistry and biology [1–5]. In the last century, Ashkin et al. have demonstrated the trapping of micron-size particles experimentally by radiation pressure of light [6]. It is interesting that light beam can not only push the object forward, but also pull the particle toward the source via a backward scattering force, called optical pulling force [7–9]. Meanwhile, the nonlinear materials have also attracted much interest [10, 11]. Nonlinear optical effects, such as optical bistability [12–14], have an important role in optical switching, optical transistor and optical modulation. In this paper, we study the radiation force on the nanoparticle and demonstrate that the radiation force exhibits bistability.

We adopt Maxwell's stress tensor method to calculate the radiation force on the nonlinear nanoparticle. Considering the nanoparticle is nonlinear, we obtain the fields of the nanoparticle based on Mie theory and the self-consistent mean-field

H. L. Chen (✉) · Y. Y. Huang
School of Science, Nantong University, Nantong 226000, China
e-mail: chenhongli90@126.com

L. Gao
School of Physical Science and Technology, Soochow University, Suzhou 215006, China

L. Xu and L. Zhou (eds.), *Proceedings of the 8th International Multidisciplinary Conference on Optofluidics (IMCO 2018)*, Lecture Notes in Electrical Engineering 531,
https://doi.org/10.1007/978-981-13-3381-1_11

approximation method. The strong optical bistability of the radiation force for the nonlinear nanoparticles is demonstrated. The bistable region can be tuned by altering the nanoparticle's size, the surrounding environment's permittivity and the incident wavelength.

2 Theoretical Development

We firstly consider the linear nanoparticle with radius a, the relative permittivity ε_c and permeability μ_c, embedded in the medium of the relative permittivity ε_m and permeability μ_m. Based on the Lorenz–Mie scattering theory, the incident field, the scattered field and the field in the nanoparticle can be expressed as series expansions for transverse-magnetic (TM) and transverse-electric (TE) spherical modes [15, 16].

To study the nonlinear effects on optical materials, we consider the Kerr material with weak nonlinearity $\widetilde{\varepsilon_c} = \varepsilon_L + \chi^{(3)}|E_c|^2$. And we adopt the mean-field approximation method and replace the nonlinear local field with the mean field, that is,

$$\widetilde{\varepsilon_c} = \varepsilon_L + \chi^{(3)}|E_c|^2 \approx \varepsilon_L + \chi^{(3)}\left\langle |E|^2 \right\rangle_c. \tag{1}$$

Substituting Eq. (1) into Lorenz-Mie scattering theory, we can deduce the nonlinear Lorenz-Mie scattering theory.

After solving the electric fields based on the above theory, we integrate the Maxwell's stress tensor over the surface of the nanoparticle to calculate the radiation force on it. The field components are related with Maxwell's stress tensor by the following expression

$$T_{ij} = \varepsilon_0\varepsilon_m E_i E_j + \mu_0\mu_m H_i H_j - \frac{1}{2}\delta_{ij}(\varepsilon_0\varepsilon_m|E|^2 + \varepsilon_0\varepsilon_m|H|^2).$$

Then, the total time-averaged radiation force acting on the nanoparticle can be written as

$$\langle F \rangle = \frac{1}{2}\mathrm{Re}\left(\int_S T_{ij} \cdot n_j dS\right), \tag{3}$$

where n_j is the outward normal vector of the surface of the nanoparticle. The normalized force is expressed as $F_0 = \pi a^2 S_{\mathrm{inc}}/c$, where S_{inc} is the power flow density of the incident wave.

3 Numerical Calculations

We now consider the nanoparticle with nonlinear relative permittivity [17], $\widetilde{\varepsilon_c} = \varepsilon_L + \chi^{(3)}|E_c|^2$, where $\varepsilon_L = 2.2$ and $\chi^{(3)} = 4.4 \times 10^{-20}\mathrm{m}^2/\mathrm{V}^2$. We assume both the background and the nonlinear nanoparticle are non-magnetic with $\mu_m = \mu_c = 1$.

Firstly, we study the radiation force when the nanoparticle is illuminated by a plane wave with different wavelengths. In Fig. 1, it shows that the radiation force on the nonlinear nanoparticle exhibits bistable behavior. The radiation force first increases with the incident field E_0 and then discontinuously jumps up to the upper branch upon reaching the switching-up threshold field $E_{0-\mathrm{up}}$($E_{0-\mathrm{up}} \approx 1.45 \times 10^{10}\mathrm{V/m}$ for $\lambda =$ 510 nm). On the other hand, when the incident field E_0 is decreased to the switching-down threshold field $E_{0-\mathrm{down}} \approx 9.5 \times 10^9\mathrm{V/m}$ for $\lambda = 510$ nm), it discontinuously jumps down to the lower branch. Interestingly, we find that there is a maximum positive radiation force at the switching-down threshold field. And the bistable behavior becomes broader with increasing the wavelength.

Next, we plot the radiation force as a function of the permittivity of the surrounding medium to study the effect of the environment on the force. Figure 2 shows that increasing the permittivity, the bistable region becomes narrower. As shown in Fig. 2a, the maximum positive radiation force at the switching-down threshold field decreases with increasing the permittivity of the surrounding medium. However, for the permittivity larger than about 3, Fig. 2b shows a smoother line shape of the radiation force compared to Fig. 2a, and the radiation force at the switching-down threshold field is not the maximum positive value. In this case, one point worth emphasizing is that the radiation force firstly decreases and then increases at low incident electric field.

Then, we study the influence of the size of the nanoparticle on the bistable behavior. Figure 3a shows that increasing the size of the nanoparticle results in the bistable region of the radiation force becoming narrower due to the decrease of the switching-up threshold field. Meanwhile, the bistable region of the radiation

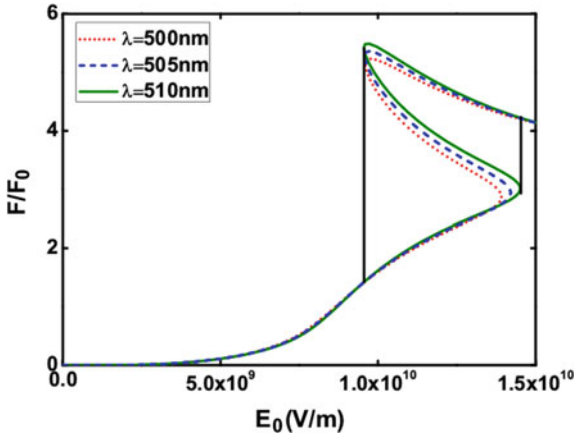

Fig. 1 Normalized radiation force as a function of the incident field E_0. The size of the nanoparticle is $a =$ 100 nm, and the permittivity of the surrounding medium is $\varepsilon_m = 2.25$

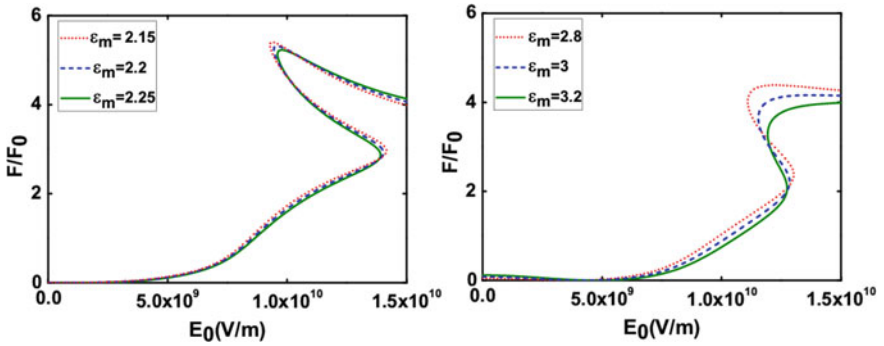

Fig. 2 Normalized radiation force as a function of the incident field E_0. The size of the nanoparticle is $a = 100$ nm, and the incident wavelength is $\lambda = 500$ nm

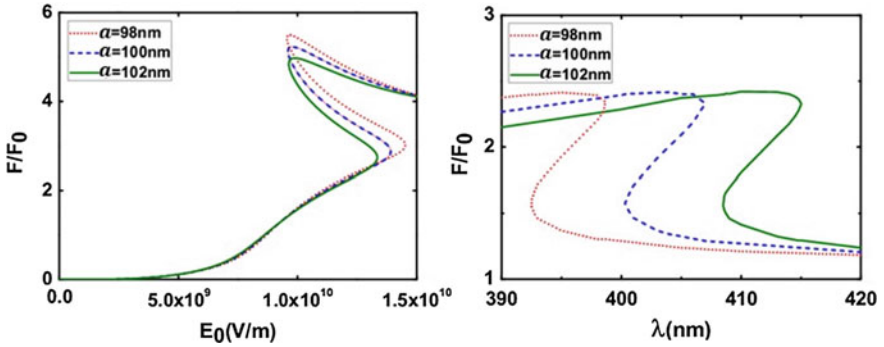

Fig. 3 Normal radiation force on the nanoparticle with different sizes. **a** Normalized radiation force as a function of the incident field E_0 with $\lambda = 500$ nm. **b** Normalized radiation force as a function of wavelength with the incident electric field $E_0 = 9 \times 10^9$ V/m. The permittivity of the surrounding medium is $\varepsilon_m = 2.25$

force shifts downwards when the size of the particle increases. In Fig. 3b, we plot the radiation force versus the incident wavelength for a fixed input electric field $E_0 = 9 \times 10^9$ V/m. It shows that the bistable behavior is observable as well with varying the incident wavelength. The bistable behavior is similar to the case where the incident electric field is varied. However, the bistable region red shifts with increasing the size of the nanoparticle. This result provides the possibility of tuning the switching wavelength and switching threshold field of the radiation force via changing the size of the nanoparticles for potential applications.

4 Conclusions

In conclusion, we calculate the radiation force on nonlinear nanoparticles and demonstrate optical bistability of the radiation force based on nonlinear Mie theory and Maxwell's stress tensor method. When the optical intensity is sufficiently high, the nonlinearity of nanoparticles can give rise to bistable responses of radiation force. The bistable radiation force can be tuned by the nanoparticle's size, the incident wavelength and the permittivity of the surrounding medium.

Funding This work was supported by the National Science of Jiangsu Province (Grant No. BK20161210); the Qing Lan project, "333" project (Grant No. BRA2015353); Natural Science Foundation for the Youth of Jiangsu Province (No. BK20150306); Natural Science Foundation for Colleges and Universities in Jiangsu Province of China (No.15KJB140008).

Conflicts of Interest The authors declare no conflicts of interest.

References

1. Antognozzi M, Bermingham CR, Harniman RL, Simpson S, Senior J, Hayward R et al (2016) Direct measurements of the extraordinary optical momentum and transverse spin- dependent force using a nano-cantilever. Nat Phys 12:731–735
2. Cheuk LW, Anderegg L, Augenbraun BL, Bao YC, Burchesky S, Ketterle W et al (2018) Lambda-enhanced imaging of molecules in an optical trap. Phys Rev Lett 121:083201
3. Reimann R, Doderer M, Hebestreit E, Diehl R, Frimmer M, Windey D et al (2018) GHz rotation of an optically trapped nanoparticle in vacuum. Phys Rev Lett 121:033602
4. Senaratne R, Rajagopal SV, Shimasaki T, Dotti PE, Fujiwara KM, Singh K et al (2018) Quantum simulation of ultrafast dynamics using trapped ultracold atoms. Nat Commun 9:2065
5. Wang HM, Wang L, Jakob DS, Xu XJG (2005) Tomographic and multimodal scattering-type scanning near-field optical microscopy with peak force tapping mode. Nat Commun 2018:9
6. Ashkin A (1970) Acceleration and trapping of particles by radiation pressure. Phys Rev Lett 24:156–159
7. Chen J, Ng J, Lin Z, Chan CT (2011) Optical pulling force. Nat Photon 5:531–534
8. Alaee R, Christensen J, Kadic M (2018) Optical pulling and pushing forces in bilayer PT-symmetric structures. Phys Rev Appl 9:014007
9. Zhu T, Cao Y, Wang L, Nie Z, Cao T, Sun F et al (2018) Self-induced backaction optical pulling force. Phys Rev Lett 120:123901
10. Nielsen MP, Shi XY, Dichtl P, Maier SA, Oulton RF (2017) Giant nonlinear response at a plasmonic nanofocus drives efficient four-wave mixing. Science 358:1179–1181
11. von Hoegen A, Mankowsky R, Fechner M, Forst M, Cavalleri A (2018) Probing the interatomic potential of solids with strong-field nonlinear phononics. Nature 555:79
12. Fink T, Schade A, Hofling S, Schneider C, Imamoglu A (2018) Signatures of a dissipative phase transition in photon correlation measurements. Nat Phys 14:365
13. Navarro-Urrios D, Capuj NE, Colombano MF, Garcia PD, Sledzinska M, Alzina F et al (2017) Nonlinear dynamics and chaos in an optomechanical beam. Nat Commun 8:14965
14. Pickup L, Kalinin K, Askitopoulos A, Hatzopoulos Z, Savvidis PG, Berloff NG et al (2018) Optical bistability under nonresonant excitation in spinor polariton condensates. Phys Rev Lett 120:225301

15. Born M, Wolf E (1999) Principles of optics: Electromagnetic theory of propagation, interference and diffraction of light. Cambridge University Press
16. Bohren CF, Huffman DR (1983) Absorption and scattering of light by small particles. Wiley, New York
17. Argyropoulos C, Chen PY, Monticone F, D'Aguanno G, Alu A (2012) Nonlinear plasmonic cloaks to realize giant all-optical scattering switching. Phys Rev Lett 108:263905

Polymer Microtip Bridge Between Two Optical Fibers Integrated in a V-Groove

Jingyu Tan, Caoyuan Wang, and Limin Xiao

Abstract The optical fiber microtips can be utilized as a unique platform for various applications, including optical coupling, sensing, beam shaping and optomechanical systems. Here, we fabricate a polymer microtip between two SMFs and the whole device is integrated in a V-groove which is portable and reusable. Characteristics of the microtip bridge will be discussed. This integrated portable device can be used in various coupling and sensing applications.

Bachelot et al. [1] introduced a method to fabricate fiber-based polymer microtips. The optical fiber microtips can be utilized as a unique platform for various applications, including optical coupling [2], sensing [3], beam shaping and opto-mechanical systems.

Different approaches to fabricate polymer microtips between two fibers were demonstrated using photopolymerization [4]. A polymer bridge was constructed between the fiber ends through injecting actinic light from two counter-propagating optical fibers, which realized low loss coupling [5]. Polymer waveguides with different lengths were fabricated between two single mode fibers (SMFs) using single photon polymerization via a xenon lamp instead of a monochromatic laser source [6]. However, these methods all require a sophisticated 3D alignment system that is bulky and may not be convenient to use.

J. Tan · C. Wang · L. Xiao (✉)
Advanced Fiber Devices and Systems Group, Key Laboratory of Micro and Nano Photonic Structures (MoE), Department of Optical Science and Engineering, Fudan University, Shanghai, China
e-mail: liminxiao@fudan.edu.cn

L. Xiao
Key Laboratory for Information Science of Electromagnetic Waves (MoE), Fudan University, Shanghai, China

Shanghai Engineering Research Center of Ultra-Precision Optical Manufacturing, Fudan University, Shanghai, China

L. Xu and L. Zhou (eds.), *Proceedings of the 8th International Multidisciplinary Conference on Optofluidics (IMCO 2018)*, Lecture Notes in Electrical Engineering 531,
https://doi.org/10.1007/978-981-13-3381-1_12

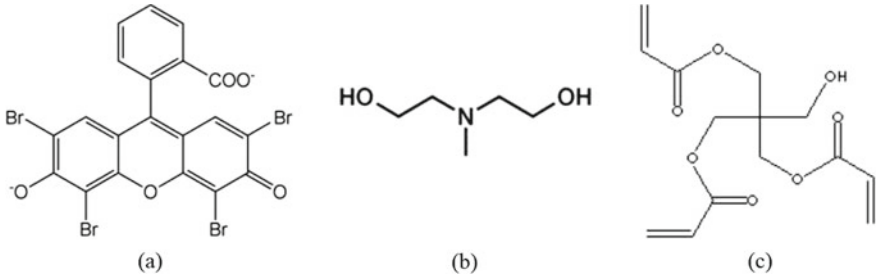

Fig. 1 Molecular structure diagrams of **a** eosin Y, **b** MDEA, **c** PETIA [1]

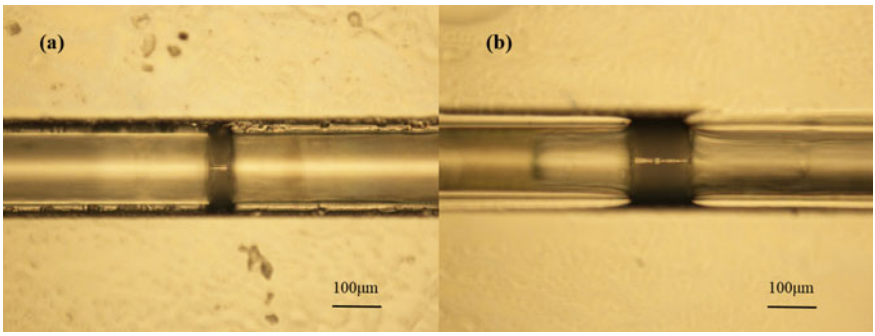

Fig. 2 Microscope images of two microtip bridges with different lengths between SMFs **a** 38 μm, **b** 108 μm

Here, we fabricate a polymer microtip between two SMFs, and the whole device is integrated in a V-groove which is portable and reusable. To fabricate a microtip, we should prepare photopolymer reagent first. The photopolymerizable reagent is made up of three basic components: a sensitizer dye, an amine cosynergist and a multifunctional acrylate monomer. In this experiment, we use 0.5% in weight of eosin Y, 8% in weight of methyldiethanolamine (MDEA) and 91.5% in weight of pentaerythritol triacrylate (PETIA), as shown in Fig. 1 [1].

After two SMFs were placed and fixed in a V-groove at a certain distance from each other, a drop of liquid reagent was deposited in the gap between SMFs. Then, the green laser was coupled in the SMF on the left hand, and laser light emerging from the core of the SMF solidifies external photosensitive material. A polymer microtip bridge therefore grew between cores of two SMFs within the unreacted liquid, and the unreacted liquid was then washed off by a few drops of ethanol.

We can control the microtip length conveniently by placing two SMFs at a set distance. Besides, through adjusting green laser power and laser exposure time, we can get microtips with different diameters. Figure 2 depicts microscope images of two microtip bridges between SMFs with different lengths. The laser power was 3 μw, and the exposure time was 120 s. The microtip bridge ensures light propagation over

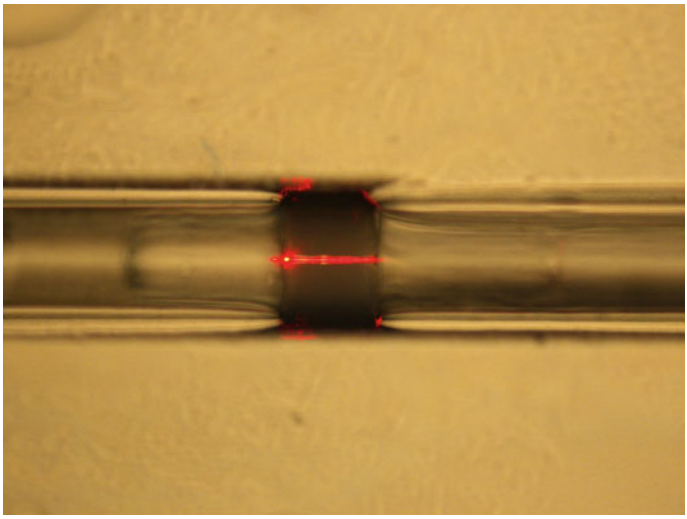

Fig. 3 Microscope image of a photopolymer microtip bridge carrying some red light

a broad bandwidth ranging from 406 to 1550 nm. Figure 3 shows the photopolymer microtip bridge in Fig. 2b carrying some red light.

When the laser power was 3 μw and the exposure time was 90 s, the tip base was about 13 μm with the length of 82 μm. At a wavelength of 532 nm, this microtip achieves the lowest loss transmission with 0.25 dB loss.

We have fabricated polymer microtips between two SMFs, and the whole device is integrated in a V-groove which is portable and reusable. This integrated device can be used in various coupling and sensing applications.

Funding National Natural Science Foundation of China (NSFC) (61475119, 61775041); Shanghai Pujiang Program (17PJ1400600); National Key R&D Program of China (2016YFC0201401).

References

1. Bachelot R, Ecoffet C, Deloeil D, Royer P, Lougnot DJ (2001) Integration of micrometer-sized polymer elements at the end of optical fibers by free-radical photopolymerization. Appl Opt 40:5860–5871
2. Xiao L, Jin W, Demokan MS, Ho HL, Tam H, Ju J, Yu J (2006) Photopolymer microtips for efficient light coupling between single-mode fibers and photonic crystal fibers. Opt Lett 31:1791–1793
3. Pura P, Szymański M, Dudek M, Jaroszewicz L, Marć P, Kujawińska M (2015) Polymer microtips at different types of optical fibers as functional elements for sensing applications. J Lightwave Technol 33:2398–2404

4. Klein S, Barsella A, Leblond H, Bulou H, Fort A, Andraud C, Lemercier G, Mulatier JC, Dorkenoo KD (2005) One-step waveguide and optical circuit writing in photopolymerizable materials processed by two-photon absorption. Appl Phys Lett 86:211118–211121
5. Jradi Safi, Soppera Olivier, Lougnot Daniel J (2008) Fabrication of polymer waveguides between two optical fibers using spatially controlled light-induced polymerization. Appl Opt 47:3987–3993
6. Mohammed PA, Wadsworth WJ (2015) Long free-standing polymer waveguides fabricated between single-mode optical fiber cores. J Lightwave Technol 33:4384–4389

Refractive Index Sensor Based on Long-Range Surface Plasmon Polariton Waveguide

Xiaoqiang Sun, Yan Xu, Pierre Berini, and Daming Zhang

Abstract Straight long-range surface plasmon polariton (LRSPP) waveguides are demonstrated as liquid refractive index (RI) sensors (Barnes et al. in Nat Mater 424:824–830, 2003, [1]). The sensors consist of 5 μm-wide, 20 nm-thick straight Au stripes that are embedded in ultraviolet (UV) sensitive polymer SU-8. The double layer liftoff fabrication is adopted to fabricate the embedded rectangular and smooth Au stripes. An etched microfluidic channel allows the contact of analyte to Au surface for RI detection. Within the range from 1.576 to 1.596, a sensitivity of 821 dB/RIU can be obtained. The proposed device has potentials in the portable and compact refractometer application.

Keywords LRSPP · Waveguide · RI sensor · Polymer · Lift-off

1 Introduction

Surface plasmon resonance (SPPs) is propagating modes existed at the interface between a metal and dielectric medium. Due to the characteristic of strong mode confinement, SPPs are very sensitive to the RI (RI) change near metal surface [1]. However, the high light absorption in metal leads to a high propagation loss. Therefore, long-range surface plasmon polaritons (LRSPPs) that are propagating plasmon waves excited on both sides of symmetrically embedded metal stripes are investigated [2]. To enhance the firmness and simplify the fabrication of LRSPP waveguide, we

X. Sun · Y. Xu · D. Zhang (✉)
State Key Laboratory of Integrated Optoelectronics, College of Electronic Science and Engineering, Jilin University, Changchun, China
e-mail: zhangdm@jlu.edu.cn

P. Berini
School of Electrical Engineering and Computer Science, University of Ottawa, Ottawa, Canada
e-mail: pberini@uottawa.ca

Centre for Research in Photonics, University of Ottawa, Ottawa, Canada

Department of Physics, University of Ottawa, Ottawa, Canada

L. Xu and L. Zhou (eds.), *Proceedings of the 8th International Multidisciplinary Conference on Optofluidics (IMCO 2018)*, Lecture Notes in Electrical Engineering 531,
https://doi.org/10.1007/978-981-13-3381-1_13

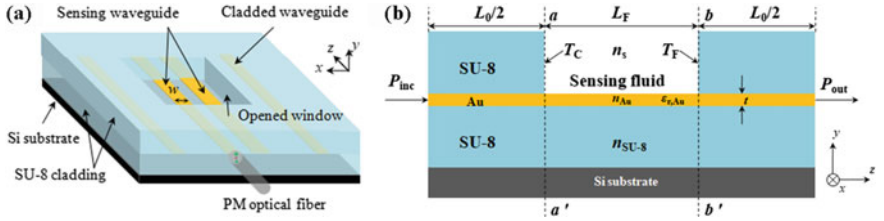

Fig. 1 Configuration of **a** three-dimentional illustration of the straight LRSPP waveguide RI sensor. A polarization-maintaining (PM) optical fiber is butt-coupled to the input of the waveguide to excite the LRSPP mode thereon, **b** longitudinal cross section of the straight LRSPP waveguide sensor

choose the ultraviolet (UV) polymer of SU-8 as the cladding material, which has good adhesion on silicon substrate without using hexamethyldisilazane (HMDS) excess layer. Its high glass temperature and resistance to the erosion of most solvents, such as acetone and isopropyl alcohol (IPA), promise good structural stability [3]. The smooth SU-8 film surface is also favorable to high quality metal layer deposition.

2 Device Design

The proposed straight LRSPP waveguide RI sensor is shown in Fig. 1. Straight Au stripe with the width $w = 5$ μm and thickness $t = 20$ nm is embedded in SU-8 claddings. The whole structure is supported by a silicon substrate. The thicknesses of upper and bottom claddings are both 5 μm. The microfluidic channel with length L_F is formed on the top of Au stripe by wet chemical etching. As measuring, the analyte with a RI of n_s that is around n_{su-8} fills the channel. The RI change above the straight Au waveguide will result in the variation of output optical power.

3 Experimental

The double layer liftoff fabrication flow is depicted in Fig. 2. Firstly, the 4 inches silicon wafer was cleaned. SU-8 2005 (MicroChem Corp., US) was spin-coated onto the silicon substrate as the bottom cladding. Then, SU-8 was prebaked at 65 and 95 °C for 5 and 10 min, respectively. After flush exposure at a UV dose of 100 mW, post-exposure bake was done at 65 and 95 °C for 10 and 20 min, respectively. Photoresist LOR-1A (MicroChem Corp., US) and MICROPOSIT S1805 (Shipley Corp.,) were directly spin-coated on the SU-8 bottom cladding and cured at 180 °C for 3 min, respectively. Waveguide patterns were transferred from the photomask to S1805 by UV photolithography. After development in MICROPOSIT MF-321 (Shipley Corp.,), a 20 nm-thick Au film was deposited by electron beam evaporation (Angstrom Co., CA). Thereafter, the liftoff process was done with two baths

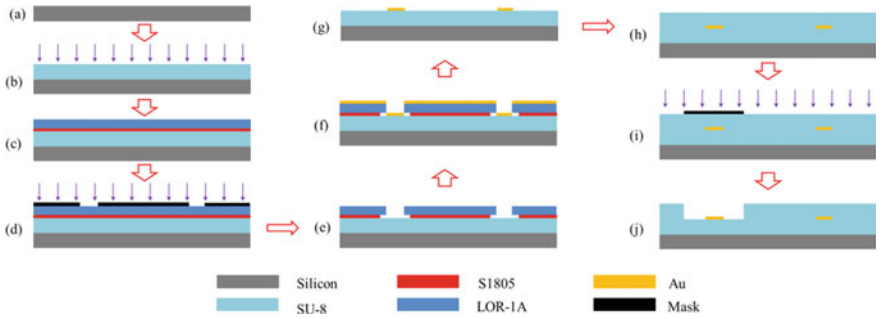

Fig. 2 **a** Preparation for silicon wafer, **b** spin-coating and prebake of SU-8 bottom cladding, **c** UV cure of SU-8 bottom cladding, **d** spin-coating and baking of bi-layer photoresist LOR/S1805 stack, **e** UV exposure and development, **f** Au film deposition by E-beam evaporation, **g** liftoff of LOR-1A and S1805, **h** spin-coating and solidification of SU-8 upper cladding, **i** UV photolithography and fluidic channel etch, **j** spin-coating of SPR 220 resist

of Remover PG (MicroChem Corp., USA) at room temperature. Finally, the SU-8 microfluidic channel was formed by UV photolithography and wet chemical etching.

The fabricated Au stripe was characterized by atomic force microscope (AFM) NX10 (Park Corp., ROK), as shown in Fig. 3. It can be seen that root mean square roughness of Au stripe is 1.470 nm and the roughness of SU-8 is 0.772 nm. The remains left on Au stripe surface can be removed by further oxygen plasma cleaning.

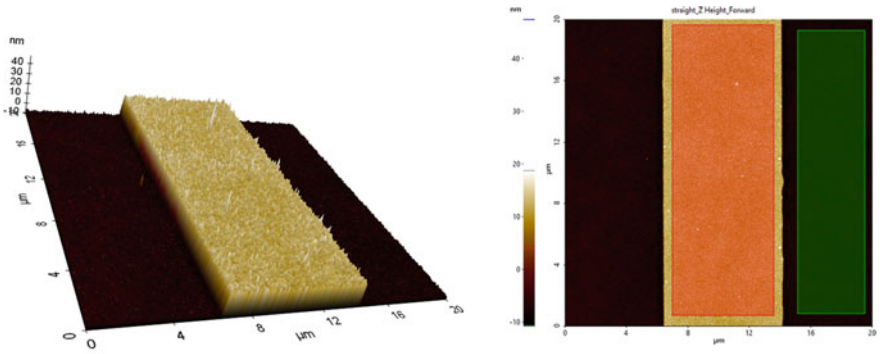

Statistics

Region	Min(nm)	Max(nm)	Mid(nm)	Mean(nm)	Rpv(nm)	Rq(nm)	Ra(nm)	Rz(nm)	Rsk	Rku
Red	8.354	47.447	27.900	11.703	39.092	1.470	1.112	34.712	-2.384	33.582
Green	**-10.430**	**-3.402**	**-6.916**	**-7.844**	**7.028**	**0.772**	**0.614**	**6.594**	**-0.344**	**3.242**
R-G	18.785	50.849	34.817	19.547	32.064	0.698	0.498	28.118	-2.040	30.340

Fig. 3 AFM image of fabricated Au stripe on SU-8 surface

4 Results

The RI sensing performance was characterized by the setup shown in Fig. 4. RI matching liquids (Series A, Cargille) with an increment of 2×10^{-3} RIU were sequentially injected into the fluidic channel. The optical power change captured as a function of RI of liquid is illustrated in Fig. 5.

The output optical mode from straight LRSPP waveguide is bright and clear with seldom surrounding radiation within the RI range from 1.576 to 1.596. Moreover, the brightness of output mode pattern grows steadily with the increment of RI of liquid, which corresponds to the linear decrement of insertion loss. As shown in Fig. 5, the largest output signal corresponds to the analyte with a RI of 1.596. This value is supposed to be very close to $n_{\text{su-8}}$ (cured SU-8). The most significant signal variation of $\Delta S = 34.087$ μW is obtained when the RI shifts from 1.576 to 1.596, which corresponds to a sensitivity of 821 dB/RIU. For our setup, the standard deviation of

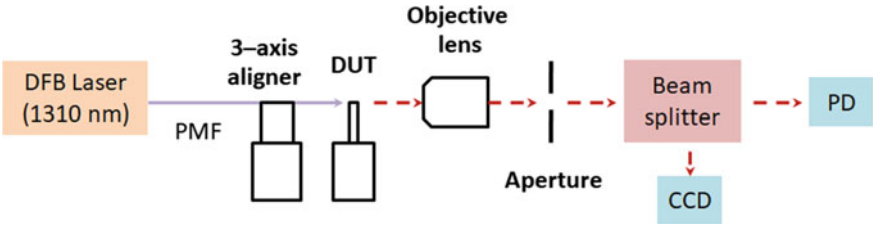

Fig. 4 Measurement setup for straight LRSPP waveguide RI sensor at $\lambda = 1310$ nm

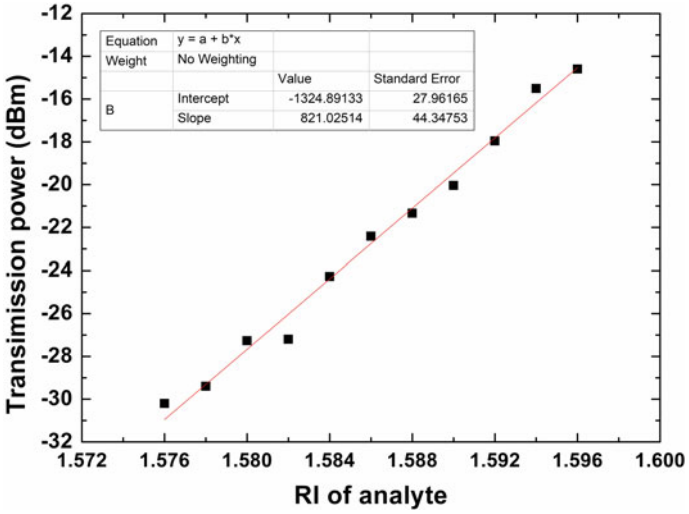

Fig. 5 Transmission power of 5 μm-wide straight LRSPP waveguide versus RI in fluidic channel ($\lambda = 1310$ nm)

output power can be lowered to $\delta = 5$ nW with our measurement setup [4]. For signal-to-noise ratio $\Delta S/\delta = 1$, the detection limit is 2.934×10^{-6} RIU at the wavelength 1310 nm within the detection range.

Acknowledgements This work is also supported by the National Natural Science Foundation of China (Nos. 61675087, 61575076).

References

1. Barnes WL, Dereux A, Ebbesen TW (2003) Surface plasmon subwavelength optics. Nat Mater 424, 824–830
2. Charbonneau R, Berini P, Berolo E, Lisicka-Shrzek E (2000) Experimental observation of plasmon-polariton waves supported by a thin metal film of finite width. Opt Lett 25:844–846
3. Ji L, Sun X et al (2017) Surface plasmon resonance refractive index sensor based on ultraviolet bleached polymer waveguide. Sens Actuat B-Chem 244:373–379
4. Krupin O, Asiri H, Wang C, Tait RN, Berini P (2013) Biosensing using straight long-range surface plasmon waveguides. Opt Express 21:698–708

Second-Order Differentiator Based on Long-Period Waveguide Grating

Ailing Zhang, Hongyun Song, and Bo Geng

Abstract In this paper, a structure of second-order differentiator based on long-period waveguide grating (LPWG) is proposed. The second-order differentiator consists of two segment uniform gratings, one segment waveguide and electrode correspondingly deposited on both sides of waveguide on *x*-cut lithium niobate (LN) crystal. The performances of the second-order differentiator are analyzed and simulated. It shows that it can be implemented by introducing π-phase shift by adjusting voltage according to the electro-optic effect of LN.

Keywords Long-period waveguide grating (LPWG) · Differentiator · Lithium niobate (LN) · Electro-optic effect

1 Introduction

An *N*-th photonic differentiator can realize the *N*-th time derivative of input optical signal and has important applications in analog–digital conversion, pulse shaping, and optical processing of microwave signals [1]. In recent years, second-order differentiators based on long-period fiber grating (LPFG) have been proposed and experimentally verified [2, 3]. It normally uses the elastic-optical effect in fiber to obtain the differentiated function, resulting in low tuning speed. Lithium niobate (LN) has advantages of good electro-optic effect and fast tuning speed. Therefore, second-order differentiator based on LN long-period waveguide grating (LPWG) has potential applications in high-speed differentiator.

In this paper, a structure of second-order differentiator based on LPWG is proposed. And the second-order differentiator is analyzed theoretically and simulated by MATLAB. The fabrication of LPWG based on LN is investigated.

A. Zhang (✉) · H. Song · B. Geng
School of Electrical and Electronic Engineering, Engineering Research Center of Ministry of Education for Optoelectronic Devices and Communication Technology, Tianjin Key Laboratory of Film Electronic and Communication Devices, Tianjin University of Technology, Tianjin, China
e-mail: alzhang07@163.com

L. Xu and L. Zhou (eds.), *Proceedings of the 8th International Multidisciplinary Conference on Optofluidics (IMCO 2018)*, Lecture Notes in Electrical Engineering 531,
https://doi.org/10.1007/978-981-13-3381-1_14

2 Principle

The structure of second-order differentiator based on LPWG is shown in Fig. 1. It consists of two segments of uniform LPWG gratings, one segment of waveguide and electrodes correspondingly deposited on both sides of waveguide on x-cut LN crystal.

According to transfer-matrix method, the matrix of differentiator can be expressed as [6].

$$F = F2 \times P \times F1 \tag{1}$$

where F_1 is the transfer matrix of the 1-th grating and F_2 is the transfer matrix of the 2-th grating. P is transfer matrix of the waveguide.

F_1 is expressed as

$$F_i = \begin{bmatrix} \cos(sl_i) + j\frac{\delta}{s}\sin(sl_i) & j\frac{\kappa}{s}\sin(sl_i) \\ j\frac{\kappa}{s}\sin(sl_i) & \cos(sl_i) - j\frac{\delta}{s}\sin(sl_i) \end{bmatrix} \quad i = 1, 2 \tag{2}$$

where l_i is length of the ith grating ($i = 1, 2$), $\delta = \frac{\pi(N_{\text{co}} - N_{\text{cl}})}{\lambda} - \pi/\Lambda$ and $\kappa = \frac{\pi}{\lambda}\Delta N$ are the detuning and coupling coefficient of the grating, respectively. N_{co} and N_{cl} are effective refractive index of the core and cladding of waveguide, ΔN is modulation amplitude of the grating, Λ is the period of the grating and $s = \sqrt{\kappa^2 + \delta^2}$.

P is expressed as

$$\mathrm{P} = \begin{bmatrix} \mathrm{e}^{-j\frac{\theta}{2}} & 0 \\ 0 & \mathrm{e}^{j\frac{\theta}{2}} \end{bmatrix} \tag{3}$$

According to electro-optic effect of LN [7], θ is

$$\theta = \frac{2 \cdot \pi \cdot L}{\lambda} \cdot \left(N_{\text{co}} - \frac{V}{2d}\gamma_{33}N_{\text{co}}^3 \right) \tag{4}$$

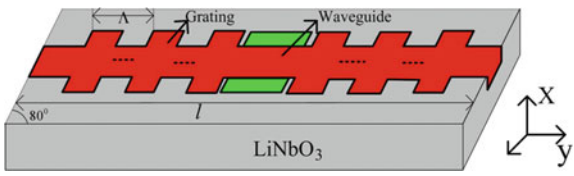

Fig. 1 Structure of second-order differentiator based on long-period waveguide grating

where L is the length of waveguide, V is the voltage added on electrode with gap d. $\gamma_{33} = 30.8\,\text{pm/V}$ is used for the electric field is parallel to the optical axis z.

Suppose a voltage is applied across the waveguide to produce π phase shift, the transfer function of the differentiator is

$$F[1,1] = -j\frac{\delta^2}{s^2}\cos s(l_1 + l_2) - j\frac{\kappa^2}{s^2}\cos s(l_1 - l_2) + \frac{\delta}{s}\sin s(l_1 + l_2) \tag{5}$$

Expanding $F(1,1)$ into Taylor series analytically around the central frequency ω_0.

$$F[1,1] = F(\omega_0) + \frac{1}{2}F'(\omega_0)(\omega - \omega_0) + \frac{1}{6}F''(\omega_0)(\omega - \omega_0)^2 + \ldots \tag{6}$$

For the second-order differentiator, it is required that the constant term and the first-order term are zero. According to Eqs. (5) and (6), we can obtain

$$\kappa l_1 = \frac{3\pi}{4} \quad \kappa l_2 = \frac{\pi}{4} \tag{7}$$

As a result, in order to obtain a second-order differentiator, θ should be equal to π, and length ratio of two segments LPWG should be $l_1{:}l_2 = 3{:}1$. According to Eq. (4), π phase shift can be achieved by adjusting the voltage V.

3 Results

The second-order differentiator is verified by MATLAB in the following. In simulation, we set $N_{co} = 2.139$, $N_{cl} = 2.137$, $\Delta N = 0.5 \times 10^{-4}$, $\Lambda = 775\,\mu\text{m}$, $L = 3.6\,\text{mm}$, $d = 7\,\mu\text{m}$, and set $l_1 = 20.4\,\text{mm}$, $l_2 = 6.8\,\text{mm}$ according to theoretical analysis.

Figure 2 shows the relationship between the phase shift and voltage. It can be seen that the tuning efficiency of the phase is 0.1 π/V, which will be increased by using a longer length of waveguide. From Fig. 2, π-phase shift can be obtained by applying 10 V voltage.

According to theoretical analysis, the second-order differentiator can be implemented by π-phase shift inserted between two LPWG with $l_1{:}l_2 = 3{:}1$, and the spectra of two LPWG are shown in Fig. 3.

The spectrum of the second-order differentiator is shown in Fig. 4. As can be seen from Fig. 4, the transmission spectrum of it is approximately a quadratic function near the resonance frequency.

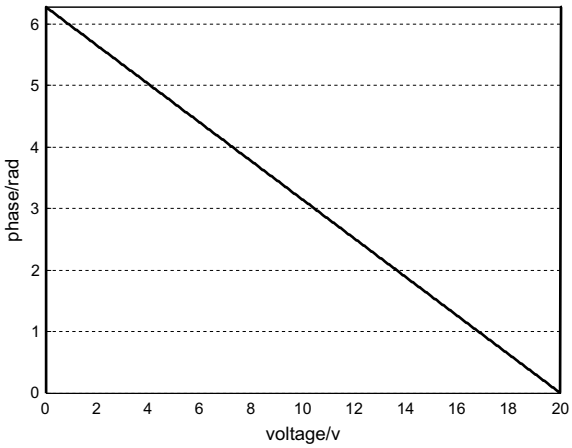

Fig. 2 Phase shift versus voltage V

Gaussian pulse was spectrally centered at the LPWGs' resonance frequency and subsequently propagated through the LPWG structure. The output waveform is shown in Fig. 5. From Fig. 5b, there is a fairly good agreement between the theoretically predicted and output time-domain waveform. Thus, it verifies feasibility of second-order differentiator based on LPWG.

Figure 6 shows the relationship between amplitude of second-order differentiator and ΔN. As can be seen, amplitude of second-order differentiator is inversely proportional to ΔN.

4 Conclusion

In this paper, a structure of second-order differentiator based on long-period waveguide grating (LPWG) is proposed. The second-order differentiator is verified theoretically by MATLAB. The second-order time derivative of Gaussian pulses is obtained by introducing a π phase shift by adjusting voltage at 3/4 of the length of the grating.

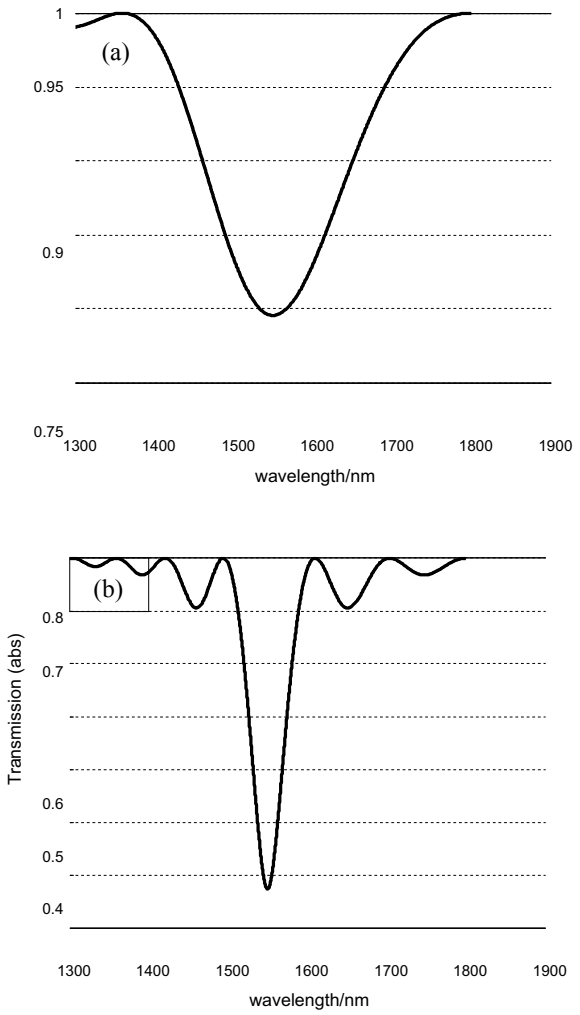

Fig. 3 Transmission spectra of two-segment grating **a** spectrum of the 1th grating, **b** spectrum of the 2th grating

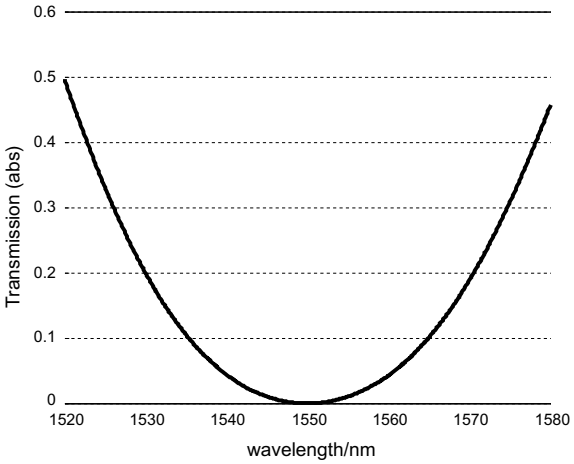

Fig. 4 Transmission function of second-order differentiator based on LPWG

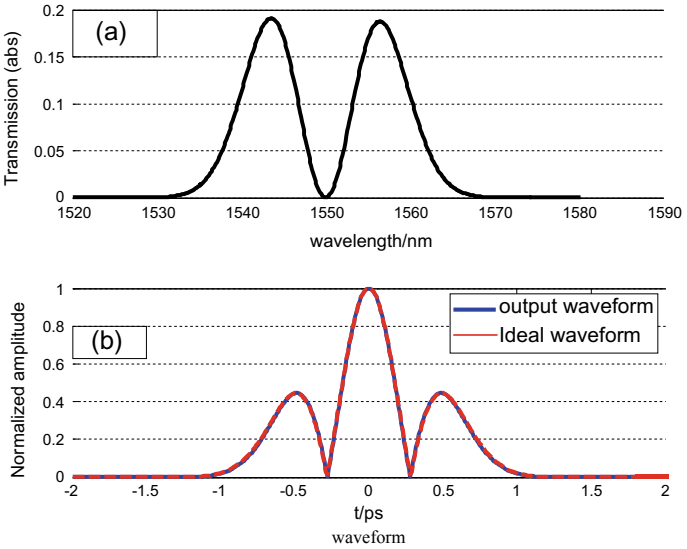

Fig. 5 Spectrum and time domain of Gaussian pulse derived by second-order differentiators based on LPWG. **a** Spectrum; **b** time domains

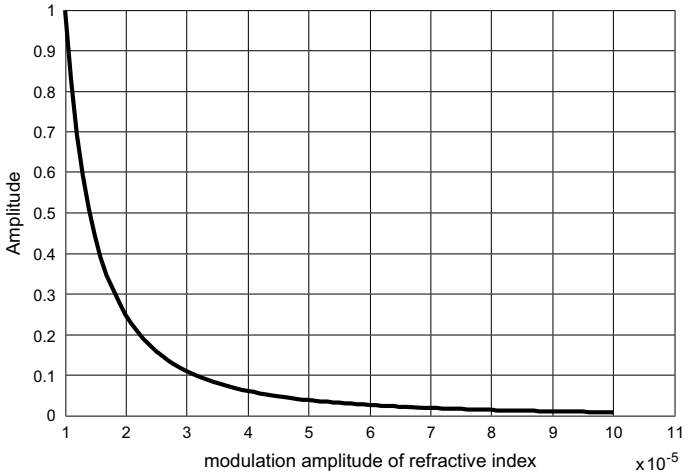

Fig. 6 Amplitude of second-order differentiator vesus ΔN

Acknowledgements This work was supported by National Natural Science Foundation of China (Project 61377075).

References

1. Slavík R, Park Y, Kulishov M et al (2006) Ultrafast all-optical differentiators. Opt Express 14(22):10699
2. Kulishov M, Krcmarík D, Slavík R (2007) Design of terahertz-bandwidth arbitrary-order temporal differentiators based on long-period fiber gratings. Opt Lett 32(20):2978–2980
3. Slavík R, Park Y, Azaña J et al (2009) Second-order photonic temporal differentiator based on a phase-shifted long period fiber grating. In: Leos meeting conference proceedings, Leos‘09. IEEE, pp 185–186
4. Jin W, Chiang KS, Liu Q (2008) Electro-optic long-period waveguide gratings in lithium niobate. Opt Express 16(25):20409–20417
5. Chiang KS, Wei J (2012) Electro-optic long-period waveguide grating devices. In: Opto-electronics and communications conference. IEEE, pp 545–546
6. Erdogan T (1997) Fiber grating spectra. J Lightwave Technol 15(8):1277–1294
7. Zhou J, Fu S, Aditya S et al (2009) Photonic temporal differentiator based on polarization modulation in a $LiNbO_3$, phase modulator. In: International topical meeting on microwave photonics. IEEE, pp 1–3

Silicon Photonics Carrier-Induced Waveguide Bragg Grating with Tunable Extinction Ratio

Qing Fang, Juan Hu, Xiaoling Chen, Zhiqun Zhang, Wei Wang, and Song Feng

Abstract In this paper, we demonstrated PIN-type and PN-type silicon Bragg gratings using ion implantation technology. This carrier-induced PIN-type silicon Bragg grating can be modulated under a forward bias, and its extinction ratio decreases with the increase of forward bias. The optical 3 dB-bandwidth of 0.45 nm and the ER of 19 dB are achieved on the PN-type Bragg grating. With the carrier injection, the ER modulation is more than 10 dB; with the carrier depletion, the ER modulation is more than 11.5 dB. The electrical modulation speed is fast. An eye-diagram with a data rate of 8 Gbps is measured.

Keywords Silicon photonics · Waveguide grating · Carrier-induced · Extinction ratio modulation

1 Introduction

Bragg grating-based optical devices have been using widely in optical communication systems, especial the fiber Bragg grating filter [1]. Due to the low index difference in the optical fiber, the Bragg grating length is normally long. On the other hand, it is hard to realize high-speed modulation in the fiber Bragg grating filter. Silicon photonics had become an amazing research hotspot in the last decade because of excellent performances and low cost of silicon materials. Many kinds of silicon Bragg gratings formed by etching process were reported, recently [2, 3]. This kind of silicon Bragg grating structure is permanent, and its reflected wavelength

Q. Fang (✉) · J. Hu · X. Chen · Z. Zhang
Kunming University of Science and Technology, Kunming 650500, China
e-mail: qingfang@kmust.edu.cn

Q. Fang · W. Wang
Shanghai Industrial μTechnology Research Institute, Shanghai 201800, China
e-mail: Wayne.Wang@sitrigroup.com

S. Feng
School of Science, Xi'an Polytechnic University, Xi'an 710048, China

L. Xu and L. Zhou (eds.), *Proceedings of the 8th International Multidisciplinary Conference on Optofluidics (IMCO 2018)*, Lecture Notes in Electrical Engineering 531,
https://doi.org/10.1007/978-981-13-3381-1_15

exists in the spectrum once it is formed by etching process. In this paper, we demonstrated both PIN-type and PN-type silicon Bragg gratings using ion implantation technology. This carrier-induced PIN-type silicon Bragg grating can be modulated under a forward bias, and its extinction ratio decreases with the increase of forward bias. However, it is hard to modulate the extinction ratio under a reverse bias because the finger length is hard to change with a reverse bias. The PN-type carrier-induced silicon Bragg grating is using the same ion implantation technology on SOI platform. The extinction ratio of this PN-type silicon Bragg grating can be modulated under both reverse biases and forward biases.

2 Design and Fabrication

The Bragg grating finger is composed of low *P* and low *N* implantation, shown in Fig. 1. The instinct *Si* range is designed between each finger of Bragg grating. The finger pattern is formed by implantation. According to the plasma dispersion effect in silicon, the refractive index of silicon will change with the increase of the ion concentration. The refractive index in *P* (*P*−) and *N* (*N*−) implantation areas decreases when implantation is processed. On the other hand, the refractive index in the instinct Si range is not changed. So, the Bragg grating is formed by ion implantation. The designed parameters are listed in Table 1.

The carrier-induced Bragg grating was fabricated on an 8-inch silicon-on-insulator (SOI) wafer with 220 nm top Si layer and 2 μm buried oxide. The fabrication process is similar to the PN-type silicon modulator. The carrier concentration near the junction is around 5×10^{17} atoms/cm^3 in the finger areas. The AFM image of the dosed silicon waveguide is shown in the left of Fig. 2 after all implantations and annealing. The surface roughness along the dosed silicon waveguide is shown in the right of Fig. 2. The results show that the silicon of less than 1.5 nm is lost in the implantation area. Its contribution to the extinction ratio of reflected wavelength can be negligible.

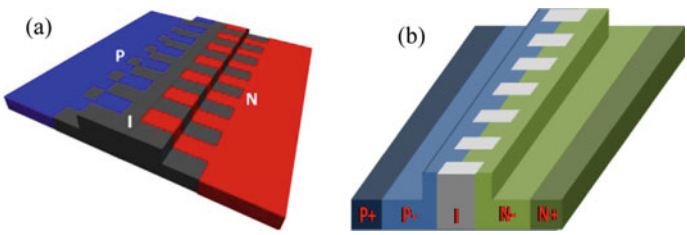

Fig. 1 Schematic of the carrier-induced Bragg grating. **a** PIN-type, **b** PN-type

Table 1 Design parameters of Bragg grating

Bragg grating type	Items	Value
PN-type	Top silicon thickness (nm)	220
	Rib width (nm)	400
	Slab height (nm)	110
	Grating period (nm)	310
	Duty cycle	50:50
PIN-type	Top silicon thickness (nm)	220
	Rib width (nm)	400
	Slab height (nm)	130
	Grating period (nm)	310
	Duty cycle	50: 50

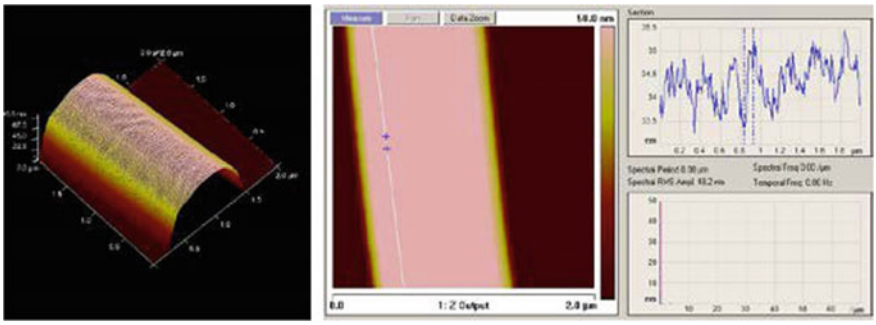

Fig. 2 AFM image and surface roughness of Bragg grating after implantations and annealing

3 Characterization and Analysis

The measured spectra of this PIN-type/PN-type Bragg grating filters with biases for TE mode is shown in Figs. 3 and 4, respectively. In Fig. 3, the excess loss caused by the implantation is ~1.5 dB and the reflected central wavelength is 1581.80 nm. The extinction ratio is ~14 dB. The measured bandwidth of PIN-type grating is 0.3 nm. Under the different forward biases, the central wavelength shifting rates is −1.35 nm/V. With the forward bias of 1.5 V, the extinction ratio reduces to ~5 dB.

In Fig. 4, the transmission loss is 2.5 dB and the reflected wavelength is 1590.15 nm without any bias. The corresponding extinction ratio is ~19 dB. In consideration of the propagation loss (2.5 dB/cm) of undoped ridge Si waveguide, the excess optical loss from implantation is ~2.0 dB. The extinction ratio modulation of more than 10 dB is realized at the forward voltage of 1.5 V. The high-speed measured result of PN-type Bragg grating is in Fig. 5. When the reverse bias is −20 V, the optical loss of this grating reduces to 1.0 dB from 2.5 dB and an extinction ratio modulation of more than 11.5 dB is realized. The eye diagram of 8 Gbps is measured, shown in Fig. 5.

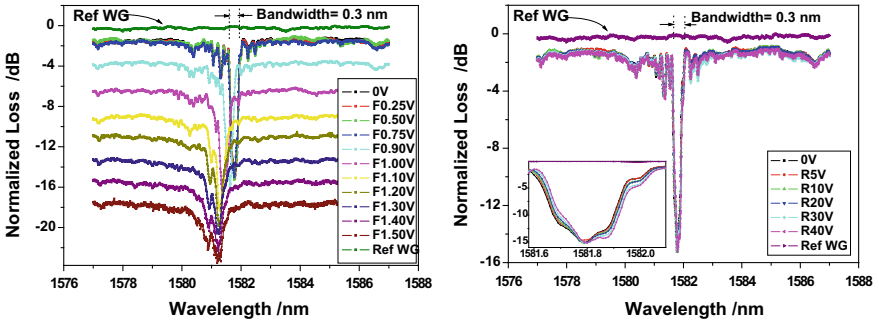

Fig. 3 Optical transmission spectra of PIN-type Bragg grating. Left: forward biases; right: reverse biases

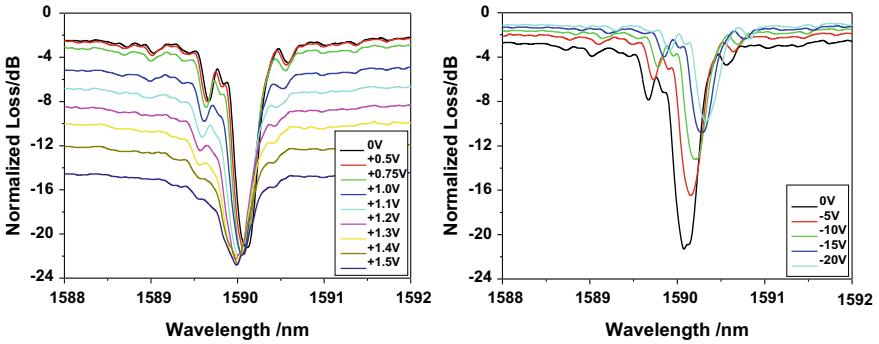

Fig. 4 Optical transmission spectra of PN-type Bragg grating. Left: forward biases; right: reverse biases

Fig. 5 8 Gbps Eye diagram of PN-type grating

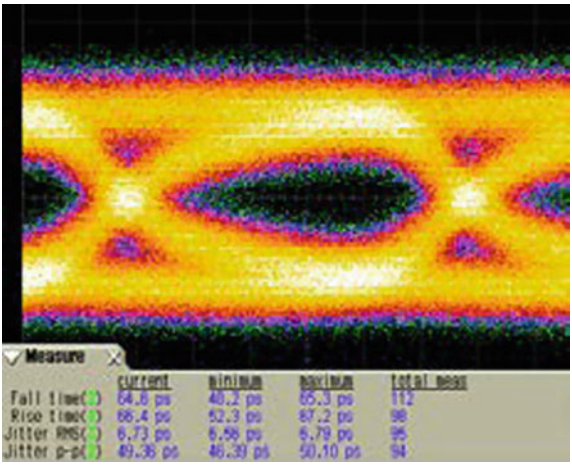

4 Conclusion

In conclusion, PIN-type and PN-type carrier-induced silicon Bragg gratings formed by ion implantation technology was demonstrated. The extinction ratio of both grating filters is 14 dB and 19 dB, respectively. With the forward bias of 1.5 V, the extinction ratio of PIN-type grating reduces to ~5 dB. Under the reverse bias and forward bias, extinction ratio modulations of PN-type grating are ~11.5 dB and ~10 dB, respectively. The modulation frequency of this carrier-induced is very fast, and the eye diagram of 8 Gpbs data rate is achieved.

Acknowledgements This work was supported by the National Natural Science Foundation of China (Grant No. 61764008 and No. 61674072), the Opened Fund of the State Key Laboratory of Integrated Optoelectronics (Grant No. IOSKL2017KF11), the Natural Science Foundation of Shanxi Province of China (Grant Nos. 2017JM6075), the Foundation of Shaanxi Provincial Education Department (Grant Nos. 17JK0335) and the Foundation of State Key Laboratory of Functional Materials for Informatics (Grant Nos. SKL201804).

References

1. Tsuda H (2010) Fiber Bragg grating vibration-sensing system, insensitive to Bragg wavelength and employing fiber ring laser. Opt Lett 35:2349–2351
2. Jiang G et al (2011) Slab-modulated sidewall Bragg grating in silicon-on-insulator ridge waveguides. IEEE Photon Technol 23:6–8
3. Honda S et al (2007) Largely-tunable wideband Bragg gratings fabricated on SOI rib waveguides employed by deep-RIE. Electron Lett 43:630–631

Simulation Design of Exosomes Separation Microfluid Device Based on Asymmetrical Flow Field-Flow Fractionation

Mingyu Yuan, Chengjun Huang, Wenbing Fan, Xiaonan Yang, and Mingxiao Li

Abstract Exosomes are extracellular nano-scale vesicles with a diameter of about 40–100 nm and a density of about 1.13–1.19 g/ml, which are secreted by most cells and have phospholipid bilayer structure on their surface. Exosomes contain a large amount of genetic information and a variety of proteins involved in cell–cell communication and macromolecular transmission. At present, the importance of exosomes in the early diagnosis and targeted treatment of diseases is widely noticed. Thus, efficient separation method for exosomes separate is urgent. In this paper, the flow field-flow fractionation method was used to separate the latter from the mixture of BSA and exosomes. Model construction and simulation were performed using commercial software COMSOL Multiphysics. According to the results of the simulation and theoretical analysis, the method can achieve rapid, effective and compatible separation of exosomes. Finally, according to the simulation results, some reference opinions can be provided for the actual microfluidic chip production, and the subsequent applications are prospected.

Keywords Exosomes · Flow field-flow fractionation · Separation · Simulation · Microfluidic

M. Yuan · W. Fan · X. Yang (✉)
School of Information Engineering, Zhengzhou University, Zhengzhou, China
e-mail: iexnyang@zzu.edu.cn

M. Yuan · C. Huang · M. Li (✉)
Institute of Microelectronics of Chinese Academy of Sciences, Beijing, China
e-mail: limingxiao@ime.ac.cn

C. Huang
University of Chinese Academy of Sciences, Beijing, China

L. Xu and L. Zhou (eds.), *Proceedings of the 8th International Multidisciplinary Conference on Optofluidics (IMCO 2018)*, Lecture Notes in Electrical Engineering 531,
https://doi.org/10.1007/978-981-13-3381-1_16

1 Introduction

Exosomes have been the focus of researchers since their discovery and naming in 1987 [1]. Nowadays, exosomes have great potential as circulating biomarkers of disease, and it can also be used as a medium for remote intercellular communication in the body. Biofluids (such as blood, saliva, urine, etc.) contain a large number of exosomes that can transfer various molecules from parental cells to other cells, including proteins, mRNA/miRNA and DNA, so it can be used as a cell replacement [2]. In addition, exosomes are also a significant advantage as cancer monitors [3].

Exosomes are relatively new targets for bioassays that have unique physical and biological properties: Their size range (typically 40–100 nm in diameter) is much smaller than cells (10–30 um), but larger than protein and comprises a highly heterogeneous constituency [4]. Traditional methods for separating exosomes are as follows: ultracentrifugation, sucrose-gradient centrifugation, size-exclusion chromatog-raphy [5], etc. They all have some limitations, such as time-consuming, low recovery rate or low purity. Thus, efficient separation method for exosomes separate is urgent.

Asymmetrical flow field-flow fractionation (AF4) is a sub-class of field-flow fractionation techniques developed by Giddings in 1966 [6]. It is based on the difference in diffusion coefficient to complete the sample separation. Separation is done in a flat channel, the channels are distributed in a laminar flow, and in the direction of the vertical laminar flow, another flow field is applied, which is called a cross-flow. Samples with different diffusion coefficients are balanced at different locations in the channel by cross-flow to move toward the channel exit at different speeds. However, most AF4 analysis tools have been optimized for other biological objects with limited sensitivity and throughput for exosomes separation.

In this paper, we implemented the process of separating the exosomes from the AF4 system on the simulation software. The results in our work verify that AF4 technique has great potential for exosomes separation. And provide guidance for the subsequent actual device fabrication.

2 Experiment

In this study, COMSOL Multiphysics® 5.2 software was used to separate proteins (bovine serum albumin, BSA) and exosomes. The technique used for the simulation is the previously mentioned asymmetrical flow field-flow fractionation (AF4). The separation is based on an ultrafiltration membrane that retains the solutes when a cross-flow is applied.

A 2D model was used to describe this system. Flow profile and samples migration are predominantly homogeneous along the breadth of the channel and that enabled to reduce the model to two dimensions. A mesh was created with very fine elements in the proximity to the bottom flat permeable surface (membrane) as samples migration

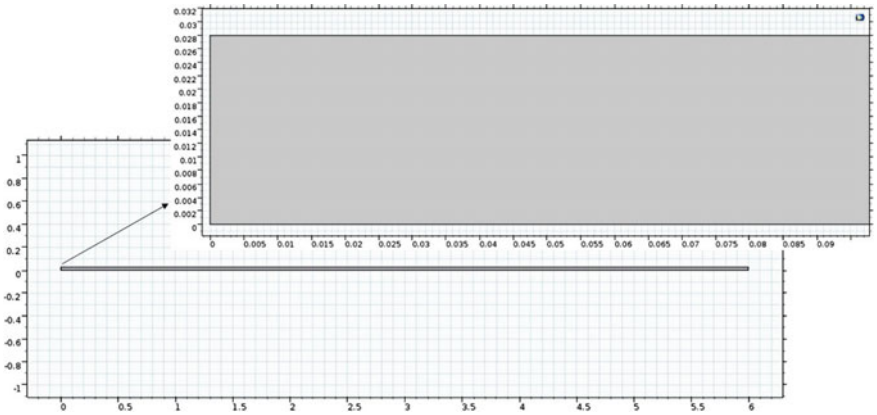

Fig. 1 COMSOL 2D simulation model diagram. Since it is a long, flat channel, a partially enlarged picture is added at the top of the figure

takes place in this region. A rectangle of 6 cm in length and 280 μm in height was drawn as a separation channel (Fig. 1).

To describe the flow, single-phase laminar flow was used, and boundary conditions (inlet, outlets) were set to define channel flow and cross-flow. The study of the flow profile was solved as stationary-state problem, and this output was used to solve the time-dependent problem of samples migration. Transport of diluted species (convection and diffusion) was used to simulate samples of two different sizes, BSA and exosomes with hydrodynamic radius 3.7 nm and 20 nm respectively.

3 Results and Discussion

3.1 Flow Rate and Concentration Distributions

After optimizing the parameters of the 2D flow rate stationary-state simulation, the obtained flow velocity and concentration simulation results and partial enlargement patterns are shown in Fig. 2. It can be seen from Fig. 2a that the flow velocity at the center of the channel is much larger than the flow velocity of the upper and lower walls of the channel, and the channel flow for carrying current is in the form of laminar flow (parabolic type). In Fig. 2b, at the lower wall of the channel, there is a vertically downward flow field, indicating that the cross-flow is present in the channel, and that the curve of the streamline can also be seen from the direction of the streamline in the channel. It is also the effect of cross-flow. In contrast, the velocity of the channel flow is much greater than the speed of the cross-flow, so that it does not change the general distribution of the fluid in the entire channel.

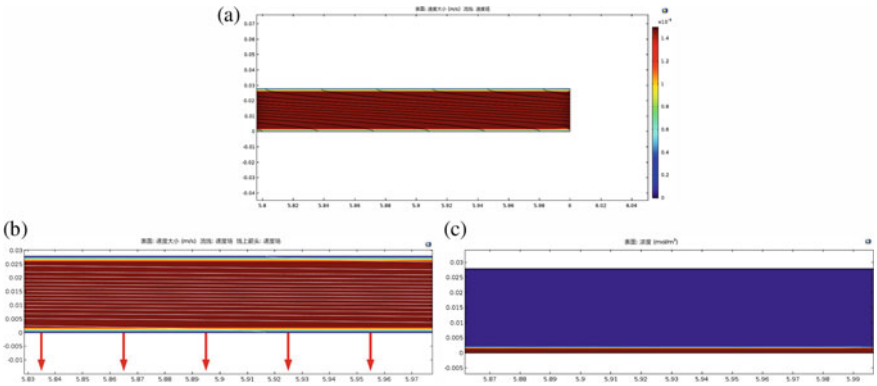

Fig. 2 Two-dimensional stationary-state flow rate simulation and concentration results. The figure is the physics field distribution near the exit

The distribution of sample concentration in the channel can also be represented by a two-dimensional stationary-state simulation (Fig. 2c). It can be seen from the simulation results that the sample is almost concentrated at the accumulation wall of the channel, again illustrating the effect of the cross-flow on the entire channel, and in the steady state, the concentration at the bottom of the channel entrance is almost zero. This is because when setting up sample injection, the concentration is injected into the channel as a pulse rather than a continuous injection channel.

3.2 Effect of Separation

The 2D distribution of flow rate and concentration can only observe some phenomena from the image, but it cannot quantitatively explain that the two samples with different diffusion coefficients have been separated. Therefore, a 1D function curve is needed to characterize the relationship of concentration over time at the exit of the channel.

In the simulation process, the transport of diluted species interface is used to enable 1D time-dependent analysis. Both samples enter the inlet at the same time with the Gaussian pulse. Since the different diffusion coefficients cause a difference in the transfer speed, at the exit, the two flow out of the channel at different times (Fig. 3).

According to the 1D function curve, it can be seen that the two substances exit the channel at different times at the exit. The blue line represents BSA, and the green one represents exosomes. Since the particle sizes of the two samples differ greatly, the time of the outflow channel is also quite different. This result is similar to the theoretical calculations, and the feasibility of the AF4 method for exosomes separation can be demonstrated using a simulation method.

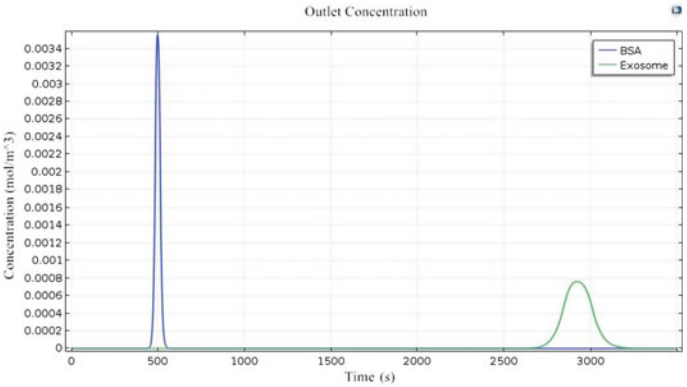

Fig. 3 1D plot of export concentration versus time. The curves in the legend indicate two different colors representing BSA and exosomes

4 Conclusions

In this study, the theory of field-flow separation was applied to the separation of exosomes. Through theoretical analysis and simulation design, two-dimensional and one-dimensional simulation results were obtained, and the results were used to confirm that the method can separate exosomes. A simulation platform is built for constructing the field-flow fractionation device. If the added physical field and sample are modified, the method can also be used for simulation. Moreover, the fabrication of the actual microfluidic separation device can play a role of auxiliary reference. By modifying the size parameters of the device and the parameters of each physical field interface, a more suitable physical device can be obtained.

References

1. Johnston RM, Adam M, Hammond JR, Orr L, Turbide C (1987) Vesicle formation during reticulocyte maturation. J Biol Chem 262:9412–9420
2. Keerthikumar S, Chisanga D, Ariyaratne D, Al Saffar H, Anand S, Zhao K, Samul M, Pathan M, Jois M, Chilamkurti N et al (2016) Exocarta: a web-based compendium of exosomal cargo. J Mol Biol 428:688–692
3. Böing AN, Harrison P, Sturk A, Nieuwland R (2012) Classification, functions, and clinical relevance of extracellular vesicles. Pharmacol Rev 64:676–705
4. Yáñez-Mó M, Siljander PRM, Andreu Z, Borràs FE, Buzas EI, Buzas K, Casal E, Cappello F, Carvalho J et al (2015) Biological properties of extracellular vesicles and their physiological functions. J Extracell Vesicles 4:27066
5. Nordin JZ, Lee Y, Vader P, Mager I, Johansson HJ, Heusermann W, Wiklander OP, Hallbrink M, Seow Y, Bultema JJ et al (2015) Ultrafiltration with size-exclusion liquid chromatography for high yield isolation of extracellular vesicles pre-serving intact biophysical and functional properties. Nanomedicine 11:879–883
6. Giddings JC (1966) A new separation concept based on a coupling of concentration and flow nonuniformities. J Sep Sci 1(1):123–125

Papers from the 9th International Multidisciplinary Conference on Optofluidics (IMCO 2019)

Editors:
Xuming Zhang, The Hong Kong Polytechnic University, Hong Kong, China
Yi Zhang, Nanyang Technological University, Singapore

Design of a Microfluidic Chip for Separating Rice Disease Spores

Gangshan Wu, Chiyuan Chen, Ning Yang, Haifang Hui, and Peifeng Xu

Abstract Rice is one of the world's important food crops, but its output is affected by disease all year round. Among them, the pathogens of rice smut and sheath blight are the two most typical fungal pathogens infesting rice. Therefore, the detection of pathogenic spores is very important for studying the occurrence and development of rice diseases. In this paper, a microfluidic chip for the separation of spores of rice smut is designed. The microfluidic chip adopts a two-stage separation structure. The first-stage separation structure adopts a periodic rectangular recess structure on the side of the separation channel to achieve the purpose of separating air spores. The second-stage separation structure adopts a vertical sheath flow channel structure to enhance the separation effect. The paper used a microscope to photograph spore images to verify the separation effect. The experimental results show that the chip can complete the separation of the rice smut spores.

Keywords Spore detection · Microfluidic chip · Spore separation

1 Introduction

In 2006–2015, Chinese crops were frequently threatened by various pests and diseases [1]. Rice has a long history of planting in China, with an average annual planting area of 30 million hm^2, accounting for about one-third of the area planted with food crops. It is one of the indispensable food crops in China [2]. However, the annual economic loss caused by the reduction of rice production caused by pests and diseases in China is between 4 million and 5 million tons [3, 4].

It has become an important means of disease prevention and control by detecting the type and content of fungal spores in the air to achieve timely warning of epidemic

G. Wu · P. Xu
Jiangsu Polytechnic College of Agriculture and Forestry, 211121 Jurong, China

C. Chen · N. Yang (✉) · H. Hui
Jiangsu University, 212013 Zhenjiang, China
e-mail: 864315462@qq.com

L. Xu and L. Zhou (eds.), *Proceedings of the 8th International Multidisciplinary Conference on Optofluidics (IMCO 2018)*, Lecture Notes in Electrical Engineering 531,
https://doi.org/10.1007/978-981-13-3381-1_17

diseases in the air [5, 6]. The traditional methods for detecting spores of crop diseases are mainly weighing method and microscopic counting method. The results obtained by these two methods are susceptible to impurities [7].

According to the above reasons, finding a convenient and low-cost method for separating impurities has become a hot topic in current research. The microfluidic chip has the advantages of minimal consumption of reagents, rapid and automatic detection, low cost, and high degree of integration. Based on the above technology, a chip capable of efficiently performing spore separation is designed to realize rapid detection of spores.

2 Methods and Materials

2.1 Design of Microfluidic Chip

In order to achieve automatic separation of aggregated spores, a microfluidic chip comprising a two-stage structure as shown in Fig. 1a was designed. The first part is called the passive separation structure. As shown in Fig. 1b, it mainly solves the agglomeration phenomenon of air fungal spores. With the periodic collision and extrusion of the chip channel, the aggregated spores can repeatedly collide with the chip channel and decompose. The second part is called the active separation classification structure. As shown in Fig. 1c, the spores of lightweight are more susceptible to external motion and change the motion state, so a small external force perpendicular to the initial velocity direction can be introduced. Different types of spores are classified.

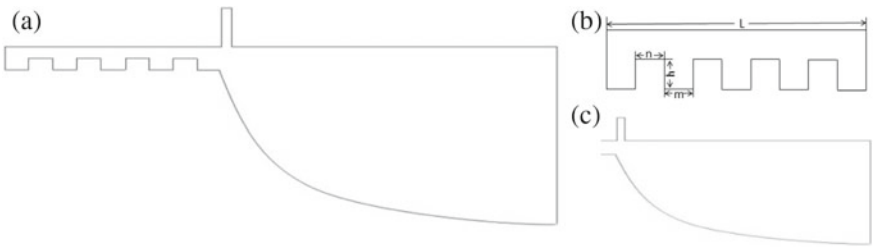

Fig. 1 Microfluidic chip design. **a** Overall design, **b** passive separation structure, **c** active separation classification structure

2.2 Numerical Method

Here is a microfluidic chip design diagram with a chip thickness of 100 μm, an entrance width of 500 μm, and an entrance from the first rectangular depression of 1000 μm in Fig. 1. The last rectangular depression is 500 μm from the inlet of the active separation structure; the width of the sheath flow inlet of the active separation structure is 200 μm, and the length of the upper channel wall is 700 μm.

It is assumed that the airflow is a stable two-dimensional flow, axisymmetric, and incompressible. The temperature was 20 °C, and the gas pressure was 101.3 kPa. The side walls of the chip were set to have no slip, the left inlet flow rate was 10 mm^3/s, and the sheath flow rate was 1 mm^3/s. After the airflow simulation, the particle motion was studied. Simulate particle motion used COMOSOL Multiphasic 5.1. The side walls of the chip were set to adhere, the particle density was 1000 kg/m^3, and the particle diameter was 2 and 16 μm.

3 Results and Discussions

3.1 Particle Motion Simulation

First, h and L are optimized, and the simulation results are shown in Fig. 2a. The aggregate spore separation effect is best when the height of the rectangular depression is $h = 0.3$ mm. Therefore, the length L of the passive separation structure does not affect the separation effect, and the separation effect is best when the height h of the rectangular depression is 0.3 mm. Then, the values of n and m are optimized. The experimental results are shown in Fig. 2b. When the inter-rectangular depression m is a certain value, $n = 0.4$ mm, the separation effect of the aggregate spores is the best. According to the above experiment, h is 300 μm, n is 400 μm, L is the length of four continuous rectangular concave structures, and m is 0.5 mm.

Figure 2c is a flow chart of the flow rate of the microfluidic chip. Figure 2d is the particle separation case, because of the inertia, where 2 μm particles are located below the chip separation region and 16 μm particles are located above the chip separation region.

3.2 Experimental Results

Figure 3 is an image taken by scanning electron microscopy, and the rice smut spores are clearly separated.

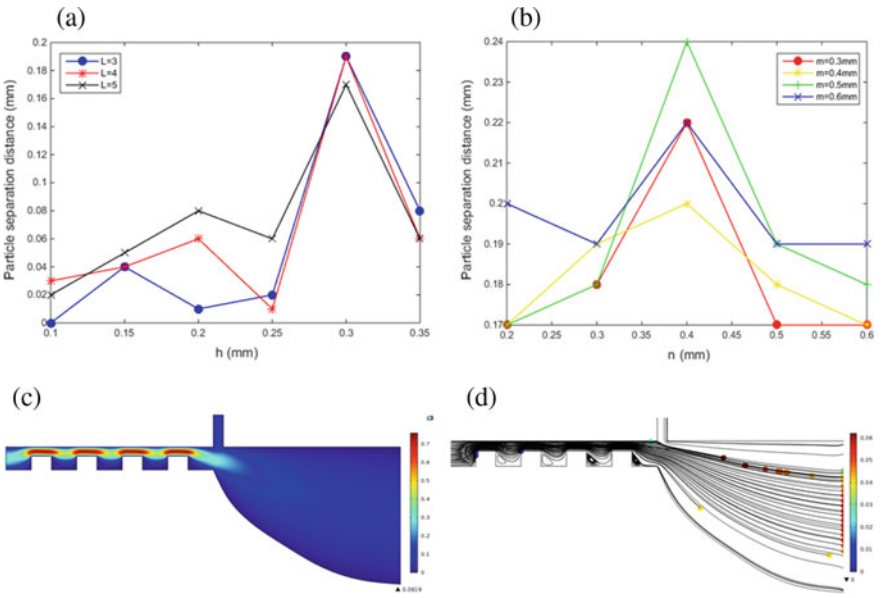

Fig. 2 **a** Influence of the height of rectangular recess h and the number of rectangular, **b** effect of rectangular recess length n and rectangular interval m on particle separation results, **c** velocity distribution in chip, **d** particle separation in chip

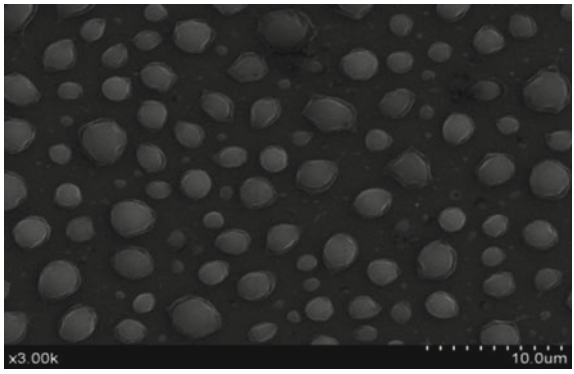

Fig. 3 Isolation of spores from rice blast

4 Conclusions

The paper designed a microfluidic chip for the isolation of rice smut spores, including passive separation and active separation. The optimal parameters to maximize chip separation efficiency were investigated. Experiments show that the designed microfluidic chip can separate the agglomerated spores.

Acknowledgements This research was financially supported by the Research on Intelligent System for Early Diagnosis of Main Strawberry Pests and Diseases Based on Deep Learning (2018kj11), Chinese National Natural Science Foundation (31701324), China Post-doctoral Science Foundation Project (2018M642182), Jiangsu Agricultural Science and Technology Innovation Fund (CX(18)3043), Outstanding Youth Science Foundation of Jiangsu province (BK20180099), Zhenjiang Dantu Science and Technology Innovation Fund (Key R&D Program-Social Development) (SH2018003), the Priority Academic Program Development of Jiangsu Higher Education Institutions (PAPD).

References

1. Walters DR (2013) Controlling crop diseases using induced resistance: challenges for the future. J Exp Botany 64(5):1263
2. Webster RK (2012) Compendium of rice diseases. Dis Compendium 84(6):953
3. Yang JH (2010) Diversity analysis of antagonists from rice-associated bacteria and their application in biocontrol of rice diseases. J Appl Microbiol 104(1):91–104
4. Zhu Y (2000) Genetic diversity and disease control in rice. Nature 406(6797):718
5. Zheng A (2013) The evolution and pathogenic mechanisms of the rice sheath blight pathogen. Nat Commun 4(1424):1424
6. Qin Z (2005) Detection of rice sheath blight for in-season disease management using multispectral remote sensing. Int J Appl Earth Obs Geoinf 7(2):115–128
7. Pellegrino PM (2002) Enhanced spore detection using dipicolinate extraction techniques. Anal Chim Acta 455(2):167–177

Harmonic Mode Locking of Dual-Wavelength Mode-Locked All-Fiber Laser

Xinyu Huang, Bo Cao, and Xiaosheng Xiao

Abstract We report the experimental observation of harmonic mode locking of a dual-wavelength all-fiber laser with different repetition rates. Dual-wavelength mode locking with individual fundamental repetition rates could be generated in the laser. By adjusting the intracavity polarization controller, harmonic mode locking of both wavelengths can be generated, and the difference of harmonic repetition rates is stable. This investigation not only enriches the nonlinear dynamics of mode-locked lasers, but also has potential applications related to the dual-comb based on a free-running fiber laser.

Keywords Mode-locked fiber laser · Harmonic mode locking · Dual-comb

1 Introduction

Passively mode-locked fiber lasers have been investigated intensely, due to their important applications in many fields. As ultrashort optical pulse sources, they show the advantages of low-cost, compactness, and stability. In addition, the mode-locked fiber lasers are ideal platform for nonlinear science investigations [1]. An interesting phenomenon in passively mode-locked fiber laser is that pulse trains with different repetition rates can simultaneously exist in a single cavity. In 2008, an all-fiber bidirectional mode-locked laser was proposed, where the pulses could operate in both directions since there is no isolator in the cavity [2]. Birefringence-induced asynchronous pulse trains with different polarization states were also investigated in fiber lasers. For example, pulse trains with orthogonal polarizations were proposed in a unidirectional fiber laser [3]. Pulse nonlinear dynamics was also reported in the fiber lasers with asynchronous pulse trains. Bound solitons was observed in a bidirectional mode-locked fiber laser [4]. Coexistence of dissipative soliton and

X. Huang · B. Cao · X. Xiao (✉)
State Key Laboratory of Precious Measurement Technology and Instruments, Department of Precision Instruments, Tsinghua University, 100084 Beijing, China
e-mail: opticsxiao@qq.com

L. Xu and L. Zhou (eds.), *Proceedings of the 8th International Multidisciplinary Conference on Optofluidics (IMCO 2018)*, Lecture Notes in Electrical Engineering 531,
https://doi.org/10.1007/978-981-13-3381-1_18

stretched pulse was reported in a dual-wavelength fiber laser due to the significant wavelength-dependent net cavity dispersion [5].

Fiber lasers with asynchronous pulse trains have promising applications in many fields, especially serving as a simple dual-comb source. Sharing the same cavity, there is inherently mutual coherence between the two pulse trains [2]. Bidirectional fiber laser was proposed for fiber Bragg grating interrogation, which can be used for multiplexed static strain sensing [6]. Dual-comb spectroscopies were demonstrated by use of a free-running bidirectionally fiber laser [7] and a dual-wavelength fiber laser [8], respectively.

Mode-locked fiber lasers usually generate multiple pulses due to wave breaking. An interesting and special regime of multiple pulse is passive harmonic mode locking observed in 1993 [9], where all the output pulses are equally separated and the pulse repetition rate is multiple of the fundamental repetition rate. For the applications such as dual-comb distance measurement, the increases of repetition rate will improve the performance, e.g., shortening the refresh time.

In this paper, harmonic mode locking is investigated in a dual-wavelength all-fiber laser with asynchronous pulse trains. The difference of repetition rates is larger than the case operating with fundamental repetition rate. Further measurement shows that the difference of repetition rates is stable.

2 Experimental Setup

Figure 1 shows the experimental setup. The fundamental repetition rate is ~39 MHz. The laser is passively mode-locked by the combination of nonlinear polarization ration (NPR) and carbon nanotube (CNT). The CNT, placed between two fiber ferrules to form a saturable absorber, mainly contributes to the mode locking. Meanwhile, two polarization controller (PCs) and a polarization-dependent isolator (PD-ISO) form NPR, assisting the mode locking.

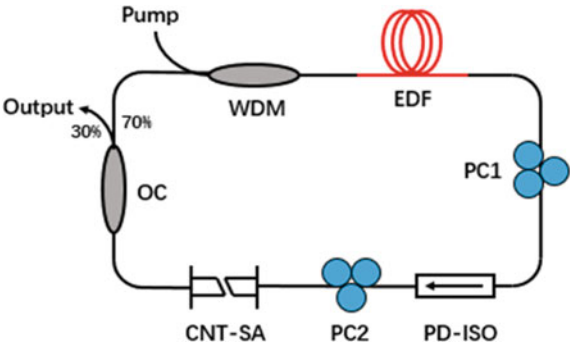

Fig. 1 Schematic of the experimental setup. WDM, wavelength division multiplexing; EDF, erbium-doped fiber; PC, polarization controller; PD-ISO, polarization-dependent isolator; CNT-SA, carbon nanotube saturable absorber; OC, optical coupler

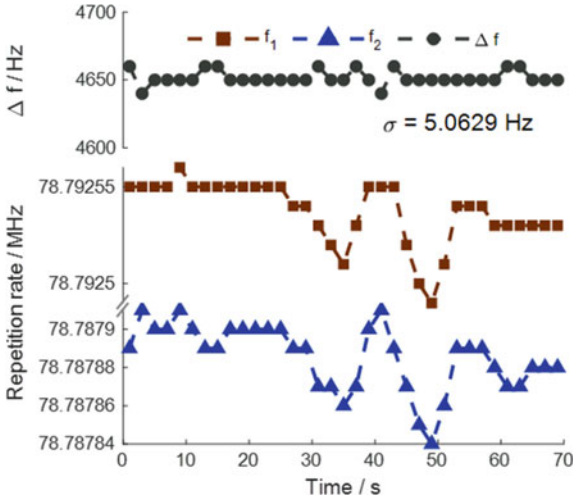

Fig. 2 Repetition rates drift and difference (Δf) of the asynchronous pulse trains in the dual-wavelength mode-locked fiber laser with harmonic mode locking

3 Experimental Results

By properly setting the PCs, mode locking (with single pulse train) can be achieved at two different central wavelengths, respectively. Furthermore, dual-wavelength mode locking with individual fundamental repetition rates (around 39 MHz) could be generated in the laser. In the case of dual-wavelength mode locking, by further adjusting the PCs, up to several tens order harmonic mode locking at one of the wavelength could occur, while the other wavelength keeps operating at fundamental repletion rate. More interestingly, harmonic mode locking of both wavelengths can also be generated, which double the repetition frequency difference of that at fundamental repetition.

To investigate the stability of the dual-comb based on the dual-wavelength fiber laser, the difference of two repetition rates of harmonic mode locking are measured in a period of time. As shown in Fig. 2, the repetition rates (twice of the fundamental repetition rate) of the two wavelength drifts in similar tendencies, which results in a small drift of Δf with standard deviation of 5 Hz.

4 Conclusion

Benefiting from the saturable absorption mechanism provided by the combination of CNT and NPR, harmonic mode locking of asynchronous pulse trains with different wavelengths is achieved in an all-fiber laser. The stability of the repetition rate difference is experimentally confirmed, the standard deviation of which is about 5 Hz. Our

work provides a potential way to enlarge the repetition rates, as well as the difference of repetition rate, of dual-comb based on a single cavity, which may benefit the applications of dual-comb.

Acknowledgements This work was supported by the National Key Scientific Instrument and Equipment Development Project of China under Grant 2014YQ510403, and by the National Natural Science Foundation of China (NSFC) under Grant 51527901.

References

1. Grelu P, Akhmediev N (2012) Dissipative solitons for mode-locked lasers. Nat Photonics 6:84
2. Kieu K, Mansuripur M (2008) All-fiber bidirectional passively mode-locked ring laser. Optics Lett 33(1):64–66
3. Zhao X, Li T, Liu Y, Li Q, Zheng Z (2018) Polarization-multiplexed, dual-comb all-fiber mode-locked laser. Photonics Res 6(9):853–857
4. Li L, Ruan Q, Yang R, Zhao L, Luo Z (2016) Bidirectional operation of 100 fs bound solitons in an ultra-compact mode-locked fiber laser. Opt Express 24(18):21020–21026
5. Wang Y, Li J, Hong L, Li G, Liu F, Zhou X et al (2018) Coexistence of dissipative soliton and stretched pulse in dual-wavelength mode-locked Tm-doped fiber laser with strong third-order dispersion. Opt Express 26(14):18190–18201
6. Guo J, Ding Y, Xiao X, Kong L, Yang CJO (2018) Multiplexed static FBG strain sensors by dual-comb spectroscopy with a free running fiber laser. Optics Express 26(13):16147–16154
7. Mehravar S, Norwood RA, Peyghambarian N, Kieu K (2016) Real-time dual-comb spectroscopy with a free-running bidirectionally mode-locked fiber laser. Appl Phys Lett 108(23):231104
8. Zhao X, Hu G, Zhao B, Li C, Pan Y, Liu Y et al (2016) Picometer-resolution dual-comb spectroscopy with a free-running fiber laser. Opt Express 24(19):21833–21845
9. Grudinin AB, Richardson DJ, Payne DN (1993) Passive harmonic modelocking of a fibre soliton ring laser. Electron Lett 29(21):1860–1861

The Response Analysis of Multi-Field Coupled Piezoelectric Energy Harvester Under White Gaussian Noise Excitation

Xuhui Zhang, Meng Zuo, Lin Wang, and Xiao She

Abstract Due to the large vibration of fully mechanized mining equipment, using multi-field coupled piezoelectric energy harvester will efficiently solve the difficulty of wireless monitoring power supply by capture vibration energy. The study of dynamic characteristics of the MPEH under random excitation can effectively guide the design and optimization of the piezoelectric energy harvester. We make investigation of the distance effect of magnet, noise spectrum density and damping on the dynamic response characteristics of the MPEH under longitudinal and horizontal excitation. The results show that narrowing magnetic distance under longitudinal excitation, reducing damping ratio or increasing excitation spectral density can enhance the probability of large period vibration and increase the average power of the system.

Keywords Vibration energy harvesting · Multi-field coupled · Random excitation

1 Introduction

In recent years, the wireless sensor technology and intelligent monitoring technology has provided a new and effective way to replace the traditional wired underground environmental monitoring means in coal mines [1]. However, complex environment of coalmine means the difficulties of power supply of wired monitoring. The mechanical vibration produced in the working process of fully mechanized mining equipment in the coal mine is the most common kind of mechanical energy. Therefore, the

X. Zhang (✉) · M. Zuo (✉) · L. Wang · X. She
College of Mechanical Engineering, Xi'an University of Science and Technology, 710054 Xi'an, China
e-mail: zhangxh@xust.edu.cn

M. Zuo
e-mail: Zoezuom@163.com

X. Zhang
Shaanxi Key Laboratory of Mine Electromechanical Equipment Intelligent Monitoring, 710054 Xi'an, China

L. Xu and L. Zhou (eds.), *Proceedings of the 8th International Multidisciplinary Conference on Optofluidics (IMCO 2018)*, Lecture Notes in Electrical Engineering 531,
https://doi.org/10.1007/978-981-13-3381-1_19

construction of efficient vibration energy collection system is called upon to realize the self-power supply of wireless network nodes in coal mine [2, 3].

The piezoelectric vibration energy harvesting, owing to its superiority in structure and application, has been receiving more attention [4, 5]. The structural design of multi-field coupled piezoelectric energy harvester (MPEH) can effectively solve the problems of narrow resonance band of traditional linear piezoelectric harvester. Mechanical vibration is normally expressed as a broad-band random signal. Therefore, design and verification of MPEH should be studied not only under harmonic excitation, but also under random excitation.

2 Design and Modeling

The design of MPEH included four linear-arch beams, four flexible piezoelectric material polyvinylidene fluoride (PVDF), two permanent magnets and a mass block with permanent magnets in MPEH. The structure is illustrated in Fig. 1. Four PVDFs adhere to four metal beams, respectively. Four beams are connected to the same mass block, which has two permanent magnets on it. The distance between two adjustable magnets is changed by adjusting the screw thread of the casing.

Generalized Hamilton principle and piezoelectric theory are used [6] to obtain the model:

$$M\ddot{r}(t) + C\dot{r}(t) + Kr(t) - \theta v(t) - K_1 r(t) - K_2 r(t)^3 = -H_s \ddot{z}(t) \tag{1}$$

$$\theta r(t) + C_p v(t) + q = 0 \tag{2}$$

where $r(t)$ and $v(t)$ are the displacement mode function and voltage mode function, respectively. $\ddot{z}(t)$ denotes the acceleration of the base excitation. And, it will be instead as Gaussian white noise $W(\tau)$, which the spectral density is K_n, when excitation is random.

The axial and radial vibration signals of rocker arm in no-load operation of coal mining machine are measured and analyzed, respectively. It is noted that the highest

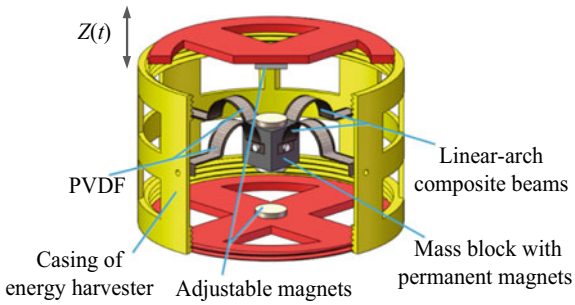

Fig. 1 Structural diagram of the MPEH

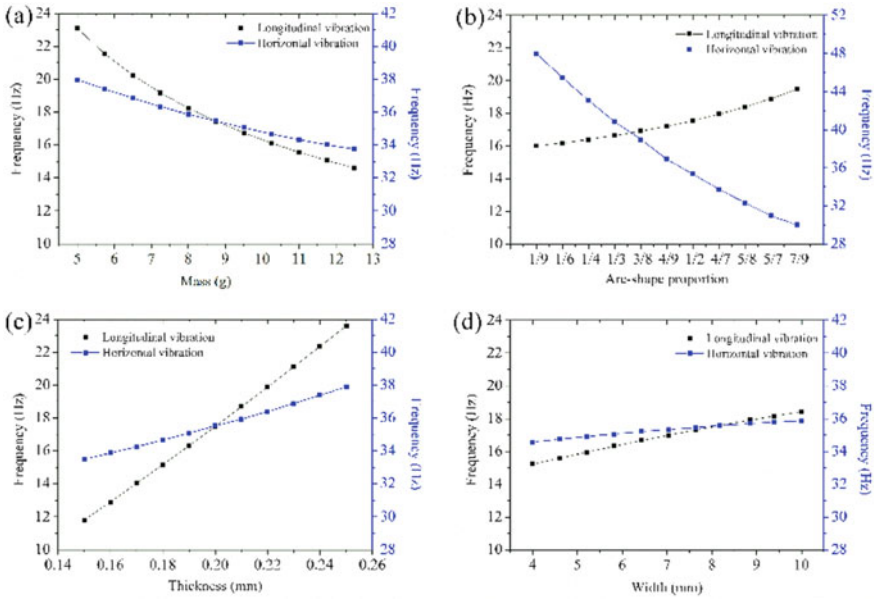

Fig. 2 Influence of structural parameters on resonance frequency of the MPEH

frequency range is between 15 and 25 Hz. Therefore, determining the structure size of the system to meet the requirements of excitation frequency is one of the important aspects of MPEH optimization design. The regularity of the influence of structural size is illustrated in Fig. 2.

3 Dynamic Response

In order to study the effect of magnet distance, noise spectral density and system damping on the response of the MPEH, the system response under random excitation is solved by the FPK equation method. The response results under longitudinal and horizontal excitation conditions are tested. In the following figures, the left are the longitudinal excitation condition, and the right are horizontal excitation (Figs. 3, 4, 5 and 6).

4 Conclusion

In order to adapt to the working frequency of coal mine machinery, structural optimization design of MPEH and the test under excitation conditions are carried out.

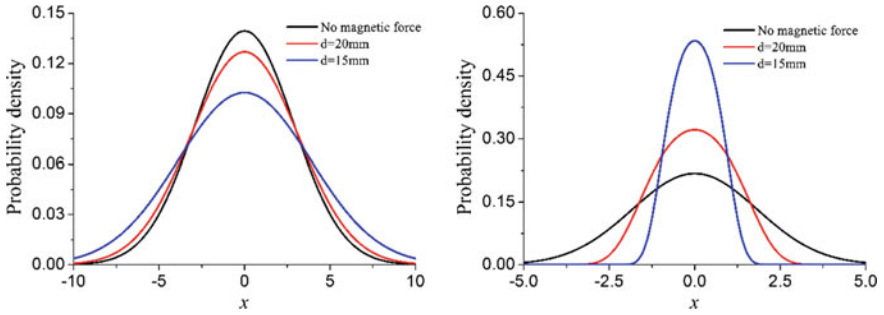

Fig. 3 Stationary probability distribution under different magnetic distances

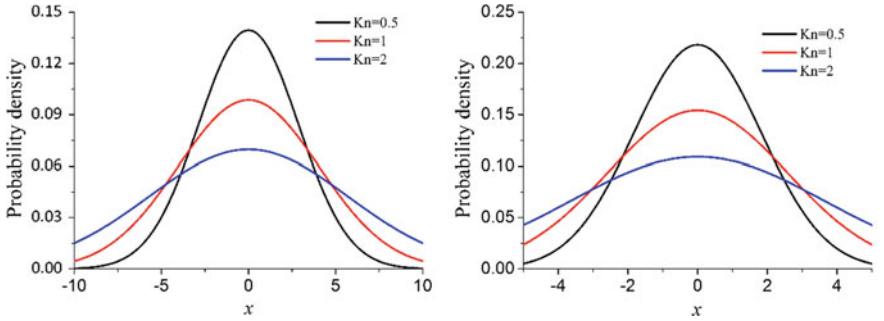

Fig. 4 Stationary probability distribution under different noise spectral densities

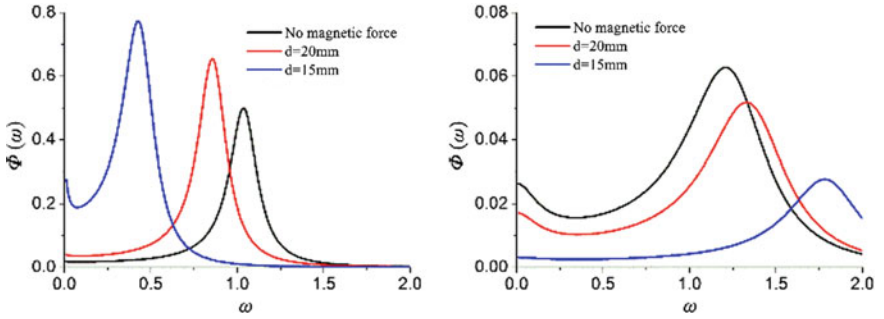

Fig. 5 Power spectral density under different magnetic distances

Under longitudinal excitation, add magnetic attraction and the magnetic distance is reduced, the variance of vibration probability distribution of the system increases and the probability of large period vibration increases. However, the influence of the magnetic distance is the opposite under horizontal excitation. Reducing damping ratio or increasing noise spectral densities will increase the system output.

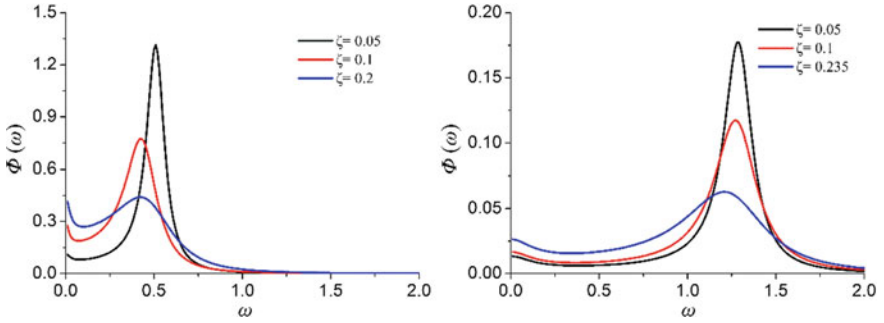

Fig. 6 Power spectral density under different damping ratios

References

1. He Q, Dong C, Li K, Wang J, Xu D, Li X (2018) A multiple energy-harvester combination for pattern-recognizable power-free wireless sensing to vibration event. Sens Actuators A Phys 279:229–239
2. Sudevalayam S, Kulkarni P (2011) Energy harvesting sensor nodes: survey and implications. IEEE Commun Surv Tutorials 13(3):443–461
3. Yang Z, Zhou S, Zu J, Inman D (2018) High-performance piezoelectric energy harvesters and their applications. Joule 2(4):642–697
4. Zhou S, Wang J (2018) Dual serial vortex-induced energy harvesting system for enhanced energy harvesting. AIP Adv 8(7):075221
5. Zhang X, Yang W, Zuo M, Tan H et al (2018) Arc-shaped piezoelectric bistable vibration energy harvester: modeling and experiments. Sensors 18(12):4472
6. Erturk A, Inman DJ (2009) An experimentally validated bimorph cantilever model for piezoelectric energy harvesting from base excitations. Smart Mater Struct 18(2):025009